Remote Entanglement of Trapped Atomic Ions

by

David Lynn Moehring

A dissertation submitted in partial fulfillment
of the requirements for the degree of
Doctor of Philosophy
(Physics)
in The University of Michigan
2007

Doctoral Committee:

Professor Christopher R. Monroe, Chair
Professor Charles R. Doering
Professor Luming Duan
Professor David W. Gerdes
Professor Roberto D. Merlin

"You believe in a dice-playing God and I in perfect laws in the world of things existing as real objects, which I try to grasp in a wildly speculative way." — Albert Einstein

"...any observation necessitates an interference with the course of the phenomena, [and requires] a final renunciation of the classical ideal of causality and a radical revision of our attitude towards the problem of physical reality." — Niels Bohr

To Lauren.

ACKNOWLEDGEMENTS

For those who know me well, you know that I am not an overly emotional person. Despite this, I hope to make clear my deep appreciation for all those who helped me to get through graduate school and to the point of writing this thesis. As anyone who has worked in experimental physics can tell you, research does not get done singlehandedly. I'd therefore like to first thank all those who worked directly with me on my experiments.

When I first joined Chris Monroe's group back in the Summer of 2002, Chris gave me an empty optical table and pretty much said, "have at it." Russ Miller, an undergraduate with a year of experience in the lab, was an irreplaceable lab partner during my first year. Together, we had the pleasure of taking this empty optical table and building a complete, functional ion trap experiment. When starting from such humble beginnings, there is a lot that one needs to know. As was the case with Russ, and everyone else that I will mention later, what I lacked in knowledge and experience, my lab partners were always there to meet my needs.

About the time when Russ was ready to leave for graduate school during the Summer of 2003, Boris Blinov joined us as a post-doc. Chris had moved Boris from the other experiment in the group because according to him, our project was about to "take off." Boris's attitude toward research allowed me to find out how enjoyable research could be, and I very much enjoyed the time we spent together.

The arrival of Professor Luming Duan in the Fall of 2003 was a pivotal point in my graduate career. At his suggestion, Boris and I began working on what turned out to be the main topic of my dissertation research — ion-photon entanglement. As a theorist, Luming understands well the issues and possibilities in experimental physics, and throughout my career has made many important suggestions for the direction of my research.

With the main direction of my research now set and progressing, more students and post-docs began joining the experiment. The first of these were Rudy Kohn and Martin Madsen. As an undergraduate student, Rudy was instrumental in building many of the electronics that were used in the experiment, and Martin was a fierce experimentalist always pushing the experiment toward completion.

Shortly before Boris left the group, Peter Maunz joined the group as a post-doc. During the last two years, and especially during the construction of the ytterbium system from not only and empty table, but from a completely empty room, I learned more experimental physics from Peter than I could have imagined. Also pivotal during the last two years were the additions of Kelly Younge, Steve Olmschenk and Dzmitry Matsukevich. As graduate students, Kelly and Steve were both instrumental in the setup and completion of our recent work with ytterbium, and Dzmitry's experience with atomic ensembles made invaluable contributions to the remote-ion entanglement experiment.

In addition to those I worked with directly, I would also like to thank the other members of the Monroe group: post-docs Winni Hensinger, Paul Haljan, and Ming-Shien Chang; graduate students Patty Lee, Louis Deslauriers, Kathy-Anne Brickman, Dan Stick, Mark Acton, Jon Sterk, and Yisa Rumala; undergraduate students David Hucul, Mark Yeo, Liz Otto, Dan Cook, and Andrew Chew; and visiting Professor

James Rabchuck from Western Illinois University. All of these people, whether they tried or not, made valuable contributions to my research throughout the years. In addition to those in the lab, I'd like to thank the members of Dave Gidley's group: Dave, Rich Vallery, and Tracy Sanderson, who lent their expertise for our excited state lifetime experiment. I'd also like to thank the staff in the Physics Department at the University of Michigan, especially Kim Smith who answered all my questions and made sure I was always on track. If there is someone I have forgotten, please do not mistake my poor memory for lack of appreciation.

Of course, none of this would have been possible if not for the support of my advisor, Chris Monroe. When I think back on my needed advice for my experiment and classes, support for buying the necessary equipment and going to conferences, specific discussions on career paths, or just someone to be a good squash opponent, never once did I go without. Thank you to everyone of you for the last 5 years.

Finally, I would like to say an extra special thank you to my family and especially my wife. Their unconditional support throughout not just the last 5 years, but all through my life has made me a better person, and for this, I am eternally grateful.

TABLE OF CONTENTS

LIST OF TABLES

Table

LIST OF FIGURES

Figure

LIST OF APPENDICES

Appendix

CHAPTER I

Introduction

Since the development of quantum mechanics almost a century ago, there has been considerable controversy over the interpretations and results of quantum theory. This controversy stems mainly from the highly counterintuitive predictions of quantum mechanics which include the issues of superposition, wave-particle duality, irreversible measurement collapse, the uncertainty principle, and perhaps most famously, entanglement at a distance. In the seminal paper by Einstein, Podolsky and Rosen [1], the authors discuss the seemingly contradictory results of quantum mechanics that are at the heart of this debate, leading them to question the completeness of quantum theory itself. In their words:

> In a complete theory there is an element corresponding to each element of reality. A sufficient condition for the reality of a physical quantity is the possibility of predicting it with certainty, without disturbing the system. In quantum mechanics in the case of two physical quantities described by non-commuting operators, the knowledge of one precludes the knowledge of the other. Then either (1) the description of reality given by the wave function in quantum mechanics is not complete or (2) these two quantities cannot have simultaneous reality. Consideration of the problem of making

> predictions concerning a system on the basis of measurements made on another system that had previously interacted with it leads to the result that if (1) is false then (2) is also false. One is thus led to conclude that the description of reality as given by a wave function is not complete.

For many years, these controversies were debated exclusively in the realm of theoretical physics. However, in 1965, John Bell and others began to develop experimentally realizable conditions using entangled particles to answer some of these questions [2, 3, 4]. These proposed Bell inequality tests show that the existence of local hidden variables impose restrictions on measured correlations that are in contradiction with the predictions of quantum mechanics.

Experiments showing violations of these Bell inequalities followed shortly thereafter involving entangled photon pairs [5, 6, 7, 8, 9], low-energy protons [10], neutral kaons [11], and more recently in trapped atomic ions [12, 13], individual neutrons [14] and even hybrid systems [15, 16, 17, 18]. In all such cases, the measured correlations are in convincing agreement with quantum mechanics and provided strong evidence against the existence of local hidden-variable theories. Based on these results, the description of reality given by the quantum mechanical wave function can indeed be considered complete, even though quantum mechanics cannot predict results with certainty. Although these fundamental questions continued to trouble many physicists over the past century, the development of the new field of quantum information science and the possible applications that may result from large scale quantum systems have brought many of these questions of quantum mechanics to the mainstream of not only theoretical but also experimental physics.

The work presented in this thesis deals with a system at the heart of these questions — quantum entanglement of trapped atomic ions at a distance. Entanglement

is the key resource in quantum information, and trapped ions are among the most attractive systems for scalable quantum information protocols because they can be well isolated from the environment and manipulated easily with lasers [19, 20, 21, 22, 23, 24, 25, 26, 27, 28, 29, 30, 31, 32, 33, 34, 35, 36, 37, 38, 39, 40, 41]. Over the past decade, the trapped ion system has shown tremendous progress toward a quantum information processor, however as one tries to scale this system from current experiments involving less than ten atomic quantum bits (qubits) to many hundreds or thousands of qubits, current experimental setups may be too limited to deal with the complexity of these very large systems. One approach to overcome this scaling problem in ion traps is to shuttle the ions through multi-zone traps [42, 43, 44, 45]. In such a system, quantum gates are performed in "entangling zones" of the larger trap structure, and the ions are shuttled to other zones for storage or further operations as necessary. Still, as the number of ions grows and the dimensions of the traps shrink, preserving coherence may become exceedingly difficult [46].

An alternative scaling approach, and the topic of this thesis, is to use photon-mediated entanglement. With this approach, ions in many different trapping zones can be entangled without the need for cooling to the motional ground state or even localization within the Lamb-Dicke regime. Even though this approach is typically probabilistic, it has been shown to scale favorably both with the success probability of atom-atom entanglement in a given trial and the number of qubits [47, 48, 49], thus eliminating the need for challenging cavity QED techniques necessary for the generation of deterministic quantum information transfer between atomic and photonic sources[1] [50, 32, 33, 40].

[1]While QED techniques are not strictly necessary, they can be incorporated into the protocols described in this thesis and can help to increase the probability of spontaneously emitting a photon into the mode of interest, currently the largest limiting factor to the success probability for atom-photon and remote-atom entanglement.

Probabilistic atom entanglement leads to deterministic quantum computation in a way similar to linear optical quantum computing, where quantum interference of photons is used to create quantum entanglement and quantum gates. By combining atomic and photonic systems, the benefits of atomic quantum memory [51, 52, 53] and the quantum communication of photons are combined. If two photons emitted by two remotely located atomic sources interfere on a beam splitter, then the appropriate measurement of the photons from the two atoms can project the atoms into an entangled state. This heralded entanglement can be used as a resource for further quantum information processing. In addition, combination of the photon and ion systems which have independently closed the locality and detection loopholes, may allow for remote ion-entanglement with the potential for measuring a loophole free Bell inequality violation [54].

In this thesis, I describe a theoretical and experimental framework for the entanglement of two particles using trapped atomic ions. Using our trapped ion system, I show the first explicit demonstration of quantum entanglement between matter and light using a single ion and its single emitted photon, including the first measurement of a Bell inequality violation between two particles of different species. Building upon this ion-photon entanglement, I demonstrate the first entanglement of two individual massive particles at a distance. In our experiment, two independently-trapped, remotely-located ions are each entangled with their emitted photons, and the interference and detection of these photons heralds the entanglement of the atomic quantum bits.

I begin with a general theoretical overview to the entanglement between a single atom and a single photon (Chapter II). Next, Chapter III shows how remote entanglement can be created using atom-photon entangled pairs. Chapter IV begins my

experimental work with trapped ions. In particular, it introduces the two different ion species used in the experiments reported in this thesis — cadmium and ytterbium — as well as the infrastructure needed for these experiments. I next highlight the experimental results using the cadmium ion where we successfully demonstrated ion-photon entanglement (Chapters V and VI) and made important steps toward the entanglement of two ions (Chapter VII). At the end of this Chapter VII, I discuss the limitations of cadmium for remote ion entanglement and why we switched to the ytterbium ion (Section 7.3). Chapter VIII begins our work with the ytterbium ion, where I describe the improved generation of quantum interference of two photons, necessary for the demonstration of remote ion entanglement, and Chapter IX reports the realization of remote ion entanglement. In the concluding Chapter X, I discuss how this approach to remote ion entanglement, though probabilistic, can lead to a scalable quantum information network as well as fundamental tests on quantum theory.

CHAPTER II

Procedure for Probabilistic Entanglement between a Single Atom and a Single Photon

I begin by discussing the protocol for entanglement between a single atomic qubit and a single photon. Consider an atomic system possessing long-lived electronic states that can be used as a viable qubit and also having a strong electric dipole coupling to an excited electronic state. For concreteness, the atomic qubit states are assumed to be hyperfine levels in the $^2S_{1/2}$ ground states of a single valence electron atom [55], although other atomic level schemes can be used. I assume the atomic system has short-lived $^2P_{1/2}$ and $^2P_{3/2}$ excited states that spontaneously decay exclusively to the $^2S_{1/2}$ ground state. Similar systems with decay channels to other electronic states (such as low-lying ^2D states) also apply, but require the application of radiation driving population from these states back to the S-P levels.

When a single atom is prepared in one of the excited ^2P states, a single photon can be spontaneously emitted via multiple decay channels after a mean time of τ (the natural lifetime of the P state) typically in the nanosecond range. Attributes of the emitted photon from the multiple decay channels can become entangled with the resulting $^2S_{1/2}$ ground states of the atom.

The simplest atomic level diagram for this system (nuclear spin $I = 1/2$) is shown in Figure 2.1(a). The main requirement for atom-photon entanglement is to drive

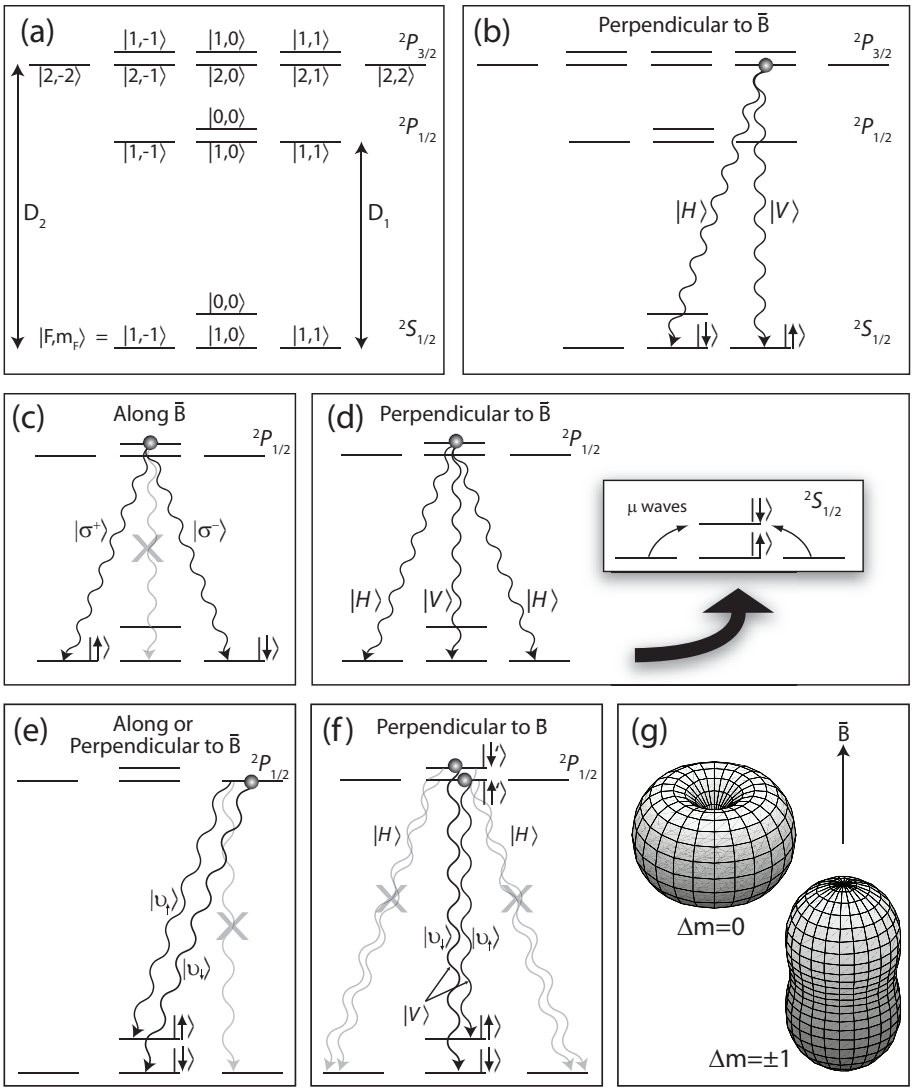

Figure 2.1: Possible schemes for atom-photon entanglement. (a) Energy level diagram for an atom with nuclear spin $I = 1/2$ and magnetic moment $\mu_I < 0$. (b) Decay scheme unique to the $^2P_{3/2}$ level with two possible decay channels. If the photon is emitted perpendicularly to the quantization axis, the polarization modes are linear and orthogonal. (c) Decay scheme consisting of three decay channels, where viewing along the quantization axis eliminates the photon from the $\Delta m = 0$ decay channel due to the radiation pattern, and the $\Delta m = \pm 1$ photons have orthogonal circular polarizations. (d) Same decay scheme as (c) but viewed perpendicularly to the quantization axis. The $\Delta m = 0$ photon decay channel is linear and orthogonal to the $\Delta m = \pm 1$ decay channels. After decay, the $|1, -1\rangle$ and $|1, 1\rangle$ can be coherently combined in the $|0, 0\rangle$ state establishing the atomic qubit (see Appendix A.1). (e) Two $|\Delta m| = 1$ decay channels with the same polarization comprise a photonic frequency qubit. The $\Delta m = 0$ photon can be eliminated by a polarizer, or by the radiation pattern if viewed along the quantization axis. (f) Two $\Delta m = 0$ decay channels with the same polarization and different frequencies. Viewed perpendicularly to the quantization axis, the $\Delta m = \pm 1$ photons are eliminated via a polarizer. As described in the text, this decay scheme can be used to perform quantum gates between the atom and the photon. (Note that cases (c)-(f) also apply to the $^2P_{3/2}$ levels.) (g) Radiation emission patterns for the $\Delta m = 0$ and $\Delta m = \pm 1$ decay channels, defined by a magnetic field $\vec{B}$.

the atom to a state with multiple decay channels which result in different levels of atomic ground state $|S_i\rangle$. The resulting (unnormalized) state of the photon and atom is:

$$\Psi = \sum_{i,j,\Delta m} C_{i,j,\Delta m} |S_i\rangle |\nu_j\rangle |\Pi_{\Delta m}\rangle, \tag{2.1}$$

where $C_{i,j,\Delta m}$ are atomic Clebsch-Gordon (CG) coefficients, ν_j are the photon frequencies, and $\Pi_{\Delta m}$ are the photon polarizations.

The photons are emitted in a specific radiation pattern depending on the change in angular momentum of the atom along the quantization axis, Δm (defined by an applied magnetic field of typically a few Gauss [Figure 2.1(g)]). For $\Delta m = 0$, the (unnormalized) polarization state of a spontaneously emitted photon is $|\Pi_0\rangle = -\sin\theta|\hat{\theta}\rangle$ and for $\Delta m = \pm 1$, the states are $|\Pi_{\pm 1}\rangle = e^{\pm i\phi}(\cos\theta|\hat{\theta}\rangle \pm i|\hat{\phi}\rangle)/\sqrt{2}$, where θ and ϕ are spherical polar and azimuthal angles of the emitted photon's wavevector with respect to the quantization axis, and $\hat{\theta}$ and $\hat{\phi}$ are their associated spherical coordinate unit vectors. Based on these formulas, there are a number of protocols which are good candidates for atom-photon entanglement, five of which are illustrated in Figures 2.1(b-f).

Ideally, the atom will decay to two different $^2S_{1/2}$ levels via two distinct decay channels of distinguishable photon qubit states (either polarization or frequency states). Polarization qubits typically require the photon to be emitted in a specific direction. One convenient choice is for a photon emitted perpendicularly to the dipole axis ($\theta = \pi/2$). In this case the $\Delta m = \pm 1$ radiation is linearly polarized and orthogonal to the $\Delta m = 0$ radiation. Another possibility is emission along the quantization axis ($\theta = 0$). Here, no $\Delta m = 0$ photons are emitted due to the radiation intensity pattern [Figure 2.1(g)], whereas the $\Delta m = \pm 1$ photons have opposite (orthogonal) helicity. With polarization qubits, single qubit rotations are easily ac-

complished via quarter and half waveplates, and qubit state detection is done with polarizing beam splitters and single photon detectors.

One possible decay scheme is shown in Figure 2.1(b) where the $^2P_{3/2}\,|F=2, m_F=1\rangle$ excited state is prepared, where F is the total angular momentum and m_F is its projection along the quantization axis. From here, the atom spontaneously decays back to either the $^2S_{1/2}\,|1,0\rangle \equiv |\downarrow\rangle$ state while emitting a σ^+-polarized photon, or to the $^2S_{1/2}\,|1,1\rangle \equiv |\uparrow\rangle$ state while emitting a π-polarized photon (with identical CG coefficients). With this decay scheme, the photon polarizations are orthogonal when viewed perpendicularly to the quantization axis, with the π decay photon polarized parallel to the quantization axis (defined as $|V\rangle$), and the σ^+ decay photon polarized perpendicularly to the quantization axis (defined as $|H\rangle$). The resulting atom-photon entangled state is $\sqrt{1/3}\,|\downarrow\rangle\,|H\rangle + \sqrt{2/3}\,|\uparrow\rangle\,|V\rangle$, where the different prefactors come from the spatial radiation intensity modes for $\Delta m = -1$ and $\Delta m = 0$ transitions. Although this state is not a maximally entangled Bell state, it is still sufficient for multi-atom entanglement experiments as will be shown in Chapter III. Alternatively, this entangled state can be made into a Bell state by simply inserting a polarization-selective lossy element into the path of the photons, at the cost of a somewhat lower efficiency [56].

Figures 2.1(c-d) show similar decay schemes which give rise to entanglement between the atomic qubit and the photon polarization qubit. In both of these schemes, the atom is prepared in the $^2P_{1/2}\,|0,0\rangle$ (or $^2P_{3/2}\,|2,0\rangle$) state with three decay channels[1]. Along the quantization axis [Figure 2.1(c)], no $\Delta m = 0$ photons are detected due to the radiation pattern, and the $\Delta m = \pm 1$ photons have orthogonal circular

[1]The $^2P\,|1,0\rangle$ states would also work well for the scheme shown in Figure 2.1(c), but for the scheme illustrated in Figure 2.1(d), the two polarization components would also have different frequencies. Theoretically, this is not a problem, but experimentally, it is difficult to control the subsequent phase on single qubit rotations, as will be discussed in more detail in Section 5.2.

polarizations. The resulting polarizations can be converted into the $|H\rangle - |V\rangle$ basis with a quarter waveplate, creating the $(|\downarrow\rangle |H\rangle + |\uparrow\rangle |V\rangle)/\sqrt{2}$ Bell state. Similarly, if observed perpendicularly to the quantization axis [Figure 2.1(d)], the polarization of the $\Delta m = 0$ decay channel is orthogonal to the $\Delta m = \pm 1$ decay channels. While this results in populating three atomic levels, $|1, -1\rangle$ and $|1, 1\rangle$ can be coherently combined in the $|0, 0\rangle$ state transferring the population to the first order magnetic field insensitive "clock qubit" states [55], as discussed in Appendix A.1.

In addition to photon polarizations, two resolved frequencies can also be used for the photonic qubit. As compared with polarization qubits, frequency qubits can be difficult to manipulate as it is much more challenging to separate and detect frequency components (typically separated by a few GHz for atomic systems) than to measure different polarization modes. Direct measurement of the photon frequency qubits would be possible by using a Mach-Zehnder interferometer with a path length difference equal to $c/2\Delta\nu$, where $\Delta\nu$ is the frequency splitting of the photonic qubit. Qubit rotations can also be performed by changing the path length difference of the interferometer, or directly by using an electro optic modulator [57]. Nonetheless, a technical challenge for further atomic state rotations is synchronization of the photon arrival time with the free evolution of the atomic hyperfine qubit ($1/\Delta\nu = 100$ ps for $\Delta\nu = 10$ GHz), which may be feasible using very fast electronics and detectors. However, direct diagnosis of the photonic qubit is not necessary when performing remote atom entanglement, as is discussed in Chapter III and demonstrated in Chapter IX.

Despite the difficulty with qubit state detection, frequency qubits are expected to be more robust than polarization qubits with remote entanglement. Closely-spaced frequency components of the same polarization have essentially zero dispersion in typical optical paths, and thus are highly insensitive to phase jitter and birefrin-

gence inherent in optical paths [58, 59, 60, 61, 62, 63, 64]. Furthermore, because these frequency qubit states have the same spatial emission patterns, efficient mode-matching is possible even with an increased collection solid angle [49].

One scheme using frequency qubits is shown in Figure 2.1(e) where an atom prepared in the ${}^2P_{1/2}\ |1,1\rangle$ state decays to the ${}^2S_{1/2}\ |1,0\rangle$ and $|0,0\rangle$ states emitting a photon with a single polarization but in a superposition of different frequencies. Here, a π-polarized photon to the ${}^2S_{1/2}\ |1,1\rangle$ state can be eliminated via a polarizer or by detecting along the quantization axis, resulting in the atom-photon entangled state $(|\uparrow\rangle\,|\nu_\uparrow\rangle - |\downarrow\rangle\,|\nu_\downarrow\rangle)/\sqrt{2}$, where the negative sign is a result of the Clebsch-Gordon coefficients.

While either photonic qubit allows for the creation of entanglement between atoms and photons, frequency qubits further enable the possibility to propagate prior superposition or entanglement of the atom to the photon, which can be used for quantum gates [49]. Consider the setup illustrated in Figure 2.1(f), where an atom is initially prepared in a superposition of the clock qubit states $|F, m_F = 0\rangle \equiv |\uparrow\rangle$ and $|F+1, m_F = 0\rangle \equiv |\downarrow\rangle$. Upon excitation with a π-polarized laser pulse, the atom can be coherently driven to the corresponding clock qubit states in the excited ${}^2P_{1/2}$ levels[2], $|F'+1, m_{F'} = 0\rangle \equiv |\uparrow'\rangle$ and $|F', m_{F'} = 0\rangle \equiv |\downarrow'\rangle$ respectively, where $F' = F$. Cross-coupling between the levels $|\uparrow\rangle \leftrightarrow |\downarrow'\rangle$ and $|\downarrow\rangle \leftrightarrow |\uparrow'\rangle$ is prohibited by selection rules. After spontaneous emission of a π-polarized photon into the appropriate mode (and $\Delta m = \pm 1$ photons eliminated via a polarizer), the atom and photon are entangled in the state $c_\uparrow\,|\uparrow\rangle\,|\nu_\uparrow\rangle + c_\downarrow\,|\downarrow\rangle\,|\nu_\downarrow\rangle$, where $c_\uparrow$ and $c_\downarrow$ correspond to the initial superposition amplitudes of the atom before excitation. The construction of gates from this entanglement is discussed in Chapter III.

[2]The scheme depicted in Figure 2.1(f) works not only $I = 1/2$, but for any half integer I. Additionally, for $I = 1/2$, it is also possible to excite on the D2 line to the ${}^2P_{3/2}$ manifold where the $|\uparrow\rangle$ and $|\downarrow\rangle$ states are excited to $|F' = 1, m_{F'} = 0\rangle$ and $|F' = 2, m_{F'} = 0\rangle$ respectively [65].

For any of the atom-photon entanglement schemes described above, the probability of detecting the entanglement in a given trial is less than unity, $P_{\text{a-p}} \equiv p_e p < 1$. Here, p_e is the probability of single photon emission[3] and $p = f\eta T(\Delta\Omega/4\pi)$ is the probability of a photon being detected in the desired spatial mode, where $f = I_{\Delta\Omega}/\langle I\rangle$ is of order unity and describes the intensity of the atomic emission pattern into the light collection solid angle $\Delta\Omega$ compared to the average emission intensity over all space, η is the quantum efficiency of the single photon detectors, and T is the optical transmission. This results in an atom-photon entanglement success rate of $R_{\text{a-p}} = P_{\text{a-p}}/T_{\text{rep}}$, where the repetition time T_{rep} is fundamentally limited by the excited state lifetime, τ.

Ideally, $P_{\text{a-p}}$ could approach unity. The excitation probability could be near unity by using an ultrafast laser pulse ($p_e \sim 1$), as discussed in the following chapters. One could also increase the collection efficiency of scattered photons by placing the atom within an optical cavity. This could potentially allow the collection of all scattered photons, effectively allowing $f(\Delta\Omega/4\pi)$ to approach unity without sacrificing fidelity [36, 66, 67, 40]. Photon detector efficiencies can also be near perfect [68, 69, 70]. However, since these improvements come at great effort, the success probability on a given trial is assumed in the following discussions to be $p \ll 1$.

[3]The emission of a single photon at the desired transition is equal to the atomic excitation probability, assuming no decay channels to low lying metastable states.

CHAPTER III

Procedure for Entangling Two Atomic Qubits Through Interference of Photons

While entanglement of nearby trapped ions has been realized through Coulomb-coupled motion [22, 24, 27, 28, 71, 72], atoms separated by too large a distance for direct atom-atom interactions may instead be entangled via their emitted photons. This remote-atom entanglement requires the ability to mode-match the photons from two atom-photon entangled pairs such that the photons from each atom are indistinguishable [73, 74, 54].

3.1 Single Photon Detection Scheme

The first example of a photon-mediated remote-atom entanglement protocol, proposed by Cabrillo *et al.* [73], begins with two atoms each prepared in a known ground state $|\downarrow\rangle$ of a 3-level lambda system [Figure 3.1(a)]. These two atoms are then simultaneously weakly driven ($p_e = \epsilon \ll 1$) to the excited state $|e\rangle$ from where the atom will decay either to the original state, or to a second ground state $|\uparrow\rangle$. After the weak excitation pulse, the two atoms are each in the (unnormalized) state $|\downarrow\rangle + \sqrt{\epsilon}|e\rangle$, or for atoms a and b: $(|\downarrow\rangle_a + \sqrt{\epsilon}|e\rangle_a) \otimes (|\downarrow\rangle_b + \sqrt{\epsilon}|e\rangle_b) = |\downarrow\rangle_a|\downarrow\rangle_b + \sqrt{\epsilon}\,|\downarrow\rangle_a|e\rangle_b + \sqrt{\epsilon}|e\rangle_a|\downarrow\rangle_b + \epsilon|e\rangle_a|e\rangle_b$. For successful atom-atom entanglement, a single photon must be detected from one of the two atoms, where the detector is

only sensitive to the $|e\rangle \rightarrow |\uparrow\rangle$ decay channel. If the atomic excitation is sufficiently small such that the probability of both atoms emitting a photon is negligible, $\epsilon^2 \ll 2\epsilon$, then by the projection postulate, after detection of the single photon, the atoms are in the entangled state $(|\downarrow\rangle_a |\uparrow\rangle_b + e^{i\phi} |\uparrow\rangle_a |\downarrow\rangle_b)/\sqrt{2}$, where the phase $\phi = k\Delta x$ comes from the optical path length difference between each atom and the detector.

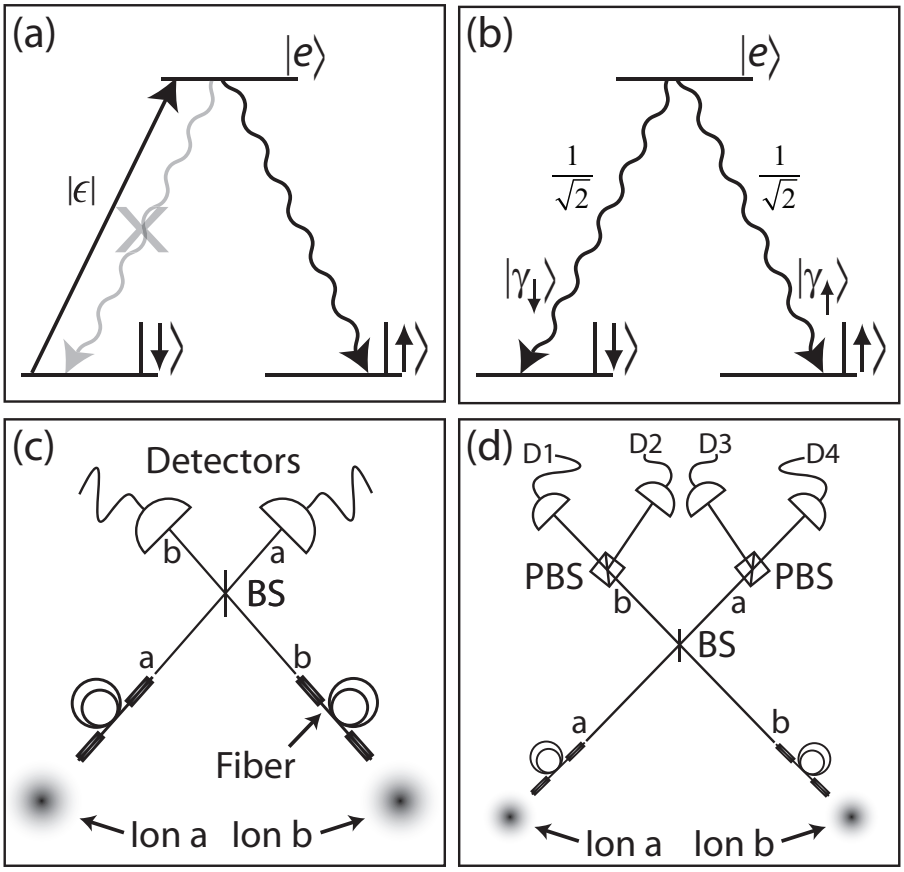

Figure 3.1: Entanglement schemes for two remotely located atomic qubits. (a) In the single-photon protocol by Cabrillo *et al.* [73], each atom is weakly excited with a probability ϵ from the ground state $|\downarrow\rangle$ to the excited state $|e\rangle$. The photon detectors are only sensitive to the $|e\rangle \rightarrow |\uparrow\rangle$ decay and a detection of a single photon projects the atoms into the entangled state $(|\downarrow\rangle_a |\uparrow\rangle_b + e^{i\phi} |\uparrow\rangle_a |\downarrow\rangle_b)/\sqrt{2}$. (b) In the two-photon protocol, each atom is prepared in the excited state with two decay channels giving rise to two distinguishable photonic qubit states. (c) Detection setup suitable for either entanglement protocol. With the protocol by Cabrillo *et al.*, only one of the two detectors detects a photon, whereas the two-photon protocol requires coincident detection on each detector, projecting the atoms into the entangled Bell state $|\Psi^-\rangle_{\text{atom}} = (|\uparrow\rangle_a |\downarrow\rangle_b - |\downarrow\rangle_a |\uparrow\rangle_b)/\sqrt{2}$. (d) An alternative setup when using polarization qubits in the two-photon protocol. Coincident detection between D1 and D3 or D2 and D4 projects the atoms into the state $|\Psi^-\rangle_{\text{atom}}$, whereas coincident detection between D1 and D2 or D3 and D4 results in $|\Psi^+\rangle_{\text{atom}} = (|\uparrow\rangle_a |\downarrow\rangle_b + |\downarrow\rangle_a |\uparrow\rangle_b)/\sqrt{2}$.

One limitation to the entanglement fidelity achievable with this protocol is the

probability of multiple photon emissions. By choosing $\epsilon \ll 1$, this probability is lowered, but at the expense of lowering the entanglement success probability. This protocol also requires that (the atoms be well localized such that) the path length the photon travels to the detector is known to much better than the wavelength of the emitted photon [75, 76], otherwise the phase in the final entangled state will be unknown and will ruin entanglement. Similarly, if an atom experiences a recoil upon emission, the evidence of which atom emitted the photon will again ruin the entanglement fidelity. These last two restrictions, however, may be overcome if the atoms are localized to well within the Lamb-Dicke limit.

Recent proposals have suggested a similar detection protocol that is less sensitive to the phase due to the path length that the photon travels to the detector [48, 77, 78]. However, this insensitivity to path length comes at the expense of a second detected photon in a subsequent excitation step, and still requires the atoms to be within the Lamb-Dicke limit. Hence, this type of entanglement may be more useful for solid state qubits (quantum dots [79, 80, 81, 82, 83], nitrogen-vacancies in diamond [84, 85], etc.) where the localization of the atomic qubit in the Lamb-Dicke limit is easily accomplished.

3.2 Two Photon Detection Scheme

A more robust two-photon protocol for remote atom entanglement, not requiring localization within the Lamb-Dicke limit and less sensitive to photonic phase, was proposed independently by Duan and Kimble [74] and Simon and Irvine [54]. The atomic energy levels for this approach are the same as the previous protocol, but the excited state can be prepared with arbitrarily high probability and the resulting entanglement requires the coincident detection of two photons, one from each

atom [Figure 3.1(b)]. The excited state has two decay channels with distinguishable photonic qubit modes — either polarization or frequency modes. After simultaneous excitations, the atoms each emit a single photon and are in the state:

$$\begin{aligned}
&\frac{1}{2}(|\downarrow\rangle_a|\gamma_\downarrow\rangle_a + |\uparrow\rangle_a|\gamma_\uparrow\rangle_a) \otimes (|\downarrow\rangle_b|\gamma_\downarrow\rangle_b + |\uparrow\rangle_b|\gamma_\uparrow\rangle_b) \\
&\quad = \frac{1}{2}(|\Psi^+\rangle_{\text{atom}}|\Psi^+\rangle_{\text{photon}} + |\Psi^-\rangle_{\text{atom}}|\Psi^-\rangle_{\text{photon}} \\
&\qquad + |\Phi^+\rangle_{\text{atom}}|\Phi^+\rangle_{\text{photon}} + |\Phi^-\rangle_{\text{atom}}|\Phi^-\rangle_{\text{photon}}),
\end{aligned} \tag{3.1}$$

where $|\gamma_\downarrow\rangle$ and $|\gamma_\uparrow\rangle$ are the qubit states of the photonic qubit, and $|\Psi^\pm\rangle_{\text{atom}} = (|\uparrow\rangle_a|\downarrow\rangle_b \pm |\downarrow\rangle_a|\uparrow\rangle_b)/\sqrt{2}$ and $|\Phi^\pm\rangle_{\text{atom}} = (|\uparrow\rangle_a|\uparrow\rangle_b \pm |\downarrow\rangle_a|\downarrow\rangle_b)/\sqrt{2}$ are the maximally entangled Bell states for the atoms, with corresponding definitions for the photons. (An extension to arbitrary atom-photon entangled states is given in Section 3.4.) If the two photon modes are matched on a 50/50 beam splitter, then they will exit on different ports only if they are in the antisymmetric state $|\Psi^-\rangle_{\text{photon}} = (|\gamma_\uparrow\rangle_a|\gamma_\downarrow\rangle_b - |\gamma_\downarrow\rangle_a|\gamma_\uparrow\rangle_b)/\sqrt{2}$, respecting the symmetry of the overall photonic wavefunction [86]. Therefore, coincident photon detection in the two output ports of this beam splitter projects the atoms into $|\Psi^-\rangle_{\text{atom}}$ [Figure 3.1(c)]. Additionally, with a polarizing beam splitter placed in either output port, it is possible to detect the (polarization qubit) photons in the state $|\Psi^+\rangle_{\text{photon}}$, thus projecting the atoms into the state $|\Psi^+\rangle_{\text{atom}}$ [Figure 3.1(d)]. For the other two photonic Bell states $|\Phi^\pm\rangle_{\text{photon}}$, both photons are always detected in the same qubit state and thus cannot herald a unique entangled state of the atoms [54].

For high fidelity atom-atom entanglement, it is important to emit only a single photon from each atom. With atom-photon entanglement, good entanglement fidelities can still be obtained using weak cw excitations, where the probability of spontaneously emitting two photons is $p_{2e} = p_e^2/2$. Hence, when detecting a single

photon, the probability of a second emitted photon, potentially affecting the fidelity of the entanglement, is only $p_e/2$. However, in the two photon atom-atom entanglement protocol, the probability of two photons being detected from one atom is of the same order as detecting two photons from different atoms (discussed in more detail in in Section 3.4). Emitting only a single photon requires the excitation pulse duration to be much shorter than the excited state lifetime, and allows for $p_{2e} \to 0$. In addition to eliminating multiple excitations, a fast excitation pulse can also allow for near unit excitation probability ($p_e \sim 1$), which can lead to a significant increase in entanglement success probability.

Even with an increased excitation probability, the likelihood of detecting a single emitted photon is typically low, and therefore the requirement of detecting both emitted photons can make this protocol significantly slower than the single photon protocol. However, with the possibility to considerably increase the effective photon collection solid angle via an optical cavity, the latter approach can be comparable in success probability, or even greater, due to the intrinsic limitation of $p_e \ll 1$ in the single photon protocol.

Additionally, by starting with two atom-photon pairs entangled in the method of Figure 2.1(f), one could allow for quantum gates between the two atoms using this protocol [49]. For this, the choice of pulse length (bandwidth) must allow for unique simultaneous excitation of both qubit states. Therefore, the pulsed laser bandwidth needs to be larger than the largest hyperfine splitting, but smaller than the fine structure splitting to eliminate coupling to the different excited state levels [Figure 3.2].

Because of the insensitivity to atomic localization and interferometric phase, our experiments have focused on the two-photon entanglement. In the following, I will

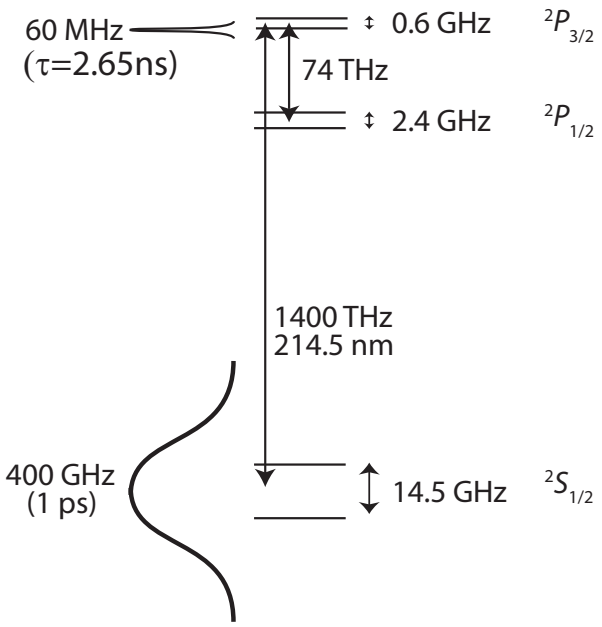

Figure 3.2: Pulsed Laser frequency requirements. Energy levels (not to scale) and laser bandwidth requirements for generation of a high efficiency single photon source (atomic values shown are for $^{111}Cd^{+}$). For simultaneous excitation of both hyperfine qubit states, the bandwidth of the laser pulse must be much larger than the largest hyperfine splitting, but smaller than the fine structure splitting to eliminate coupling to the different excited state levels. To eliminate multiple scatters, the pulse duration must be much smaller than the excited state lifetime (have a bandwidth much larger than the linewidth of the excited state).

discuss this protocol exclusively.

3.3 Coupling Photon Modes with a Beam splitter

The central component of the photonic coupling used to entangle atomic qubits is the interference of photons on a beam splitter (BS). This involves single photons entering the two input ports of the BS, as shown in Figure 3.3. If the spatial, temporal, and frequency modes of the two photons coincide on the BS, there are two indistinguishable ways for the photons to emerge in separate output ports: both photons are transmitted through the BS, and both photons are reflected from the BS [Figure 3.3(d-e)]. It is the destructive interference of these two amplitudes [86] that can project the atoms into an entangled state.

Consider the general interference of two photonic modes on a beam splitter, which can be conveniently described by effective angular momentum rotation operators [87]. As shown in Figure 3.3(a), spatial modes a and b are depicted by the two straight paths through the BS, and the BS transfers photons between these two modes. Given n and m photons in respective modes a and b before the BS, the action of the BS is identical to rotations within an effective $J = N/2$ angular momentum system, where $N = n + m$. Formally, the two mode input state $|n\rangle_a|m\rangle_b$ evolves to

$$|n\rangle_a|m\rangle_b \rightarrow e^{-i\chi\hat{J}_y}|n\rangle_a|m\rangle_b, \tag{3.2}$$

where the rotation angle χ is π times the reflectivity R of the lossless BS, and $\hat{J}_y = -i(\hat{a}^\dagger\hat{b} - \hat{a}\hat{b}^\dagger)/2$ [87]. The photon annihilation and creation operators, $\hat{a}$ and $\hat{a}^\dagger$ for mode a and $\hat{b}$ and $\hat{b}^\dagger$ for mode b, follow the usual bosonic commutation relations $[\hat{a}, \hat{a}^\dagger] = [\hat{b}, \hat{b}^\dagger] = 1$.

I write down the evolution of two-mode photonic states for up to $N = 3$ total photons, using angular momentum rotation matrices [88]. Obviously, the trivial case

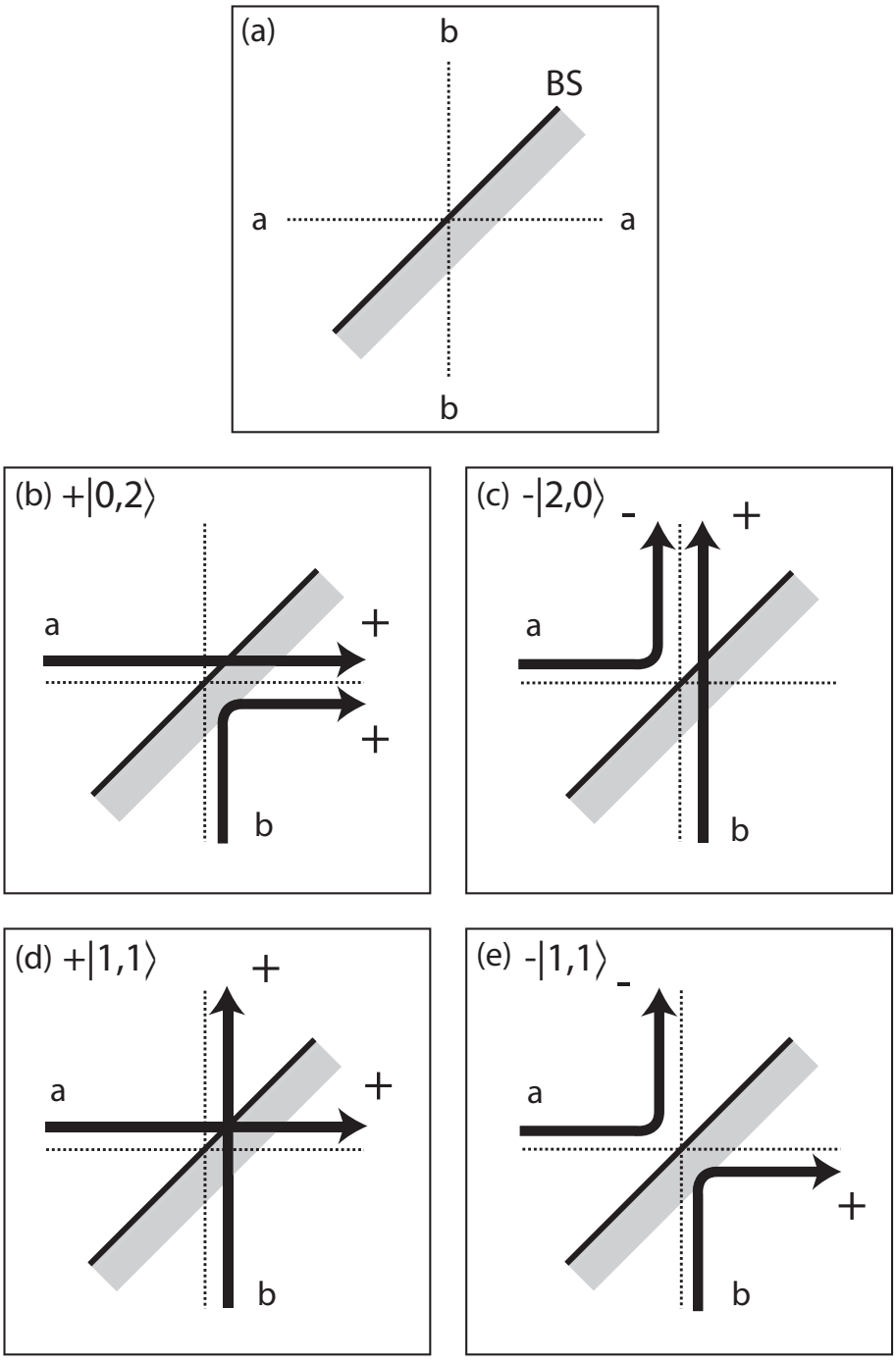

Figure 3.3: Modes of a beam splitter. (a) Spatial modes a and b are straight paths through the beam splitter (BS), and the beam splitter interferes these two modes. (b-e) The four possible output modes of two photons entering a beam splitter from different ports. A negative phase is acquired only upon reflection from low to high index of refraction — mode a in (c) and (e).

of $N = 0$ photons does not evolve. For a total of $N = 1$ photon in the two input modes, the equivalent spin-1/2 system evolves as:

$$\begin{pmatrix} |0\rangle_a|1\rangle_b \\ |1\rangle_a|0\rangle_b \end{pmatrix} \rightarrow \begin{bmatrix} \cos\frac{\chi}{2} & \sin\frac{\chi}{2} \\ -\sin\frac{\chi}{2} & \cos\frac{\chi}{2} \end{bmatrix} \begin{pmatrix} |0\rangle_a|1\rangle_b \\ |1\rangle_a|0\rangle_b \end{pmatrix}. \tag{3.3}$$

For $N = 2$ photon input states, we find,

$$\begin{pmatrix} |0\rangle_a|2\rangle_b \\ |1\rangle_a|1\rangle_b \\ |2\rangle_a|0\rangle_b \end{pmatrix} \rightarrow \begin{bmatrix} \frac{1}{2}(1+\cos\chi) & \frac{1}{\sqrt{2}}\sin\chi & \frac{1}{2}(1-\cos\chi) \\ \frac{-1}{\sqrt{2}}\sin\chi & \cos\chi & \frac{1}{\sqrt{2}}\sin\chi \\ \frac{1}{2}(1-\cos\chi) & \frac{-1}{\sqrt{2}}\sin\chi & \frac{1}{2}(1+\cos\chi) \end{bmatrix} \begin{pmatrix} |0\rangle_a|2\rangle_b \\ |1\rangle_a|1\rangle_b \\ |2\rangle_a|0\rangle_b \end{pmatrix}, \tag{3.4}$$

and for reference, the evolution for $N = 3$ photon input states is:

$$\begin{pmatrix} |0\rangle_a|3\rangle_b \\ |1\rangle_a|2\rangle_b \\ |2\rangle_a|1\rangle_b \\ |3\rangle_a|0\rangle_b \end{pmatrix} \rightarrow$$

$$\begin{bmatrix} cos^3\frac{\chi}{2} & \sqrt{3}cos^2\frac{\chi}{2}sin\frac{\chi}{2} & \sqrt{3}cos\frac{\chi}{2}sin^2\frac{\chi}{2} & sin^3\frac{\chi}{2} \\ -\sqrt{3}cos^2\frac{\chi}{2}sin\frac{\chi}{2} & cos^3\frac{\chi}{2} - 2cos\frac{\chi}{2}sin^2\frac{\chi}{2} & -sin^3\frac{\chi}{2} + 2cos^2\frac{\chi}{2}sin\frac{\chi}{2} & \sqrt{3}sin^2\frac{\chi}{2}cos\frac{\chi}{2} \\ \sqrt{3}cos\frac{\chi}{2}sin^2\frac{\chi}{2} & sin^3\frac{\chi}{2} - 2sin\frac{\chi}{2}cos^2\frac{\chi}{2} & cos^3\frac{\chi}{2} - 2sin^2\frac{\chi}{2}cos\frac{\chi}{2} & \sqrt{3}cos^2\frac{\chi}{2}sin\frac{\chi}{2} \\ -sin^3\frac{\chi}{2} & \sqrt{3}cos\frac{\chi}{2}sin^2\frac{\chi}{2} & -\sqrt{3}cos^2\frac{\chi}{2}sin\frac{\chi}{2} & cos^3\frac{\chi}{2} \end{bmatrix}$$

$$\begin{pmatrix} |0\rangle_a|3\rangle_b \\ |1\rangle_a|2\rangle_b \\ |2\rangle_a|1\rangle_b \\ |3\rangle_a|0\rangle_b \end{pmatrix}. \tag{3.5}$$

3.4 Resulting Atom-Atom Entangled State

As discussed previously, when an atom emits a photon, attributes of the photon (e.g., polarization or frequency) can become entangled with the atomic qubit, spanned by the atomic qubit states $|\downarrow\rangle$ and $|\uparrow\rangle$. This internal degree of freedom of the photon (photonic qubit) is represented by the two states $q = \alpha, \beta$ in a given spatial mode $s = a, b$. I begin with a description of the quantum state of a single atomic qubit and the photonic mode into which the atom emits, including various imperfections such as background light and multiple atomic excitations. I then extend this situation to the case of two atoms whose emitted photons interact on a BS following the above transformations.

A single atom is prepared in its excited state with excitation probability p_e, given one of the atomic level schemes in Figure 2.1, with a probability of double sequential excitation $p_{2e} \ll p_e$. For a weak excitation pulse of duration $t_e > \tau$, $p_e \ll 1$ and $p_{2e} = p_e^2/2$, while for an ultrafast excitation where $t_e \ll \tau$, we expect $p_{2e} \sim t_e/\tau \ll p_e^2/2$. Given that the atom is excited, the probability p that a single photon is detected in mode s is determined by the overlap between the atomic emission mode and spatial mode s, transmission losses, and the detection efficiency, as discussed in Chapter II. (I assume that $p \ll 1$, but this analysis applies equally well to cases where $p \sim 1$, appropriate for cavity-QED setups, where the atom preferentially emits into mode s.) The desired (post-selected) atom-photon entangled state is of the form:

$$|\Psi^{\text{ent}}\rangle = \cos\theta_s \,|\downarrow\rangle_s \,|0\rangle_s^\alpha |1\rangle_s^\beta + \sin\theta_s \,|\uparrow\rangle_s \,|1\rangle_s^\alpha |0\rangle_s^\beta, \tag{3.6}$$

where $|n\rangle_s^q$ is a state of n photons in spatial mode s and internal photonic qubit state q. The parameter θ_s depends on the particular excitation scheme [Figure 2.1] and is usually near $\pi/4$. Alternatively, for ultrafast excitation schemes, θ_s may describe the

initial atomic qubit state that is mapped onto the atom-photon entangled state [65, 49]. After a time long enough for the spontaneous emission of a photon, the complete quantum state of the atom-photon system is a mixed state of several alternatives with respective probabilities given in Table 3.1.

Quantum State	Probability	Description
$\|M\rangle_s\|0\rangle_s^\alpha\|0\rangle_s^\beta$	$1-pp_e-pp_{bg}$	no photons
$\cos\theta_s\|\downarrow\rangle_s\|0\rangle_s^\alpha\|1\rangle_s^\beta+\sin\theta_s\|\uparrow\rangle_s\|1\rangle_s^\alpha\|0\rangle_s^\beta$	pp_e	good photon
$\|M\rangle_s\|0\rangle_s^\alpha\|1\rangle_s^\beta$	$\frac{1}{2}pp_{bg}$	background photon
$\|M\rangle_s\|1\rangle_s^\alpha\|0\rangle_s^\beta$	$\frac{1}{2}pp_{bg}$	background photon
$\|M\rangle_s\|0\rangle_s^\alpha\|2\rangle_s^\beta$	$\frac{1}{4}p^2p_{bg}^2$	background photons
$\|M\rangle_s\|2\rangle_s^\alpha\|0\rangle_s^\beta$	$\frac{1}{4}p^2p_{bg}^2$	background photons
$\|M\rangle_s\|1\rangle_s^\alpha\|1\rangle_s^\beta$	$\frac{1}{2}p^2p_{bg}^2$	background photons
$\cos\theta_s\|\downarrow\rangle_s\|1\rangle_s^\alpha\|1\rangle_s^\beta+\sin\theta_s\|\uparrow\rangle_s\|2\rangle_s^\alpha\|0\rangle_s^\beta$	$\frac{1}{2}p^2p_ep_{bg}$	background+good photons
$\cos\theta_s\|\downarrow\rangle_s\|0\rangle_s^\alpha\|2\rangle_s^\beta+\sin\theta_s\|\uparrow\rangle_s\|1\rangle_s^\alpha\|1\rangle_s^\beta$	$\frac{1}{2}p^2p_ep_{bg}$	background+good photons
$\|M\rangle_s\|0\rangle_s^\alpha\|1\rangle_s^\beta$	pp_{2e}	double excitation photon
$\|M\rangle_s\|1\rangle_s^\alpha\|0\rangle_s^\beta$	pp_{2e}	double excitation photon
$\|M\rangle_s\|0\rangle_s^\alpha\|2\rangle_s^\beta$	$\frac{1}{4}p^2p_{2e}$	double excitation photons
$\|M\rangle_s\|2\rangle_s^\alpha\|0\rangle_s^\beta$	$\frac{1}{4}p^2p_{2e}$	double excitation photons
$\|M\rangle_s\|1\rangle_s^\alpha\|1\rangle_s^\beta$	$\frac{1}{2}p^2p_{2e}$	double excitation photons

Table 3.1: The mixed quantum state of a single atom and a single photon. A photon is in spatial mode s after a time long enough for spontaneous emission. The atomic qubit is represented by states $|\uparrow\rangle_s$ and $|\downarrow\rangle_s$ ($|M\rangle_s$ is an equal mixture of the two atomic qubit states), and the photon mode can support photons of internal qubit states α and β. The lowest order possibilities are listed with their associated probabilities.

The first term in Table 3.1 corresponds to the typical case of zero photons in either qubit state α or β resulting in a random atomic qubit state $|M\rangle_s = |\downarrow\rangle_s$ or $|\uparrow\rangle_s$, while the second term corresponds to the desired creation of entanglement between the atomic qubit and a single photonic qubit. The remaining terms are errors occurring from background events (background light entering the photonic mode) with probability pp_{bg}, and multiple excitation events with probability pp_{2e} and p^2p_{2e} corresponding to detecting one or both emitted photons respectively. Here, $p_{bg} \ll 1$ is the ratio of background photons to atomic fluorescence photons detected during the relevant time window. These error events are assumed to have an effective 50% chance of populating either photonic qubit state α or β of spatial mode s, and

multiple excitations are assumed to result in the random mixed state $|M\rangle_s$. The error states listed are the lowest order possibilities in their respective probabilities ($p, p_{bg}, p_{2e} \ll 1$).

When each of two atom-photon systems is independently and simultaneously prepared in the above form, the photonic part of these states can be interfered on a BS, and subsequent detection of the photons after the BS can project entanglement between the atoms. I now describe the quantum state of the atoms and photons after the BS, under the assumption that only photons with identical internal modes α or β (e.g., the two states of polarization or frequency) interfere on the beam splitter according to the transformations in Equations 3.3 and 3.4. In general, I assume that the two atoms are prepared in unique entangled superpositions with their photons, represented by the two angles θ_a and θ_b. Anticipating the post-selection of states that result in two photons leaving the BS in distinct modes (either in separate spatial modes or in the same spatial mode but with distinct internal modes), I write down only those states and their associated probabilities in Table 3.2.

In Table 3.2, the desired atom-atom entangled states are:

$$|\Psi^{\beta\alpha}\rangle_{ab} = \mathcal{N}_1 \left[\cos\theta_a \sin\theta_b \cos^2\frac{\chi}{2} |\downarrow\rangle_a |\uparrow\rangle_b - \sin\theta_a \cos\theta_b \sin^2\frac{\chi}{2} |\uparrow\rangle_a |\downarrow\rangle_b\right] \quad (3.7)$$

$$|\Psi^{\alpha\beta}\rangle_{ab} = \mathcal{N}_2 \left[\cos\theta_a \sin\theta_b \sin^2\frac{\chi}{2} |\downarrow\rangle_a |\uparrow\rangle_b - \sin\theta_a \cos\theta_b \cos^2\frac{\chi}{2} |\uparrow\rangle_a |\downarrow\rangle_b\right] \quad (3.8)$$

$$|\Psi^{\alpha\beta}\rangle_{aa} = \mathcal{N}_3 \left[(\cos\theta_a \sin\theta_b |\downarrow\rangle_a |\uparrow\rangle_b + \sin\theta_a \cos\theta_b |\uparrow\rangle_a |\downarrow\rangle_b) \sin\chi\right] \quad (3.9)$$

$$|\Psi^{\alpha\beta}\rangle_{bb} = |\Psi^{\alpha\beta}\rangle_{aa}, \quad (3.10)$$

where $\mathcal{N}_i$ are normalization constants. The first two states are correlated with single photons emerging in the two different BS spatial modes a and b having opposite photonic qubit states, and the last two states are correlated with single photons

Photonic State	Atomic State	Probability
$\left(\|0\rangle_a^\alpha\|1\rangle_a^\beta\right)\left(\|1\rangle_b^\alpha\|0\rangle_b^\beta\right)$	$\|\Psi^{\beta\alpha}\rangle_{ab}$	$p^2p_e^2(\cos^2\theta_a\sin^2\theta_b\cos^4\frac{\chi}{2}+\sin^2\theta_a\cos^2\theta_b\sin^4\frac{\chi}{2})$
	$\|M\rangle_a\|M\rangle_b$	$p^2\left\{\frac{1}{4}p_{bg}^2(1+\frac{\sin^2\chi}{2})+\frac{1}{2}p_{bg}p_e[1+(\cos 2\theta_a-\cos 2\theta_b)\frac{\cos\chi}{2}]\right.$ $+p_{2e}p_{bg}(1-\frac{\sin^2\chi}{2})+p_{2e}p_e[1-\frac{\sin^2\chi}{2}+(\cos 2\theta_a-\cos 2\theta_b)\frac{\cos\chi}{2}]$ $\left.+\frac{1}{4}p_{2e}\sin^2\chi\right\}$
$\left(\|1\rangle_a^\alpha\|0\rangle_a^\beta\right)\left(\|0\rangle_b^\alpha\|1\rangle_b^\beta\right)$	$\|\Psi^{\alpha\beta}\rangle_{ab}$	$p^2p_e^2(\cos^2\theta_a\sin^2\theta_b\sin^4\frac{\chi}{2}+\sin^2\theta_a\cos^2\theta_b\cos^4\frac{\chi}{2})$
	$\|M\rangle_a\|M\rangle_b$	$p^2\left\{\frac{1}{4}p_{bg}^2(1+\frac{\sin^2\chi}{2})+\frac{1}{2}p_{bg}p_e[1-(\cos 2\theta_a-\cos 2\theta_b)\frac{\cos\chi}{2}]\right.$ $+p_{2e}p_{bg}(1-\frac{\sin^2\chi}{2})+p_{2e}p_e[1-\frac{\sin^2\chi}{2}-(\cos 2\theta_a-\cos 2\theta_b)\frac{\cos\chi}{2}]$ $\left.+\frac{1}{4}p_{2e}\sin^2\chi\right\}$
$\left(\|1\rangle_a^\alpha\|1\rangle_a^\beta\right)\left(\|0\rangle_b^\alpha\|0\rangle_b^\beta\right)$	$\|\Psi^{\alpha\beta}\rangle_{aa}$	$\frac{1}{4}p^2p_e^2(\cos^2\theta_a\sin^2\theta_b+\sin^2\theta_a\cos^2\theta_b)\sin^2\chi$
	$\|M\rangle_a\|M\rangle_b$	$\frac{1}{2}p^2[\frac{1}{2}p_{bg}^2(2-\frac{\sin^2\chi}{2})+p_{bg}p_e+p_{2e}(p_{bg}+p_e)\sin^2\chi+p_{2e}(1-\frac{\sin^2\chi}{2})]$
$\left(\|0\rangle_a^\alpha\|0\rangle_a^\beta\right)\left(\|1\rangle_b^\alpha\|1\rangle_b^\beta\right)$	$\|\Psi^{\alpha\beta}\rangle_{bb}$	$\frac{1}{4}p^2p_e^2(\cos^2\theta_a\sin^2\theta_b+\sin^2\theta_a\cos^2\theta_b)\sin^2\chi$
	$\|M\rangle_a\|M\rangle_b$	$\frac{1}{2}p^2[\frac{1}{2}p_{bg}^2(2-\frac{\sin^2\chi}{2})+p_{bg}p_e+p_{2e}(p_{bg}+p_e)\sin^2\chi+p_{2e}(1-\frac{\sin^2\chi}{2})]$
$\left(\|0\rangle_a^\alpha\|1\rangle_a^\beta\right)\left(\|0\rangle_b^\alpha\|1\rangle_b^\beta\right)$	$\|\downarrow\rangle_a\|\downarrow\rangle_b$	$p^2p_e^2\cos^2\theta_a\cos^2\theta_b\cos^2\chi$
	$\|M\rangle_a\|M\rangle_b$	$p^2\left\{\frac{1}{4}p_{bg}^2+\frac{1}{4}p_{bg}p_e(\cos^2\theta_a+\cos^2\theta_b)(1+\cos^2\chi)\right.$ $\left.+p_{2e}[p_{bg}+p_e(\cos^2\theta_a+\cos^2\theta_b)]\cos^2\chi+\frac{1}{4}p_{2e}\sin^2\chi\right\}$
$\left(\|1\rangle_a^\alpha\|0\rangle_a^\beta\right)\left(\|1\rangle_b^\alpha\|0\rangle_b^\beta\right)$	$\|\uparrow\rangle_a\|\uparrow\rangle_b$	$p^2p_e^2\sin^2\theta_a\sin^2\theta_b\cos^2\chi$
	$\|M\rangle_a\|M\rangle_b$	$p^2\left\{\frac{1}{4}p_{bg}^2+\frac{1}{4}p_{bg}p_e(\sin^2\theta_a+\sin^2\theta_b)(1+\cos^2\chi)\right.$ $\left.+p_{2e}[p_{bg}+p_e(\sin^2\theta_a+\sin^2\theta_b)]\cos^2\chi+\frac{1}{4}p_{2e}\sin^2\chi\right\}$

Table 3.2: Quantum states of photon modes and atomic qubits. Listed is the resulting quantum state given that two atom-photon systems are prepared according to Table 3.1, and the photon modes are coupled on a beam splitter of reflectivity $R = \chi/\pi$. Only those states with two single photons emerging in distinct modes are written, with their associated probabilities. Higher order processes in the probabilities p, p_{bg}, and p_{2e} are not listed.

emerging in the same output port of the BS, again with opposite photonic qubit states. As shown in Figure 3.1(d) for the case of polarization photonic qubit states, these four outcomes can be uniquely determined by separating the photonic qubit states at the output of each BS output port and triggering on the relevant two-photon coincidence event.

For a 50/50 BS ($\chi = \pi/2$), the above states simplify to one of the following entangled states:

$$|\Psi^{\text{ent}}\rangle_{\text{diff}} = \mathcal{N}(\cos\theta_a \sin\theta_b |\downarrow\rangle_a |\uparrow\rangle_b - \sin\theta_a \cos\theta_b |\uparrow\rangle_a |\downarrow\rangle_b) \quad (3.11)$$

$$|\Psi^{\text{ent}}\rangle_{\text{same}} = \mathcal{N}(\cos\theta_a \sin\theta_b |\downarrow\rangle_a |\uparrow\rangle_b + \sin\theta_a \cos\theta_b |\uparrow\rangle_a |\downarrow\rangle_b) \quad (3.12)$$

where $\mathcal{N}$ is a normalization constant and the subscripts "diff" and "same" refer to cases where the two photons emerged in different spatial modes or the same spatial mode but separate photonic qubit states. As mentioned previously, if the two atoms are originally prepared in arbitrary states given by θ_a and θ_b [Figure 2.1(f)], this post-selection process can amount to a "measurement gate" between the two atom. This gate corresponds to a quantum nondemolition measurement of the operator $Z_a Z_b$, where Z_i stands for the z component of the Pauli matrix associated with atomic qubit i. [49]. For $\theta_a = \theta_b$ (identically-prepared atoms), the above states simplify to the odd-parity Bell states $|\Psi^-\rangle_{\text{atom}} = (|\downarrow\rangle_a |\uparrow\rangle_b - |\uparrow\rangle_a |\downarrow\rangle_b)/\sqrt{2}$ and $|\Psi^+\rangle_{\text{atom}} = (|\downarrow\rangle_a |\uparrow\rangle_b + |\uparrow\rangle_a |\downarrow\rangle_b)/\sqrt{2}$ respectively[1].

Including noise from background counts and double excitations, we find that when two photons are detected in coincidence in the desired output ports of the BS (for either the $|\Psi^{\text{ent}}\rangle_{\text{diff}}$ or the $|\Psi^{\text{ent}}\rangle_{\text{same}}$ state), the post-selected mixed state of the two atoms alone becomes:

[1] As can be seen from Equations 3.11, 3.12, and 3.14, one cannot use this entanglement protocol for $\theta_a = \theta_b = 0$ or $\pi/2$. However, this limitation is acceptable for scalable quantum computing using the methods described in references [89] and [47]

$$\rho_{\rm post} = P_{\rm good}|\Psi^{\rm ent}\rangle\langle\Psi^{\rm ent}| + P_{\rm bad}|M_aM_b\rangle\langle M_aM_b| \tag{3.13}$$

where the probabilities of a desired entangled state $P_{\rm good}$ and the noisy mixed state $P_{\rm bad}$ are given by:

$$P_{\rm good} = \frac{1}{4}p^2p_e^2(\cos^2\theta_a\sin^2\theta_b + \sin^2\theta_a\cos^2\theta_b) \tag{3.14}$$

$$P_{\rm bad} = \frac{p^2}{2}\left[p_{bg}\left(\frac{3}{4}p_{bg}+p_e\right) + p_{2e}\left(p_{bg}+p_e+\frac{1}{2}\right)\right]. \tag{3.15}$$

The above probabilities do not add to one because they are relative to the (most probable) null case of not detecting photons in each of the output modes of the BS. Nevertheless, we can calculate a lower limit on the fidelity of the heralded entangled atomic qubit state, most importantly for the maximally-entangled Bell states $|\Psi^-\rangle_{\rm atom}$ and $|\Psi^+\rangle_{\rm atom}$ ($\theta_a = \theta_b = \pi/4$). Noting that the fidelity of the random mixed state $|M_aM_b\rangle$ is 1/4, the fidelity of the post-selected state is

$$\mathcal{F} = \frac{P_{\rm good}+\frac{1}{4}P_{\rm bad}}{P_{\rm good}+P_{\rm bad}} = \frac{p_e^2 + \left[p_{bg}\left(\frac{3}{4}p_{bg}+p_e\right) + p_{2e}\left(p_{bg}+p_e+\frac{1}{2}\right)\right]}{p_e^2 + 4\left[p_{bg}\left(\frac{3}{4}p_{bg}+p_e\right) + p_{2e}\left(p_{bg}+p_e+\frac{1}{2}\right)\right]}\,. \tag{3.16}$$

One criterion for the generation of entanglement is that the fidelity be greater than 1/2, which leads to the condition that $P_{\rm good} > P_{\rm bad}/2$ or

$$p_e^2 > 2p_{bg}\left(\frac{3}{4}p_{bg}+p_e\right) + 2p_{2e}\left(p_{bg}+p_e+\frac{1}{2}\right). \tag{3.17}$$

It is clear that when using a weak excitation pulse of duration $t_e > \tau$, the entanglement fidelity is severely limited ($P_{\rm bad} \approx P_{\rm good}$) since $p_{2e} = p_e^2/2$. However, when using ultrafast excitation pulses such that $p_e \to 1$ and $p_{2e} \to 0$, only the background photons can affect the resulting fidelity: $\mathcal{F} \sim 1 - 3p_{bg}$.

CHAPTER IV

Trapped Ions

For quantum information processing, there are two primary types of trapped ion qubits: optical qubits derived from a ground state and an excited metastable state separated by an optical frequency [90], and hyperfine qubits derived from electronic ground-state hyperfine levels separated by a microwave frequency [55]. With hyperfine qubits, single qubit manipulations can be performed using microwave pulses tuned to the hyperfine splitting between the qubit states. In comparison, optical qubits require phase-stable narrow-linewidth lasers to couple the two qubit levels, which can be very difficult to maintain. Another difficulty with optical qubits is their qubit coherence times which are fundamentally limited by the lifetime of the excited metastable state, typically on the order of seconds (and the longer the lifetime, the narrower the required linewidth of the qubit rotation laser). In contrast, hyperfine qubit levels are stored in electronic ground states, and thus lifetime is not an issue. With either qubit, magnetic field perturbations to internal structure can be important. Therefore, the coherence between two internal levels should be made magnetic field-insensitive (to lowest order), which is possible by operating near an extremum of the energy separation between the two levels with respect to the magnetic field. In this regard, hyperfine qubit coherence times have been measured to

exceed 10 min in the context of trapped ion frequency standards [91, 92].

While protocols exist for remote-ion entanglement using optical qubits [73], as mentioned in previous chapters, my work focuses on the hyperfine qubit. This choice is primarily due to the ease of qubit state manipulations and the potential for very long qubit coherence times. Additionally, each particular isotope of our ion — $^{111}Cd^+$ and $^{171}Yb^+$ — is chosen because it has a nuclear spin $I = 1/2$, simplifying the atomic physics of the system by minimizing hyperfine structure.

4.1 The Cadmium Ion

The first ion used in my experiments is the cadmium ion. Figure 4.1 displays the relevant energy levels of $^{111}Cd^+$, where the two hyperfine ground states $^2S_{1/2}$ $|F = 0, m_F = 0\rangle \equiv |\uparrow\rangle$ and $^2S_{1/2}$ $|F = 1, m_F = 0\rangle \equiv |\downarrow\rangle$ comprise the atomic qubit and have a frequency separation of $\omega_{HF}/2\pi \approx 14.5$ GHz. These two states are chosen because they are magnetic-field insensitive to second order. However, one of the major reasons cadmium was chosen in general as the ion for our group was because of the simple atomic structure. Because of the $I = 1/2$ nuclear spin and because of the absence of low lying metastable states, cadmium has perhaps the simplest atomic structure of any ion system used for quantum information. Unfortunately nothing comes without its difficulties, and one difficulty for cadmium is the resonant wavelength of 214.5 nm for the $^2S_{1/2} \leftrightarrow {}^2P_{3/2}$ transition. Such short wavelengths require frequency quadrupling infrared lasers and result in limited laser power (as discussed more in Section 4.2).

4.1.1 Trapping Cadmium ions In our group, cadmium ions were originally loaded by electron bombardment of neutral cadmium atoms — a beam of neutral cadmium atoms and a beam of electrons intersecting in the trapping region. When an electron

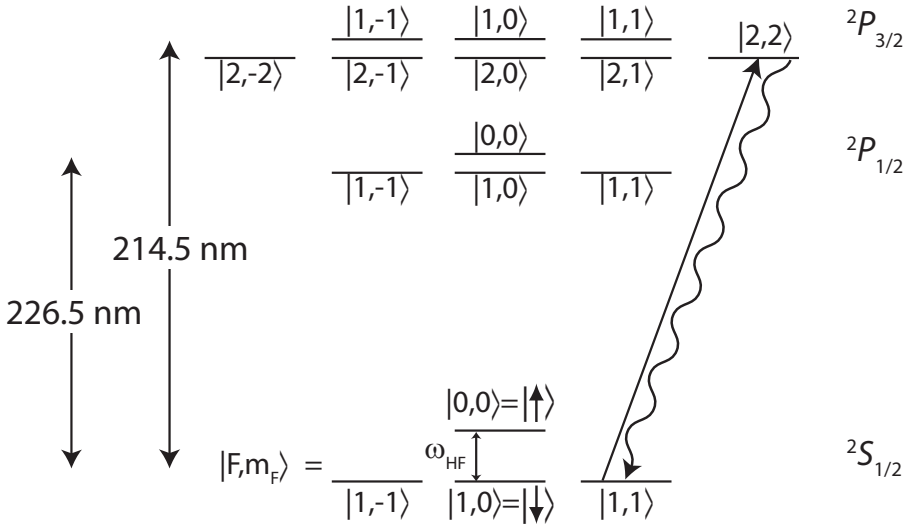

Figure 4.1: Energy levels of the $^{111}Cd^+$ ion. The $^2S_{1/2}$ $|F = 0, m_F = 0\rangle$ and $^2S_{1/2}$ $|F = 1, m_F = 0\rangle$ hyperfine ground states, separated in frequency by $\omega_{HF}/2\pi \approx 14.5$ GHz, and magnetic field insensitive to first order, form the basis of the atomic qubit. Detection of the internal HF state is accomplished by illuminating the ion with a σ^+-polarized "detection" beam near 214.5 nm and observing the fluorescence from the cycling transitions between the $F = 1$ manifold and the $^2P_{3/2}$ $|F = 2, m_F = 2\rangle$ state.

from the electron beam struck a neutral atom in this region, an electron would be ejected from the cadmium atom creating the Cd^+ ion. While this technique worked quite well for loading clouds of ions, it was difficult to load only a single ion. This was in part due to the increased local pressure in the vacuum chamber in the area of the ion trap, due to the high energy electrons. This increased pressure also limited trapping times.

With the introduction of ultrafast lasers in the lab, we gained the ability to photoionize the cadmium atoms. Photoionization not only allows for maintaining a low pressure within the trapping region, but also has a much higher efficiency [93]. This is accomplished by using a mode-locked Ti:Sapphire laser. This laser is frequency-quadrupled from a central wavelength of 915.5 nm to 228.9 nm for excitation of the neutral Cd atom (Figure 4.2a). This commercial pulsed laser (Spectra-Physics Tsunami) provides pulses of light with a pulse duration of ~ 1 ps (psec laser). With

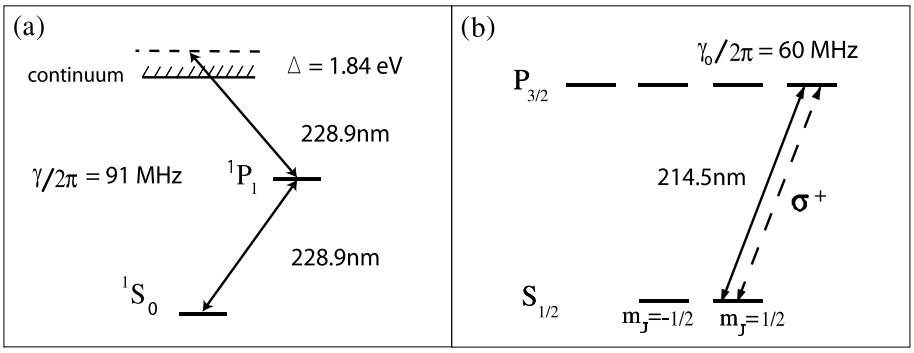

Figure 4.2: Relevant energy levels for photoionization of cadmium atoms. (a) Relevant energy levels for the neutral Cd atom. From the two-electron $^1S_0$ ground state, the intermediate excited $5s5p\ ^1P_1$ state (radiative linewidth $\gamma/2\pi = 91$ MHz) is populated with a pulsed laser near $\lambda = 228.9$ nm. This state is well above the midpoint of the energy difference between the $5s^2\ ^1S_0$ ground state and the continuum, so the same laser can subsequently ionize the atom. (b) Relevant energy levels for even isotopes of the Cd^+ ion. A continuous wave laser tuned red of the $^2S_{1/2} \leftrightarrow {}^2P_{3/2}$ cycling transition near $\lambda = 214.5$ nm (radiative linewidth of $\gamma_o/2\pi = 60$ MHz) provides Doppler cooling of the motion for the newly formed ions and localizes them to the center of the rf trap.

this laser tuned to the intermediate resonance in the neutral Cd atom, the atom can be excited to the $^1P_1$ state of Cd from where the excited electron can be promoted directly to the continuum via a single photon transition with either the psec laser or the cw laser used for Doppler cooling the resulting ion (Figure 4.2(b)). The large bandwidth of the psec laser also allows for ionization of all velocity classes of atoms in a vapor or atomic beam and can provide nearly perfect ion trap loading efficiency [93].

The psec laser produces pulse energies up to 12 nJ at 915 nm. A second-harmonic-generation autocorrelator is used to measure the pulse duration of approximately 2 ps. The infrared pulses are frequency-doubled in a 12 mm long lithium borate (LBO) crystal and doubled again in a 10 mm long $\beta-$barium borate (BBO) crystal. Each nonlinear crystal is critically phase-matched (angle-tuned) at its corresponding wavelength. The frequency-quadrupled output at 228.9 nm consists of pulses of approximate duration $\tau \approx 1$ ps with energies up to 60 pJ in the trapping region. The bandwidth of the psec laser pulses in the ultraviolet is indirectly determined by tuning

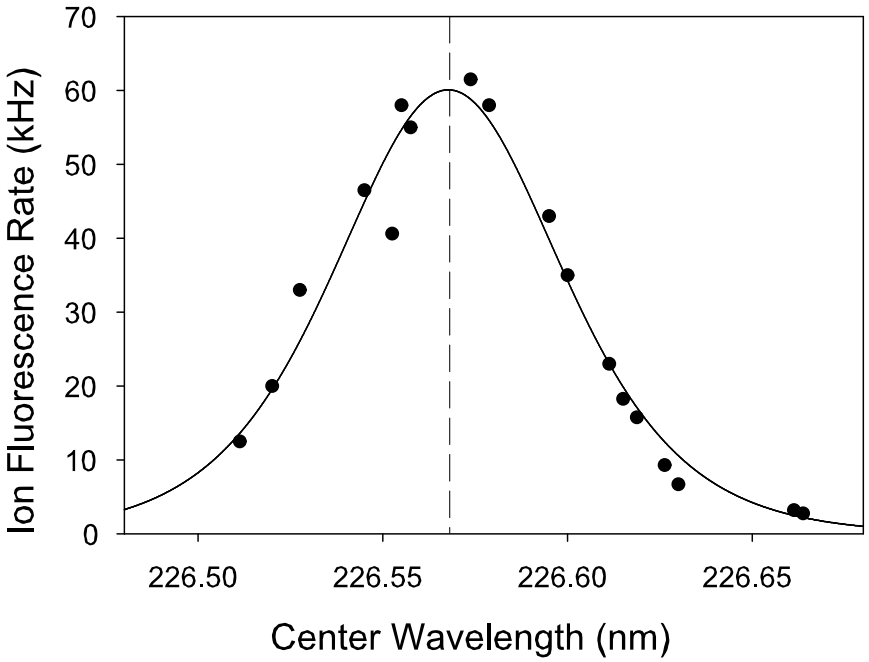

Figure 4.3: Fluorescence spectrum of a single trapped $^{111}Cd^{+}$ ion excited with an ultrafast laser. The spectrum is measured as the center frequency of the psec laser is scanned [94]. The observed 0.07 nm (400 GHz) bandwidth is consistent with a transform-limited pulse of duration $\tau \approx 1$ ps. The dashed line indicates the expected resonance position of the $^2S_{1/2} \rightarrow ^2 P_{1/2}$ transition in $^{111}Cd^{+}$ at 226.57 nm.

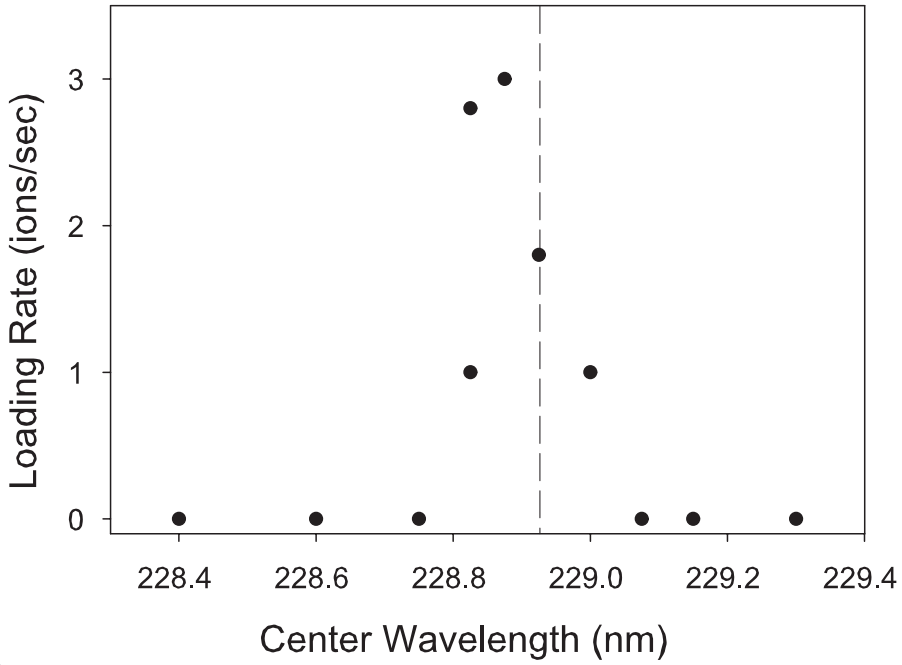

Figure 4.4: Loading rate of Cd^+ ions vs. detuning of the psec photoionization laser. Loading is via the neutral Cd $^1S_0 \rightarrow {}^1P_1$ transition at 228.9 nm. The laser repetition rate is 81 MHz, and each pulse has an approximate duration 1 ps and energy of 60 pJ. The loading rate tracks the spectrum of the psec laser, with a bandwidth of approximately 400 GHz. The dashed line indicates the expected resonance position of the $^1S_0 \rightarrow {}^1P_1$ transition in neutral Cd near 228.9 nm.

it to the nearby $^2S_{1/2} \leftrightarrow^2 P_{1/2}$ transition in Cd^+ at 226.5 nm (fundamental infrared laser center wavelength at 906 nm) and measuring the trapped ion fluorescence rate [94]. Figure 4.3 displays the fluorescence level of a single ion from the quadrupled psec laser tuned near this transition at 226.5 nm . The resulting ultraviolet bandwidth of 0.07 nm (400 GHz) is consistent with the autocorrelator measurements extrapolated from the infrared. We expect a very similar spectrum when the laser is tuned to 915 nm and quadrupled to the $^1S_0 \rightarrow {}^1P_1$ neutral Cd atom resonance, verified in Figure 4.4. Once ionized, a Cd^+ ion is Doppler cooled by the cw laser tuned red of the $^2S_{1/2} \leftrightarrow {}^2P_{3/2}$ cycling transition near 214.5 nm (radiative linewidth of 60 MHz [95]) and localizes the ion to the center of the radio frequency (rf) trap (Figure 4.2b).

4.1.2 Cadmium as a qubit For quantum information processing, the qubit must first be initialized to a known state. Light resonant with the $^2S_{1/2}F = 1 \leftrightarrow {}^2P_{3/2}F = 1$ transition is used to initialize the ion to the $|\uparrow\rangle$ state via optical pumping. As this resonance is only ≈ 626 MHz away from the cooling transition [65], an acousto-optic modulator (AOM) can be used to tune the 214.5 nm laser light to the appropriate frequency (Figure 4.1). Once the ion decays into the $|\uparrow\rangle$ qubit state, this optical pumping laser is detuned from any resonance by 14.5 GHz. Hence, once in the $|\uparrow\rangle$ state, the ion remains there with an extremely high probability.

After initialization in the $|\uparrow\rangle$ state, the ion can be rotated between $|\uparrow\rangle$ and $|\downarrow\rangle$ via microwaves resonant with the hyperfine splitting of 14.5 GHz. Rotations between the different Zeeman levels ($|1,-1\rangle$ and $|1,1\rangle$) can also be driven because these levels have resolved energy splittings due to an applied magnetic field. For small magnetic fields, the Zeeman levels shift linearly at ≈ 1.4 MHz/Gauss.

For qubit state detection, a σ^+-polarized beam resonant with the $^2S_{1/2}F = 1 \leftrightarrow {}^2P_{3/2}F = 2$ transition is sent onto the ion and the number of scattered pho-

tons detected a PMT is recorded. The $|\downarrow\rangle$ state is resonant with the applied light and is pumped to the ${}^2S_{1/2}|1,1\rangle \leftrightarrow {}^2P_{3/2}|2,2\rangle$ cycling transition which scatters many photons, whereas the $|\uparrow\rangle$ state is detuned by roughly 13.9 GHz and is therefore not likely to scatter photons. In the $^{111}Cd^+$ qubit, a detection efficiency of up to 99.7% was reported in [96].

4.2 The Ytterbium Ion

The second ion species used in our experiments is the ytterbium ion, which has certain advantages and disadvantages over the cadmium system. The major advantage of ytterbium is the relatively long resonant wavelength at 369.5 nm (in comparison to the 214.5 nm resonant wavelength of Cd^+). One reason this long wavelength is advantageous is because high power lasers are readily available, which is in contrast to the lower laser powers available with frequency quadrupled laser systems at 214.5 nm. As shown in Section 7.1, the available power at 214.5 nm in the ultrafast psec laser was only sufficient for driving a single π pulse between the S and P levels in cadmium. However, twice as much power would have been necessary for the simultaneous excitation of two ions in two separate vacuum chambers. In addition to high laser powers, the long resonant wavelengths of the ytterbium ion allow for the use of single-mode fibers with relatively low losses. As will be shown in Chapter VIII, this feature is essential for remote-ion entanglement.

Certainly, ytterbium also has its downsides — more complicated atomic structure requiring more lasers and resulting in more complex atomic transitions — but the high power associated with only frequency doubling the main 739 nm laser and the use of single-mode fibers at 369.5 nm made the switch to ytterbium very favorable.

In this section, I discuss the high-efficiency preparation and measurement of qubits

stored in the hyperfine ground states of Yb^+. Although the ytterbium ion system has previously been exploited by many groups for high-resolution spectroscopic studies because of its metastable D and F states [97, 98, 99, 100, 101, 102, 103], our group is one of the first to demonstrate the use of the Yb^+ qubit for quantum information protocols. A key component of the setup is the stabilization of all lasers to a molecular iodine spectrometer at a wavelength of 739 nm. Additionally, since the ytterbium and cadmium systems are so similar, many of the techniques developed in cadmium are applicable to the ytterbium system.

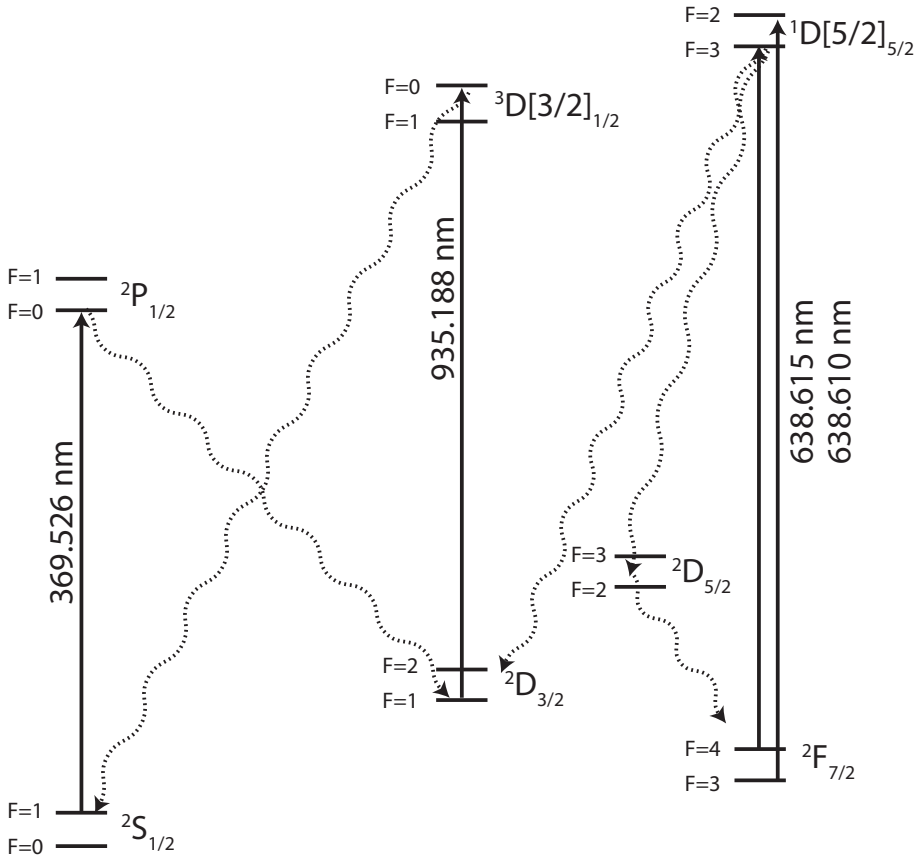

Figure 4.5: Partial level scheme of $^{171}Yb^+$. The $^2S_{1/2}F = 1 \leftrightarrow {}^2P_{1/2}F = 0$ transition at 369.526 nm is used for Doppler cooling. The transition probability from $^2P_{1/2}F = 0$ to the low-lying metastable $^2D_{3/2}$ state is $\sim$.005 [104], and the population of this state is repumped into the cooling cycle via laser radiation at 935.188 nm through the $^3D[3/2]_{1/2}$ level. The ion also reaches $^2F_{7/2}$ on the order of a few times per hour, and is repumped with light at 638.615 nm and 638.610 nm.

4.2.1 Trapping Ytterbium ions As with the cadmium system, ytterbium ions are loaded using photoionization. However, as the neutral ytterbium resonance is at a wavelength accessible directly by laser diodes, we use cw excitation of the Yb atoms rather than the psec laser[1]. To load a Yb^+ ion into the rf trap, the cw diode laser with a power of ∼5 mW is tuned to the $^1S_0 \leftrightarrow {}^1P_1$ transition of neutral Yb near 399 nm and has a focal spot size of ∼40 μm at the center of the trap. This beam is aligned with a counter-propagating beam tuned near 369.5 nm resonant with the $^2S_{1/2} \leftrightarrow {}^2P_{1/2}$ transition of the ion (Figure 4.5). The photon from the 369.5 nm laser beam has enough energy to promote the excited electron directly to the continuum. A thermal beam of Yb atoms is sent through the trap[2], and the Yb atoms are ionized by way of a resonant two-photon transition [105]. The neutral Yb beam and the 399 nm beam are approximately perpendicular to minimize Doppler shifts and allow for isotopically selective loading (a technique not available with the large bandwidth of the psec laser). About 10 mW of 935 nm and about 2 mW of 638 nm light are also directed into the trapping region from an optical fiber. These light sources prevent the ion from being trapped in the metastable $^2D_{3/2}$ and $^2F_{7/2}$ states, respectively (Figure 4.5). The mean storage time of a trapped ion is several days.

For cooling ytterbium ions, I first explain the relevant transitions for an even isotope of ytterbium without hyperfine structure, and then I discuss of the additional requirements for the hyperfine levels of $^{171}Yb^+$. The 369.5 nm transition from $^2S_{1/2} \leftrightarrow {}^2P_{1/2}$ is used to generate resonance fluorescence and Doppler cool the ion.

[1]Since photoionization with the psec laser proved to be so successful for cadmium, we first loaded ytterbium ions using this laser. This required tuning the psec laser to twice the resonant wavelength at 797.8 nm and frequency doubling the pulses to 398.9 nm. As expected, the psec laser loading method is much more efficient than the cw method, however, with trapping times of days, the cw method is more than sufficient.

[2]The ovens producing the atomic Yb beam needs to be heated to generate a sufficient flux of atoms to load. In comparison, the vapor pressure of Cd at room temperature is high enough to load exclusively from the background gas (see Appendix B). While the low vapor pressure in ytterbium requires the ovens to be fired for loading, the absence of a ytterbium background gas leads to less collisions with ytterbium atoms that can lead to ejection from the trap or charge exchange.

This light is generated by a frequency doubled amplified 739 nm cw diode laser that is stabilized to a molecular iodine reference. Instead of a frequency doubled laser, one could also use a direct diode [106], however in our experiments, a frequency doubled laser is used because the commercially available infrared lasers have more power, longer lifetimes, and allow for locking to iodine. From the $^2P_{1/2}$ state, the branching ratio into the metastable $^2D_{3/2}$ state, of lifetime $\sim$ 26 ms [107], is $\sim$0.005 [104]. A closed system is formed by pumping the ion from the $^2D_{3/2}$ state to the $^3D[3/2]_{1/2}$ state with 935 nm light [97]. From $^3D[3/2]_{1/2}$, the ion will decay directly to $^2S_{1/2}$ (or back to $^2D_{3/2}$). A few times per hour, the ion also finds its way into the extremely long-lived $^2F_{7/2}$ state. Reference [108] speculates that the $^2F_{7/2}$ state is occupied following a collision between the excited Yb^+ ion and an atom in the background gas. Alternatively, it may be due to an off resonant transition from the $^2D_{3/2}$ state[3]. However the ion gets into the $^2F_{7/2}$ state, this state depopulated by pumping the ion to the $^1D[5/2]_{5/2}$ level via laser radiation at 638 nm from where it will decay back into the closed cooling cycle. Alternatively as pointed out in reference [99], an 864 nm laser could also be used by pumping the ion back to the cycling transition through the $^3D[5/2]_{3/2}$ level. As this laser wavelength is similar to the fundamental laser wavelength for cadmium at 858 nm, we first tuned one of the cadmium lasers up to 864 nm to pump out of the $^2F_{7/2}$ state (see Appendix B). In the end, however, we purchased a 638 nm diode laser, as this option was shown to be more effective in reference [99]. In addition to getting stuck in the $^2F_{7/2}$ state, the ion also goes into a "dark state" on the order of a few times per hour, where the 638 nm laser will not bring it back to the cooling cycle. This is likely due to molecule formation, and application of a strong beam of 369.5 nm laser light of roughly 1 mW breaks the

[3]We have found that the $^2F_{7/2}$ state can be prepared rather efficiently by blocking the 935 nm laser and hitting the ion with the 399 nm cw laser light.

molecular bond such that the ion is again visible.

The hyperfine structure of $^{171}Yb^{+}$ (Figure 4.5) necessitates a few more laser frequencies in order to efficiently cool the ion. The 369.5 nm laser is tuned to the $^2S_{1/2}F = 1 \leftrightarrow {}^2P_{1/2}F = 0$ transition and the 935 nm laser is tuned to the $^2D_{3/2}F = 1 \leftrightarrow {}^3D[3/2]_{1/2}F = 0$ transition for Doppler cooling. However, off-resonant excitation of the ion to the $^2P_{1/2}F = 1$ level allows the ion to decay into the $F = 0$ state of $^2S_{1/2}$ or $F = 2$ manifold of $^2D_{3/2}$. Electro-optic modulators (EOMs) add sidebands to the lasers in order to pump out of these dark states back into the Doppler cooling cycle. For the $^2S_{1/2} \leftrightarrow {}^2P_{1/2}$ transition, the 369.5 nm laser passes through a 7.35 GHz EOM, such that the 14.7 GHz second sideband is resonant with the $^2S_{1/2}F = 0 \leftrightarrow {}^2P_{1/2}F = 1$ transition. For the $^2D_{3/2} \leftrightarrow {}^3D[3/2]_{1/2}$ transition, a fiber EOM adds the -3.06 GHz sideband to the 935 nm laser to be resonant with the $^2D_{3/2}F = 2 \leftrightarrow {}^3D[3/2]_{1/2}F = 1$ transition. Finally, the 638 nm laser is switched between 638.615 nm and 638.610 nm at a rate of about 1 Hz by adjusting the diode current and grating directly. This allows for the ion to be pumped out of both hyperfine levels of $^2F_{7/2}$. For more precise numbers on these wavelengths, see Appendix B.

4.2.2 Ytterbium Laser Stabilization Efficient Doppler cooling and qubit state detection require the 739 nm and 935 nm lasers to be stable in frequency to well within the linewidths of the relevant transitions in the experiment. For this, the 739 nm laser is locked to a stable cavity using an rf lock [109, 110] that allows for reduction of fast laser noise. We then use saturated-absorption spectroscopy of iodine to stabilize the cavity on a long time-scale to an absolute frequency reference. Lastly, the 935 nm laser frequency is stabilized using a side-of-fringe lock in the same cavity.

The relevant optics and electronics for the rf stabilization of the 739 nm laser to the cavity are shown in Figure 4.6. From the main 500 mW beam, a $\lambda/2$-waveplate

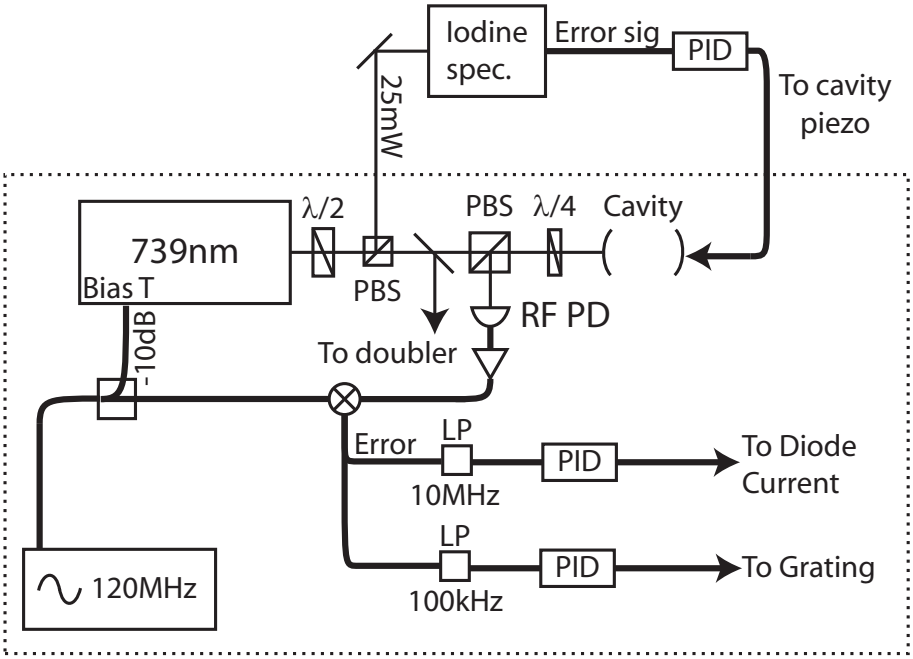

Figure 4.6: Experimental apparatus for locking the 739 nm laser to an iodine stabilized cavity. 25 mW is diverted from the main 500 mW beam by a half waveplate and a polarizing beam splitter (PBS) into the iodine lock as shown in Figure 4.7 from where the signal is sent to a proportional-integral-derivative servo controller (PID), the output of which is sent to a cavity piezo. An additional 2 mW of the main beam is sent to a stable reference cavity. The cavity reflection is measured with a radio-frequency photodiode (RF PD), and this signal is sent through an amplifier and mixed with the 120 MHz signal modulating the Bias T of the laser. The lock operates by adjusting both the laser grating and diode current. Because movement of the laser grating cannot adjust the frequency as quickly as changing the laser diode current, the signal for each is generated using two different low pass filters followed by a PID.

and a polarizing beam splitter (PBS) divert 25 mW for the iodine lock. The signal from the iodine lock is then directed to a proportional-integral-derivative (PID) servo controller, the output of which is directed to a cavity piezo. An additional ~ 2 mW of the 739 nm beam is sent onto the cavity (which is made of invar to be less sensitive to temperature fluctuations). The cavity reflection is measured with a radio-frequency photodiode, and this signal is sent through an amplifier and mixed with the 120 MHz signal modulating the current of the laser.

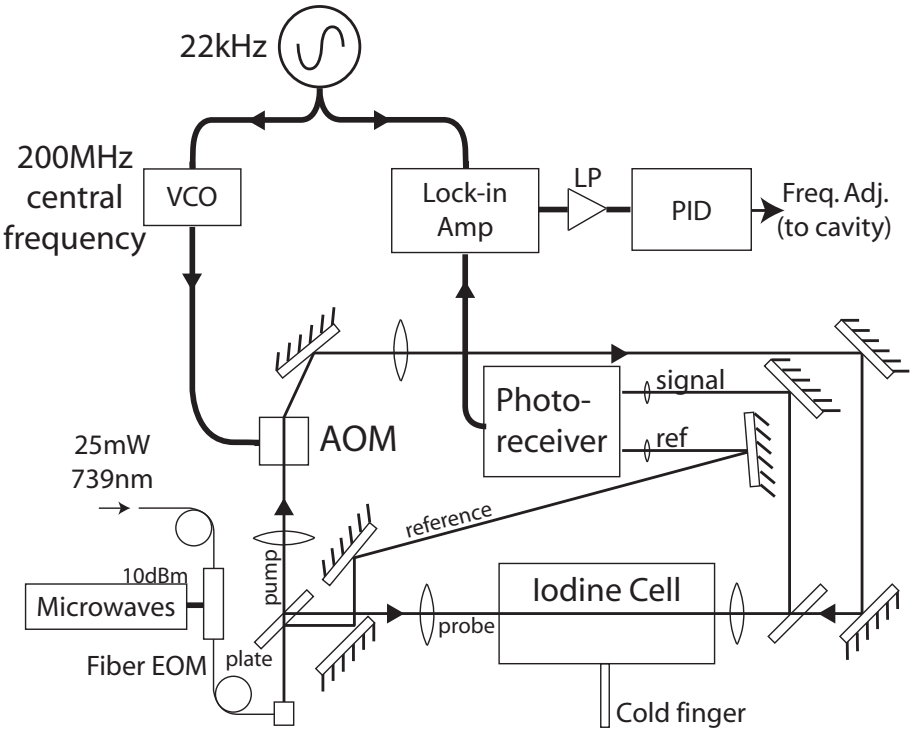

Figure 4.7: Setup for locking to molecular iodine via saturated absorption spectroscopy. About 25 mW of 739 nm light is incident on the fiber-coupled electro-optic modulator (EOM) and 10 mW of this light is coupled through the fiber. Approximately 1/3 of this is transfered into the first sideband, providing 3.5 mW to split into the reference, probe, and pump beams. A voltage-controlled oscillator (VCO) with a central frequency of 200 MHz is modulated by 22 kHz and sent into an AOM to modulate the pump beam. A lock-in amplifier mixes the 22 kHz signal with the signal from the photoreceiver, sending the output through a low pass filter (LP) and finally to a proportional-integral-derivative controller (PID) which outputs the error signal to the cavity.

Iodine is often chosen as a frequency reference for wavelengths from the near IR to the disassociation limit at 499.5 nm because of the density of narrow absorption lines in these regions [111, 112]. These absorption lines can serve as excellent frequency

references for laser stabilization to a few parts in 10^{-9} or better. However, in the region applicable to Yb^+ (739 nm), most of the lines are weak, and the iodine must be heated to over 600K in order to effectively populate the vibrational levels of the molecule that are the lower states of these transitions (Figure 4.9). We use an iodine cell 20 cm in length with two quartz windows 25 mm in diameter and a 5 cm long cold finger[4]. The cold finger is isolated such that it remains at room temperature ($\sim 24\,^{\circ}\mathrm{C}$), which is important for limiting the iodine pressure in the cell (Figure 4.8). This is necessary to avoid collisional broadening of the signal due to the high iodine pressure.

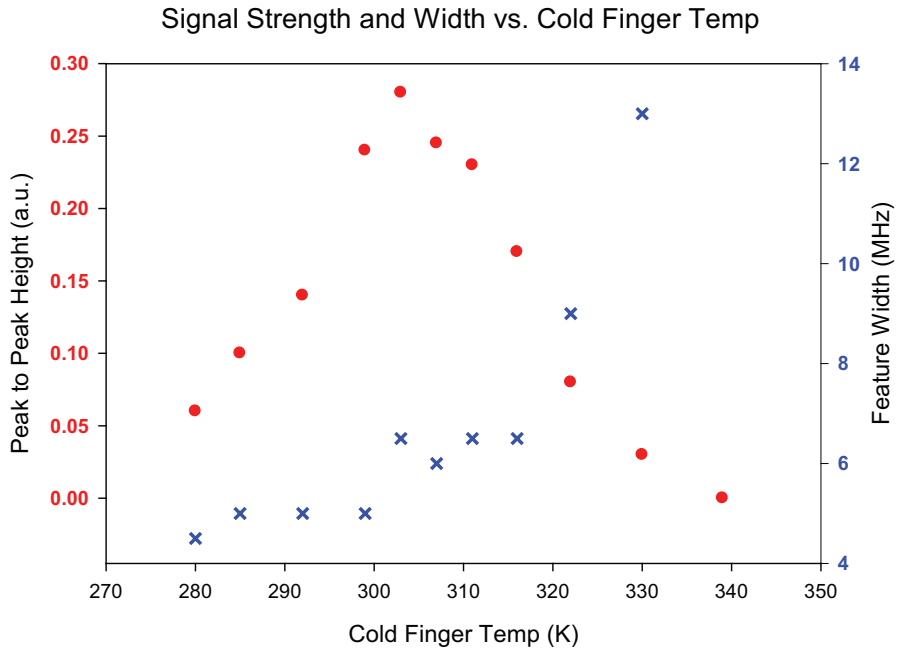

Figure 4.8: Lock signal as a function of cold finger temperature.

Figure 4.7 shows the apparatus for stabilizing the cavity to the iodine via saturated absorption spectroscopy. The 739 nm diode laser produces about 500 mW of output power, 25 mW of which is sent through a fiber EOM as shown in Figures 4.6 and 4.7.

[4]This glass cell was made in house by the university glassblower, it was cleaned with acetone, a small crystal of iodine was placed in the cell, pumped down to roughly 10^{-6} Torr and pinched off with a torch. While this cell is certainly not spectroscopic grade, it is sufficient for the locking requirements in our experiments.

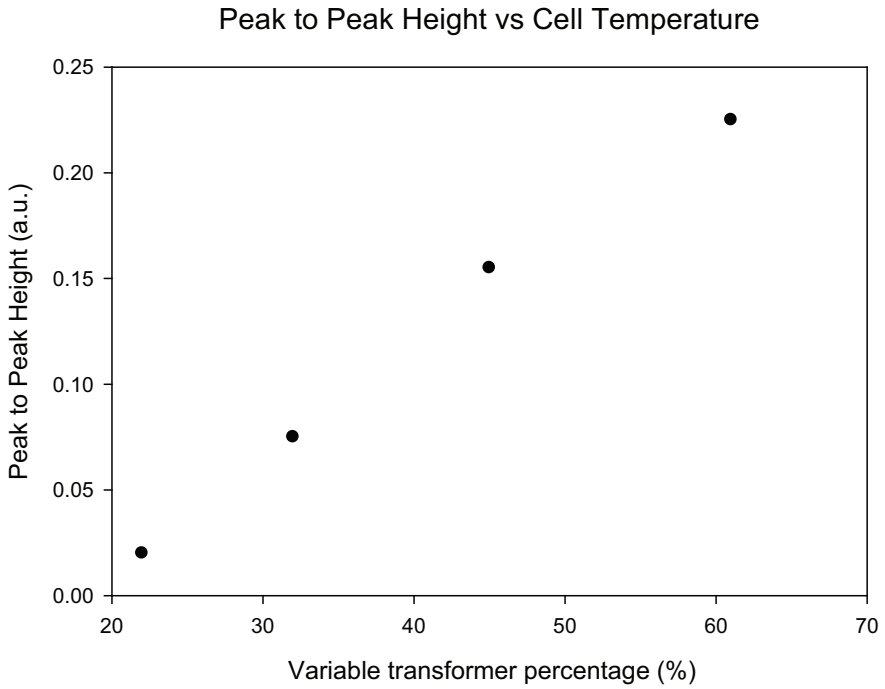

Figure 4.9: Lock signal as a function of cell temperature. The variable transformer percentage is the percentage of 120 Volts that is driving the heating element. The temperature is roughly linear with increasing transformer percentages and 0% represents room temperature, whereas 60% represents $\sim$ 600 K.

This EOM accepts radio frequencies between approximately 10 kHz and 20 GHz, and 25 mW of optical power at 739 nm can be safely sent into the EOM without photorefractive effects in the nonlinear crystal. Approximately 10 dBm of rf power is used for maximizing the power in the first order sideband, which is used for the iodine spectroscopy.

Due to coupling losses, only 10 mW of the light incident on the fiber EOM is transmitted, resulting in about 3.5 mW into the first sideband. The beam exiting the EOM is then split into three paths with a glass plate. Of the 3.5 mW to be used for spectroscopy, approximately 2.7 mW passes through the plate and then through an AOM before being focused through the iodine cell. The other two beams are a 600 μW probe beam that is overlapped with the pump beam in the cell, and a 200 μW reference beam that is used to reject intensity fluctuations of the laser. The

pump and probe beams have a mode radius of about 400 μm, and are focused with +15 cm focal length lenses through the cell to improve the signal-to-noise of the absorption signal.

The AOM has a central frequency of 200 MHz generated by a voltage-controlled oscillator and is used to frequency modulate the pump beam for lock-in detection. The 200 MHz frequency is modulated at 22 kHz with a peak-to-peak amplitude of about 3 MHz to maximize the resulting signal. The 22 kHz local oscillator is also sent to a lock-in amplifier as the reference frequency. The probe and reference beams are incident on an auto-balanced photo-receiver that subtracts the two signals and sends the output to a lock-in amplifier with a 300 ms time constant. The output from the lock-in is sent through a low-pass filter and then to a servo controller used to stabilize the cavity length.

With the cavity length stabilized to the atomic reference line in iodine, the 935 nm laser is also stabilized against long term drifts by locking to this same cavity, therefore locking to the stable iodine reference. This is accomplished by first tuning the 935 nm laser to the desired wavelength and then sending a small fraction of the beam onto the cavity to generate a side-of-fringe lock signal. As the locked cavity length is not likely to be an integer multiple of the desired 935 nm wavelength, an additional fiber-based EOM is used to generate a sideband of 935 nm light resonant with the stabilized cavity. The transmission of the cavity is sent onto a grating and the 935 nm power is measured with a photodiode for the side-of-fringe lock.

4.2.3 Measuring the Hyperfine Structure of Iodine Doppler free iodine absorption lines are located at a detuning of approximately 13 GHz, 9 GHz, and -6 GHz from the target wavelength of 739.526 nm (twice the wavelength of the $^2S_{1/2} \leftrightarrow {}^2P_{1/2}$ transition of $^{171}Yb^+$). Because the fiber EOM used to generate the sideband for spectroscopy

allows continuous tuning, we can do spectroscopy to measure the hyperfine structure of the iodine absorption lines by stabilizing the laser to the fluorescence of a trapped ion with a side-of-fringe lock. This experiment was done with $^{174}Yb^{+}$ ion because of its simpler energy level structure. The 739 nm laser was tuned just red of resonance (10 MHz relative to the 369.5 nm wavelength), and the offset on the servo was adjusted such that the count rate on the single photon counting camera remained fixed. Small fluctuations in the frequency of the 935 nm laser had little effect on the amount of ion fluorescence because the $^2D_{3/2} \leftrightarrow {}^3D[3/2]_{1/2}$ transition was strongly saturated.

With the 739 nm laser locked to a trapped ion, the microwave frequency applied to the fiber EOM was varied in 500 kHz steps over the areas of interest, and the output of the lock-in amplifier was recorded. Because of the weak nature of the lines being investigated, each point was integrated for about 1.5 seconds. We mapped out the structure of the three nearby absorption lines in order to locate the strongest line for locking. Figure 4.10 shows the hyperfine structure of the line near a detuning of 9 GHz (I_2 line #846325163b [112]), where the doublet lines at approximately 8890 MHz generate the strongest signal. For cooling $^{171}Yb^{+}$ we lock to one of the corresponding doublet lines in the 13 GHz feature at 13.141 GHz (keeping in mind the +200 MHz in the iodine lock setup and the +200 MHz AOM used for turning on and off the 369.5 nm cooling beam, shown in Figures 4.7 and 4.12 respectively).

4.2.4 Ytterbium as a qubit An energy level diagram for the $^{171}Yb^{+}$ qubit and the relevant hyperfine splittings are shown in Figure 4.11. The $^2S_{1/2}$ $|F = 1, m_F = 0\rangle$ state is defined to be logical qubit state $|\uparrow\rangle$, and the $^2S_{1/2}$ $|F = 0, m_F = 0\rangle$ state is defined to be $|\downarrow\rangle$. Note that this is opposite from the cadmium ion because the magnetic moment of $^{171}Yb^{+}$ is $\mu_{I,Yb} > 0$, whereas the magnetic moment of $^{111}Cd^{+}$

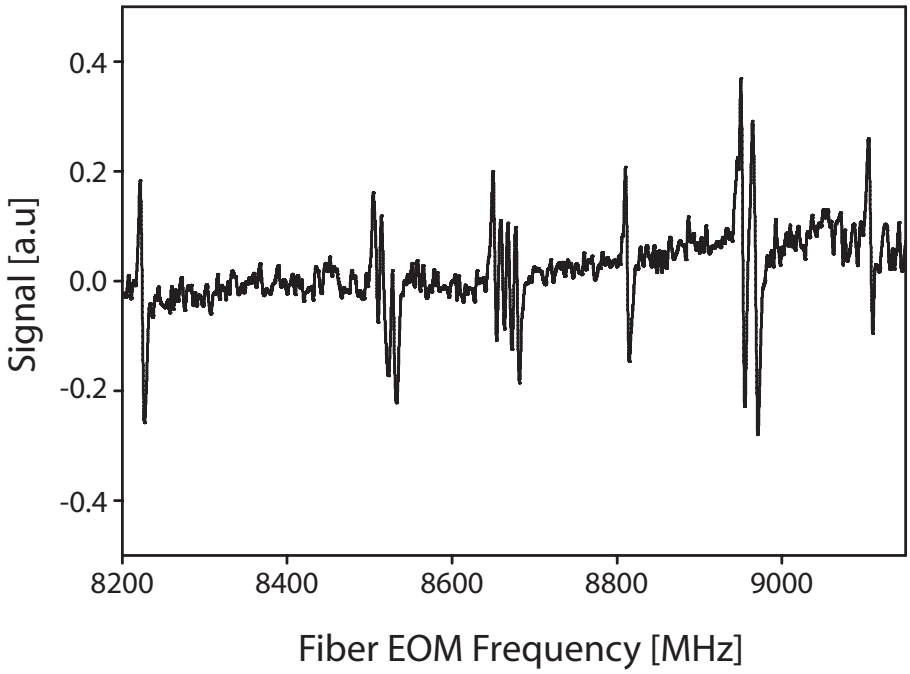

Figure 4.10: Hyperfine structure of the iodine absorption line. This displayed line is located ~ 8.6 GHz away from the ${}^2S_{1/2}$ to ${}^2P_{1/2}$ transition of ${}^{174}\mathrm{Yb}^+$.

is $\mu_{I,Cd} < 0$.

As with the cadmium ion, the qubit must first be initialized to a known state for quantum information protocols. Light resonant with the ${}^2S_{1/2}F = 1 \leftrightarrow {}^2P_{1/2}F = 1$ transition is used to initialize the ion to the $|\downarrow\rangle$ state via optical pumping (Figure 4.11). A sideband is added to the resonant 369.5 nm laser by a 2.1 GHz EOM which excites the ion from ${}^2S_{1/2}F = 1$ to ${}^2P_{1/2}F = 1$, from where it has a 1/3 chance of decaying to the $|\downarrow\rangle$ state, resulting in a 1/e time for pumping to the $|\downarrow\rangle$ state of approximately 200 ns. The 2.1 GHz EOM is only turned on for state initialization (Figure 4.12).

When excited to the ${}^2P_{1/2}F = 1$ manifold (either off-resonantly or while being pumped to the $|\downarrow\rangle$ state), the ion has a chance to decay to the ${}^2D_{3/2}F = 2$ manifold. As mentioned before, a 3.06 GHz EOM sideband on the 935 nm laser pumps out of this state. In addition to its importance for maintaining cooling, this sideband

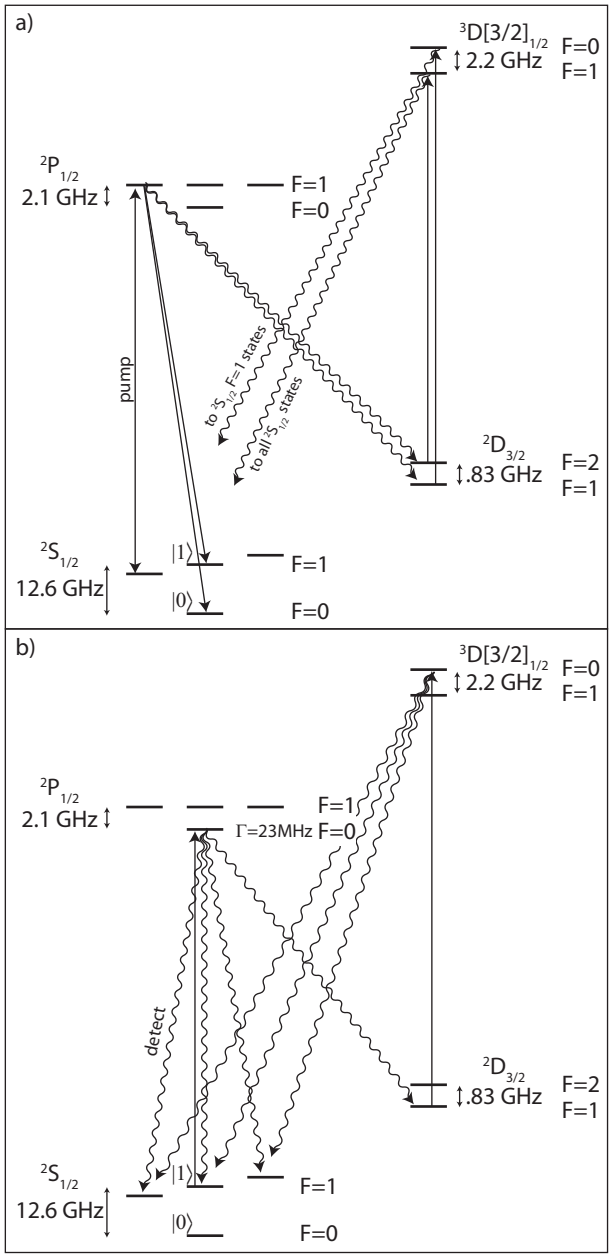

Figure 4.11: The $^{171}\mathrm{Yb}^+$ qubit. The $^2S_{1/2}$ $|F=1, m_F=0\rangle$ state is defined to be $|\uparrow\rangle$ or "bright", and the $^2S_{1/2}$ $|F=0, m_F=0\rangle$ state is defined to be $|\downarrow\rangle$ or "dark". The hyperfine splitting of the $^2P_{1/2}$ level is 2.1 GHz and the splitting of the $^2S_{1/2}$ level is 12.6 GHz. The linewidth of the $^2P_{1/2}$ $|F=0, m_F=0\rangle$ state is 23 MHz. (a) Initialization to $|\downarrow\rangle$. (b) Detection of the qubit state. If the qubit state is $|\uparrow\rangle$ it is resonant with the detection beam and scatters many photons. Note that even with the branching ratio to the $^2D_{3/2}$ state, the detection beams still create a closed transition, separate from the $|\downarrow\rangle$ state. If the state is $|\downarrow\rangle$ it sees no resonant light and scatters no photons.

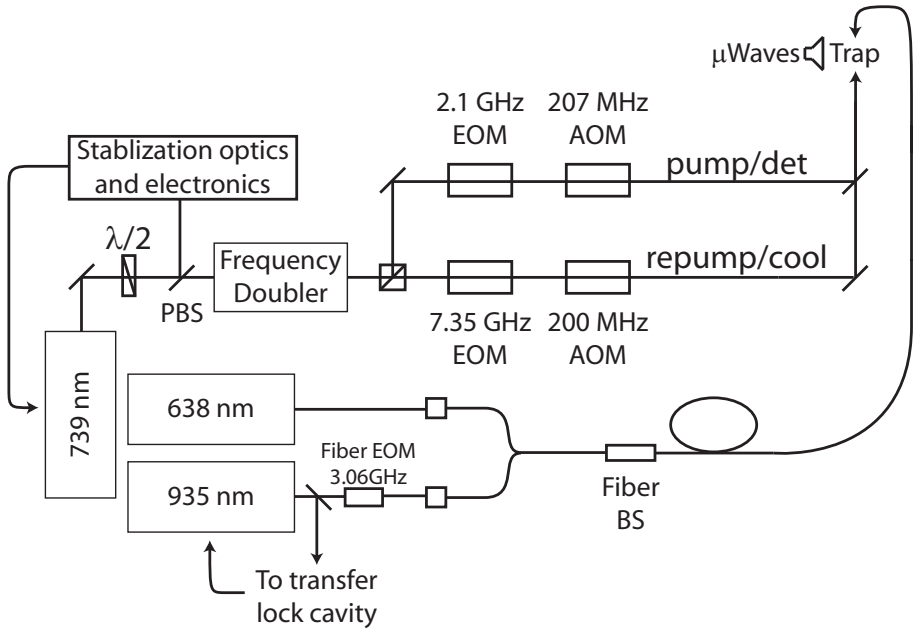

Figure 4.12: Experimental setup for initialization, manipulation, and detection of the ytterbium qubit. The EOMs are tuned to the hyperfine splittings of the S and P states, and the AOMs serve as fast acting switches for turning the beams on and off. The repump/cool beam is tuned such that the beam is about half a linewidth away from resonance to give the most efficient cooling. The pump/detect beam is tuned 7 MHz closer to resonance than the repump/cool beam in order to generate more scattering events and reduce the amount of time needed to detect.

is also necessary for fast and efficient state initialization to $|\downarrow\rangle$ because of the long lifetime of this metastable state.

Once prepared in the $|\downarrow\rangle$ state, the ion can be rotated between $|\downarrow\rangle$ and $|\uparrow\rangle$ via microwaves resonant with the hyperfine splitting (12.6 GHz), where the different Zeeman levels are resolved with an applied magnetic field. Rotations between $|\uparrow\rangle$ and $|\downarrow\rangle$ are shown in Figure 4.13. This plot also demonstrates the high detection efficiency of the $^{171}\mathrm{Yb}^{+}$ qubit, shown here to be $\approx 98.5\%$.

For detection, a beam resonant with the $^2S_{1/2}F = 1$ to $^2P_{1/2}F = 0$ transition is sent onto the ion and the number of scattered photons on a PMT is recorded. The $|\uparrow\rangle$ state is resonant with the applied light and scatters many photons, whereas the $|\downarrow\rangle$ state of the ion is off resonance by 14.7 GHz and will scatter very few photons. If the number of detected photons during the measurement interval is greater than

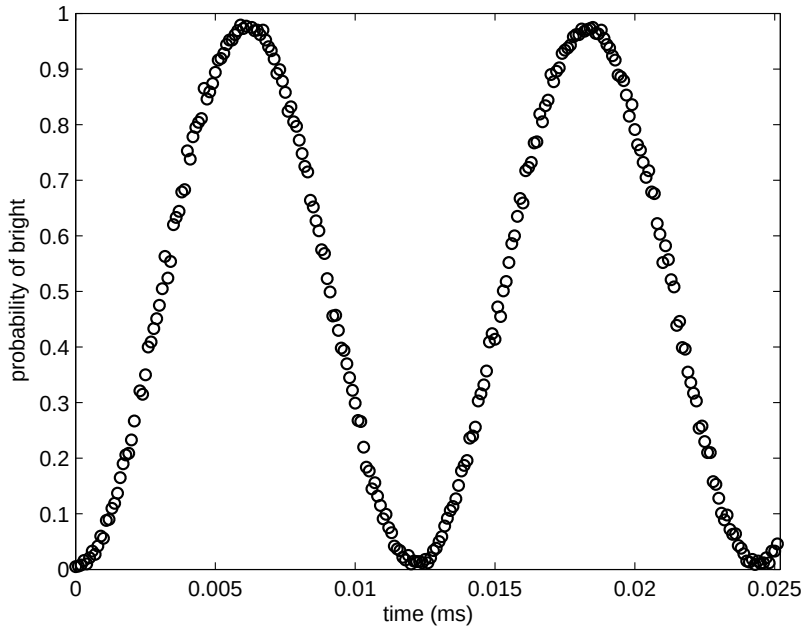

Figure 4.13: Rabi flopping of the $^{171}Yb^{+}$ qubit. This graph shows the Rabi flopping between the $|\downarrow\rangle$ and $|\uparrow\rangle$ states where the probability of $|\uparrow\rangle$ is measured as a function of the microwave pulse time. The π time of the microwaves is ≈ 6 μs at a frequency of ≈ 12.642 GHz.

the set discriminator value, then the ion is measured in the $|\uparrow\rangle$ state, whereas if the number of detected photons is less than the discriminator, then the ion is in the $|\downarrow\rangle$ state.

Errors in detection result from off-resonant coupling between the bright and dark states. A detailed study of the theoretical detection fidelity limit for different ion species was done by Acton *et. al.* in reference [113]. For a detection efficiency $p = 10^{-3}$ (one out of every 1000 emitted photons is observed) and saturation parameter of 0.25 for the detection beam, the fidelity of the measurement can be at most 99.5% for the $^{171}Yb^{+}$ qubit[5]. Most of the error occurs in off-resonantly exciting to the $^2P_{1/2}F = 1$ manifold (which can decay to the dark state) when in the bright state because of the 2.1 GHz $^2P_{1/2}$ state hyperfine splitting.

[5]A small correction to the calculation in reference [113] involves the inclusion of the $^2D_{3/2}$ state, which reduces the brightness of the ion because photons emitted when the ion decays from $^3D[3/2]_{1/2} \rightarrow {}^2S_{1/2}$ are not detected. Additionally, off-resonant pumping by the 935 nm light can occur. We estimate that given a transition probability of .005 to the $^2D_{3/2}$ states, these additions to the calculation constitute about a 1% change in the amount of error.

4.3 The Ion Trap

In order to trap ions for periods of time sufficiently long for experiments on quantum information, the ions must be trapped in ultra high vacuum (UHV) chambers. Experimentally, this requires pressures on the order of 10^{-11} Torr to limit reduce the collision rate with background gases. With these pressures maintained in our chambers, background collisions occur at an estimated rate of once per minute, but with experimental repetition rates on the the kHz timescale, these collisions are not an issue. Further, because of the depth of the ion traps used in these experiments, typical background collisions will not eject the ions from the trap, and the average lifetime of ions in our traps is on the order of days (even in the absence of laser cooling). A schematic of the vacuum chamber used in our ytterbium experiments is shown in Figure 4.14.

There are two different geometry ion traps used in the experiments described in this thesis (Figure 4.15). The first of these is an asymmetric ring-and-fork trap of characteristic size $\sim$ 700 μm [115]. This trap was used in the early experiments with cadmium because of its simple geometry and construction, and its usefulness for trapping single ions (Figure 4.16). However, because of the electrode geometry, multiply trapped ions will align in the plane of the ring (along the x-axis seen in Figure 4.15(a)). Since the rf null is located only in the middle of the circular ring, two ions cannot be simultaneously located at the rf null and will thus have unwanted micromotion. Figure 4.17 shows the modes of motion of three ions in the ring-and-fork trap. When properly cooled (Figure 4.17(a)), the ions align in a linear chain, however when driven close to resonance, the ions are not efficiently cooled and can be excited to normal modes of motion in all three dimensions (Figure 4.17(b-e)).

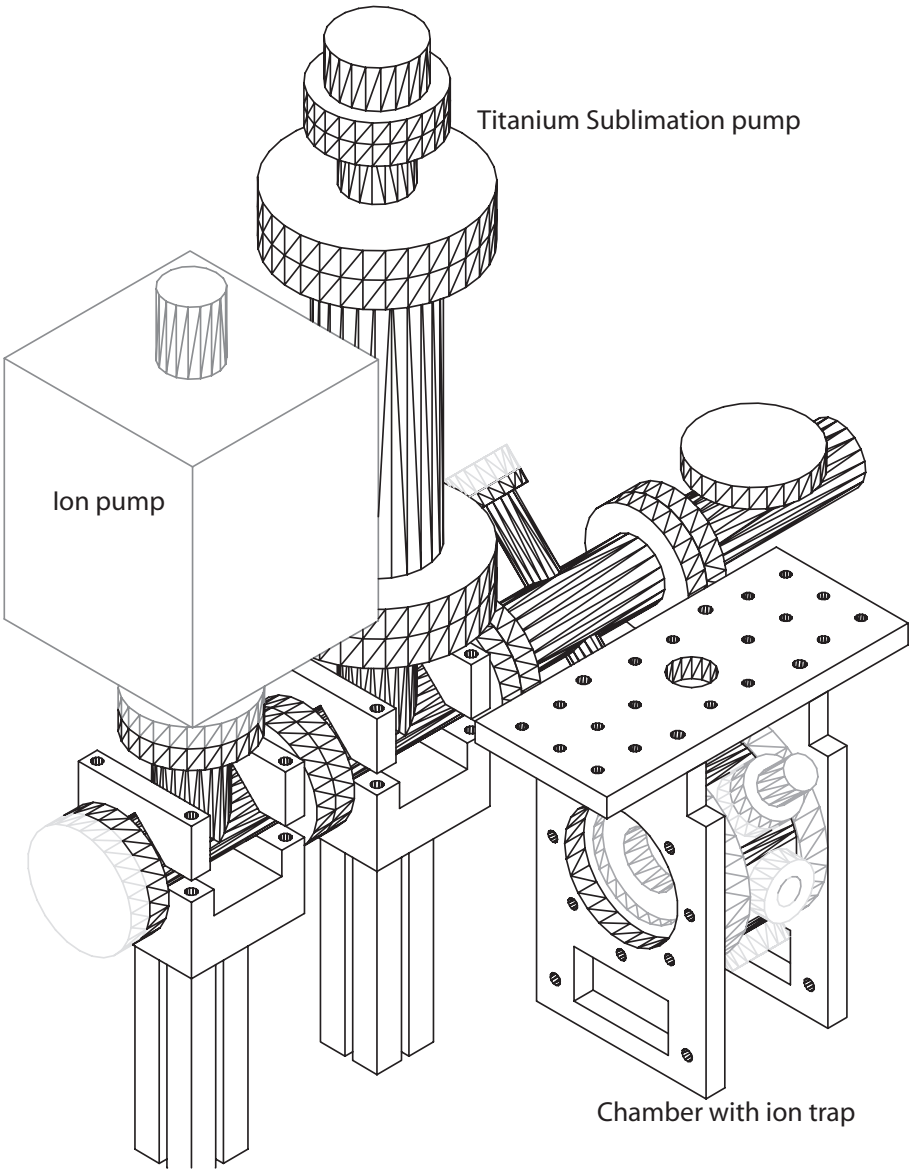

Figure 4.14: Ion trap UHV chamber. In this schematic of the vacuum chamber, the ion trap is located within the spherical octagon. Also visible in this schematic is the primary vacuum pump (a 20 Liter StarCell ion pump) used for removing background gas once the system has been pumped out. This pump can maintain an environment of below 5x10-12 Torr, as measured by a tungsten filament ionization gauge. Also visible is a titanium sublimation pump which is fired whenever the pressure in the chamber gets too high. When fired, the sublimation pump removes unwanted background gases by chemically reacting with them for easier pumping via the ion pump. Typically, the titanium sublimation pump only needs to be fired after initially sealing and baking the chamber [114].

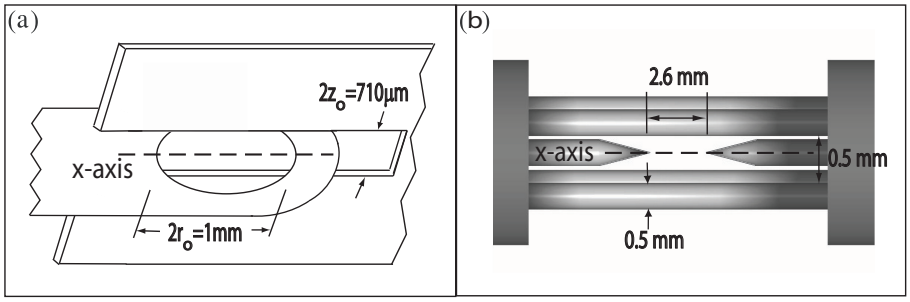

Figure 4.15: Ion traps. (a) "Ring-and-fork" trap used for early experiments in cadmium. (b) Four rod "linear" trap used for later experiments in cadmium and all experiments in ytterbium.

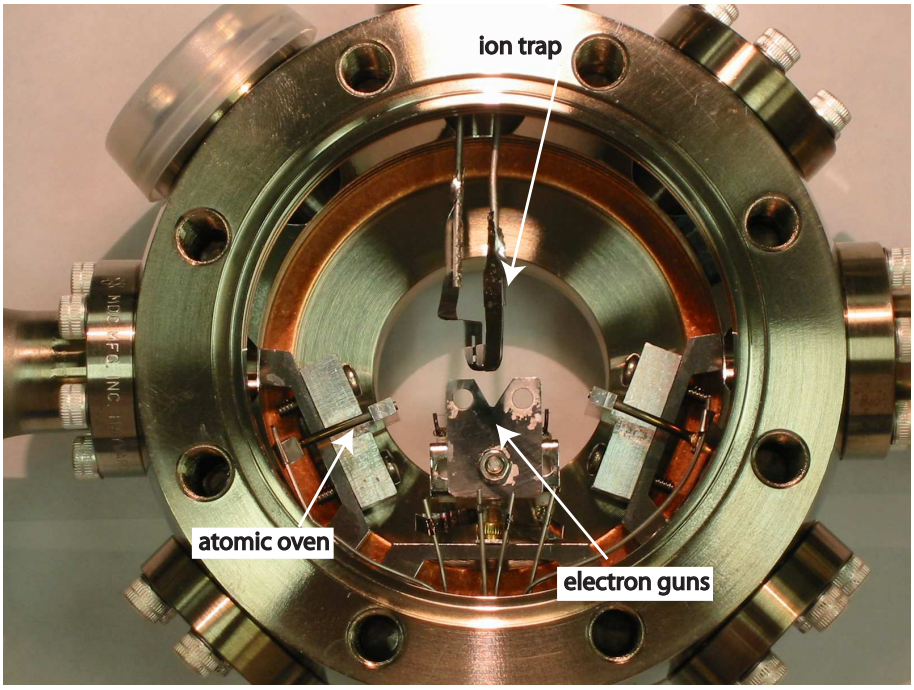

Figure 4.16: Image of the ring-and-fork trap. Also visible in this image are the atomic ovens and electron guns used to load ions within the trap.

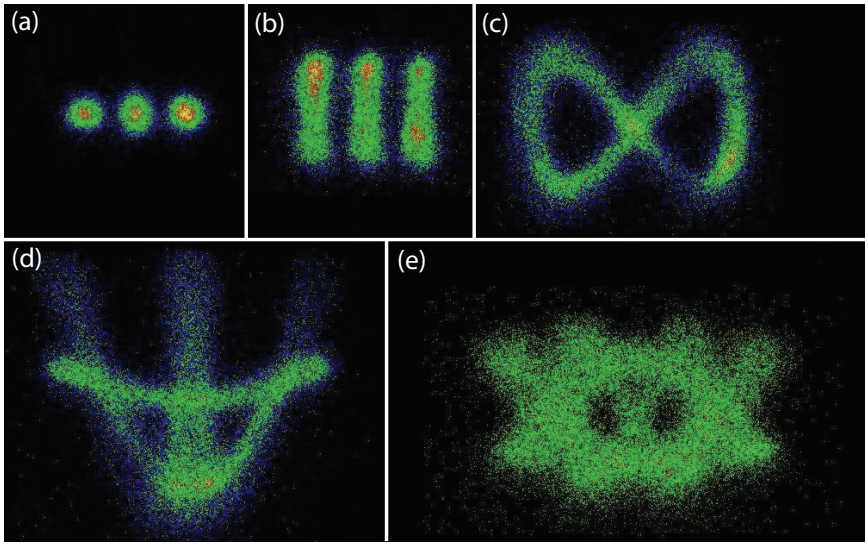

Figure 4.17: Modes of motion in the ring-and-fork ion trap. (a) Three trapped ions Doppler cooled. (b-e) Three trapped ions excited with near resonant light. When driven so near resonance, the ions are not efficiently cooled and can be excited to normal modes of motion in the trap.

For the confinement of multiple ions along an rf null, the trap must have a linear geometry. With this geometry, an rf null is created along the x-axis shown in Figure 4.15(b). Radial confinement in these traps is provided by applying rf voltage to opposing rods and rf ground to the other two rods (Figure 4.18). Axial confinement is provided by applying a small static voltage to the end-cap rods. Because of the end-cap rods, these traps are not perfectly linear, as seen by the phase shift from a linear chain of ions to a zig-zag shape chain in Figure 4.19 upon application of much higher end-cap voltages (100s of volts in our case). These four-rod linear quadrupole traps have rod spacings of 0.5 mm and end-cap spacings of 2.6 mm. The rf drive frequency is $\Omega_T/2\pi \approx 37\,\mathrm{MHz}$ and the center of mass secular trapping frequencies are $(\omega_x, \omega_y, \omega_z)/2\pi \approx (0.2, 1, 1)\,\mathrm{MHz}$. Residual micromotion at the rf drive frequency is carefully reduced by applying static offset voltages to the trap rods.

In either of these traps, the rf voltage is applied via a helical resonator is used to drive high voltages with low current [115]. Figure 4.20 shows the quarter wave

resonator used to drive this high voltage and consists of an inner helical conductor inside a conductive cylinder. In addition to carrying the high voltage rf source, the inner helical conductor can have a static offset voltage for compensation of micromotion. For driving the rf on the four rod linear trap, a similar double-helical resonator is used with two congeneric helical conductor coils wound side by side. The reason for driving the rf on opposing rods with separate helical conductors rather than a single conductor is for the minimization of micromotion — with the ability to apply independent dc voltages on all four rods, the ion can be positioned in the rf null without the need for additional offset dc electrodes.

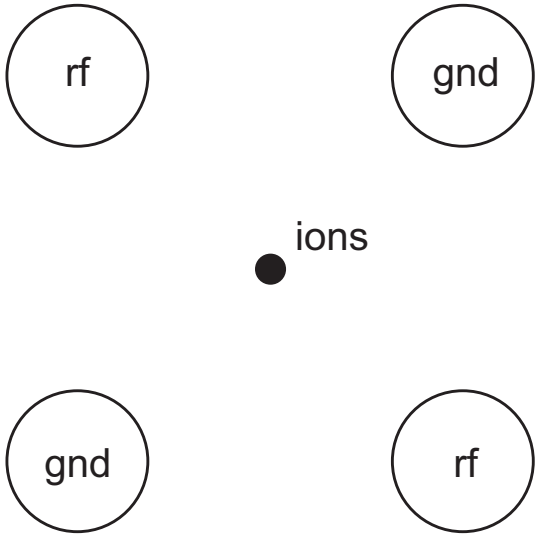

Figure 4.18: Cross-section of the four-rod linear trap. Radial confinement is provided by applying rf voltage to opposing rods and dc voltages to the other two rods. The ions are trapped along the line in the center of the four rods.

4.4 The Imaging system

Collection of the emitted photons is necessary for ion-photon entanglement as well as for further state detection of the ions. For this purpose we use one of two air spaced triplet UV objective lenses with an infinite conjugate ratio design. The first is from CVI Laser (part UVO-20.0-10.0, with the appropriate coating), and the second

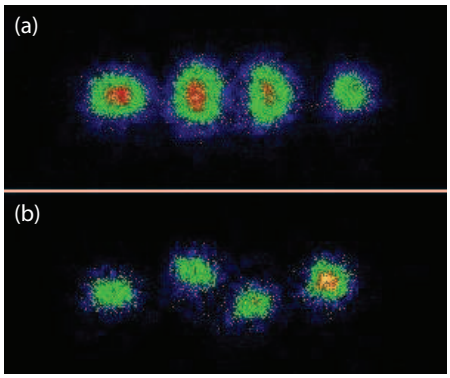

Figure 4.19: Linear ion crystal to zig-zag crystal. (a) Ions in a linear trap typically align in a linear crystal. (b) With the endcap voltages increased, the axial secular frequency becomes comparable to the radial secular frequencies and the crystal undergoes a phase change to a zig-zag crystal.

is from Special Optics (part 54-17-29-370nm). These lenses were chosen for their off-the-shelf availability, relatively low cost, high numerical aperture, and sufficiently long working distance. Specifics of these lenses are listed in Tables 4.1 and 4.2.

Lens	F/#	NA	WD (mm)	CA (mm)	Wavelength	Price ($US)
CVI	F/2.1	0.23	13	10	193-248, 355-532	$2760
SO	F/1.7	0.27	19	17	248-400	$980

Table 4.1: Imaging lens triplet general information. The CVI Laser part number is UVO-20.0-10.0-193-248 for cadmium and UVO-20.0-10.0-355-532 for ytterbium. The Special Optics (SO) lens is part number 54-17-29-370nm (for ytterbium only). F/# is the F-number, NA is the numerical aperture, WD is the working distance, CA is the clear aperture, Wavelength is the anti-reflective (AR) coating range.

Lens	L1,S1	L1,T	L1,S2	Sep	L2,S1	L2,T	L2,S2	Sep	L3,S1	L3,T	L3,S2
CVI	-38.1	4.0	-11.9	0.5	33.7	4.0	20.5	0.53	35.3	6.0	-25.8
SO	-212.6	3.0	82.9	1.8	-144.4	4.0	-18.7	0.2	181.8	4.8	-30.7

Table 4.2: Imaging lens triplet specifications. Li,Sj corresponds to lens i and surface j where the three lenses each have two surfaces. Li,T is the thickness of lens i and Sep is the separation between the lenses.

To utilize these lenses in our setup we first modeled them using OSLO optical design software. The results of this modeling optimization can be seen in Figure 4.23, where the relative irradiance of the point spread function in the image plane (IMS) is optimized by adjusting the distance between the triplet lens and the ion. In our case, the ion is located $\approx$ 8.5 mm from the surface of the vacuum window of

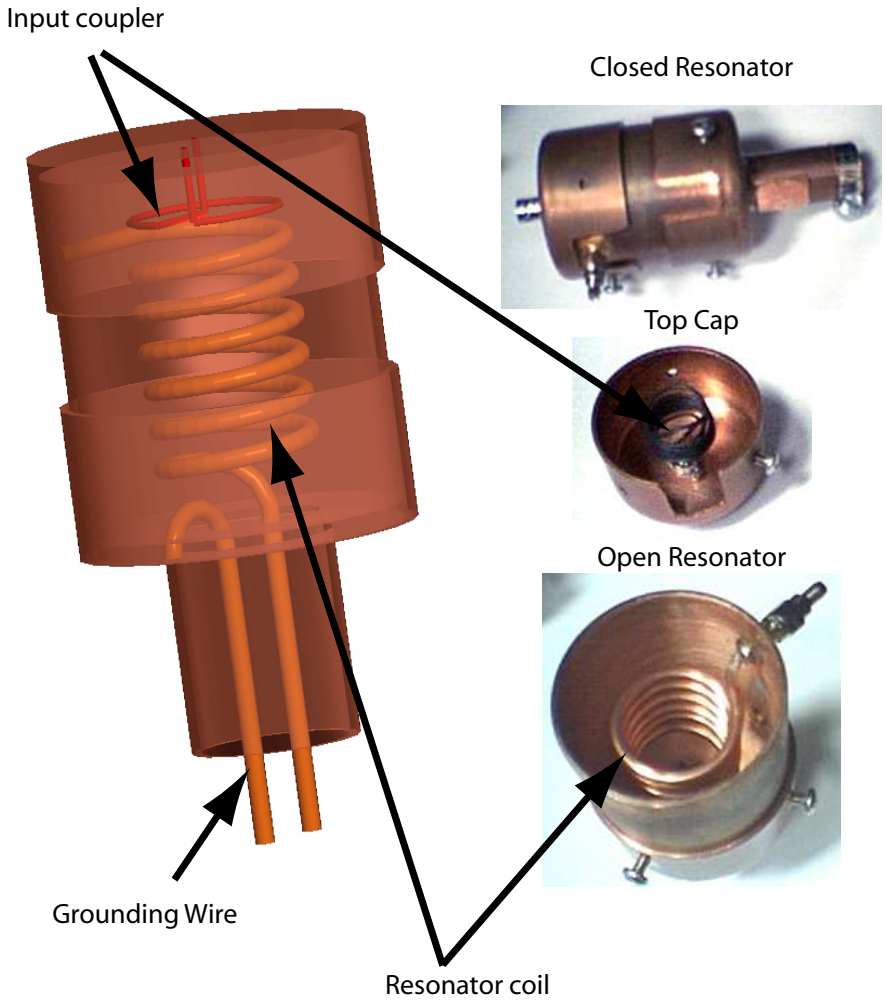

Figure 4.20: Helical resonator. A helical resonator is used to drive high voltages on the trap electrodes. This quarter wave resonator consists of an inner helical conductor inside a conductive cylinder. On the left is a schematic drawing, and on the right are photographs of the actual resonator used to drive the rf on the ring-and-fork trap. Offset voltages are applied to the grounding wire and the rf coil for compensation of micromotion. (Figure reproduced with permission from M. J. Madsen [114].)

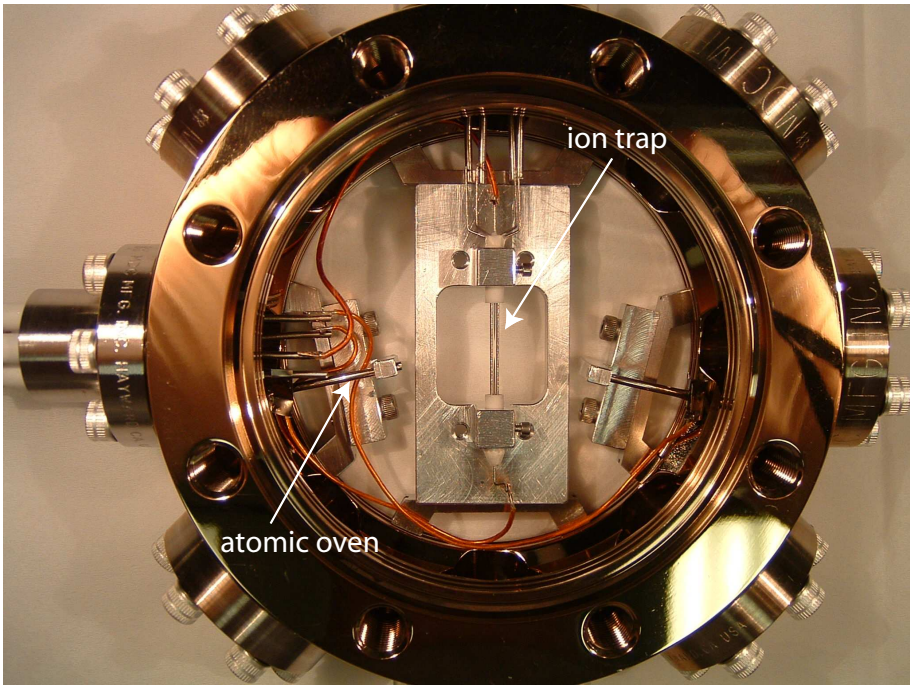

Figure 4.21: Image of the linear trap. This particular setup was for the cadmium system. One significant change for the ytterbium system is the alignment of the atomic ovens to be approximately 90 degrees to a beam axis for isotopically selective loading.

thickness 3.3 mm. The distance of the lens from this vacuum window ("thickness" of "air" between the window and the first lens) was adjusted to maximize the relative irradiance of the point spread function and find the distance to the image plane. Figure 4.23 shows the optimization corresponding to a separation of 3.47 mm between the vacuum window and the first lens, resulting in the image plane 285.4 mm after the last lens. To reduce the presence of unwanted scattered photons (off electrode surfaces, or even room lights), a pinhole of ≈ 500 μm was placed at this image plane. This intermediate image is then reimaged onto a camera or a single photon sensitive photomultiplier tube (PMT) using a doublet lens (two plano-convex lenses each of focal length ~ 75 mm depending on the desired magnification). The camera used in our system is a Quantar Technology 2401B Position Analyzer which is sensitive to positions in and x-y plane with 1024×1024 spatial digitization over a one inch active area with a quantum efficiency of $\sim 5\%$ between 214 nm and 369 nm. The

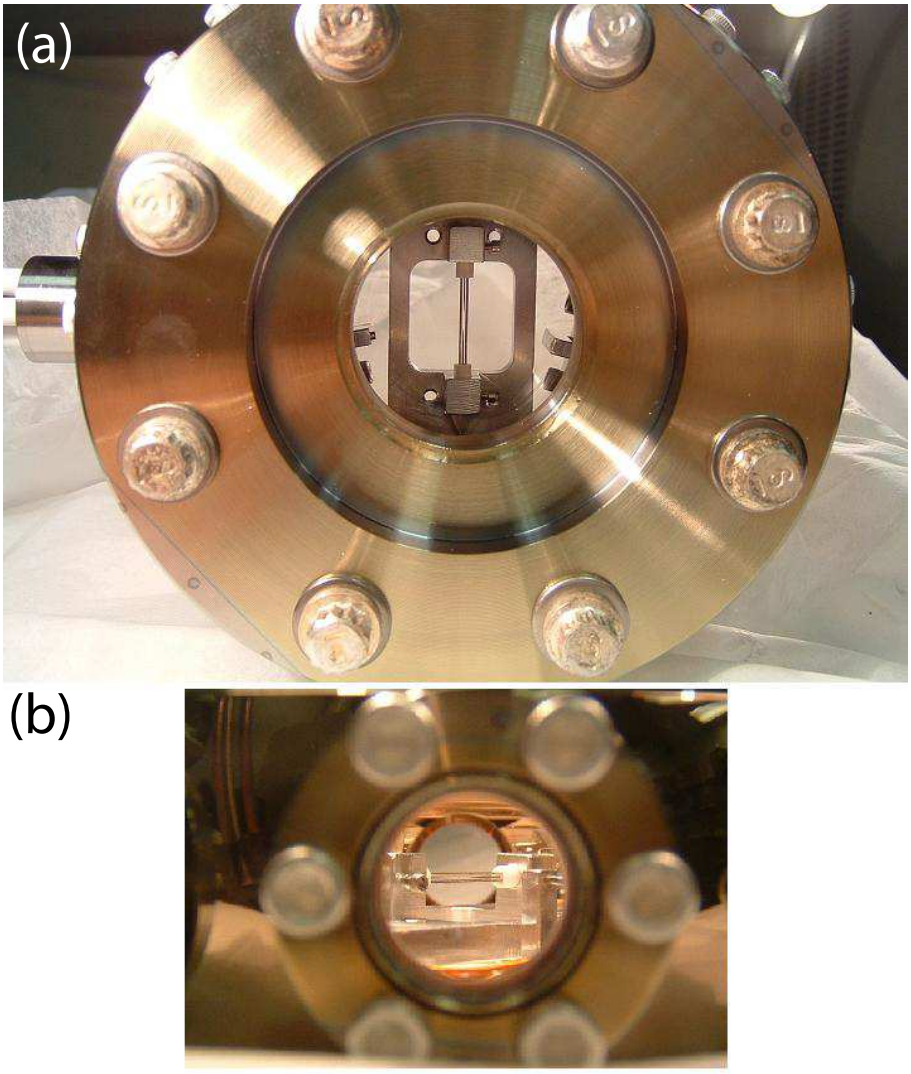

Figure 4.22: Image of the linear trap with reentrant viewports. (a) View through the reentrant viewport. This is the same view as the imaging system. (b) View through one of the smaller viewports. This is the path a laser takes through the trap.

FWHM spatial resolution is better than 60 μm. The PMTs used are Hamamatsu H8259 (H6240) Photon Counting PMTs with a quantum efficiency $\sim 15-20\%$ over this same wavelength range. Typical dark counts on these PMTs are on the order of 100/second.

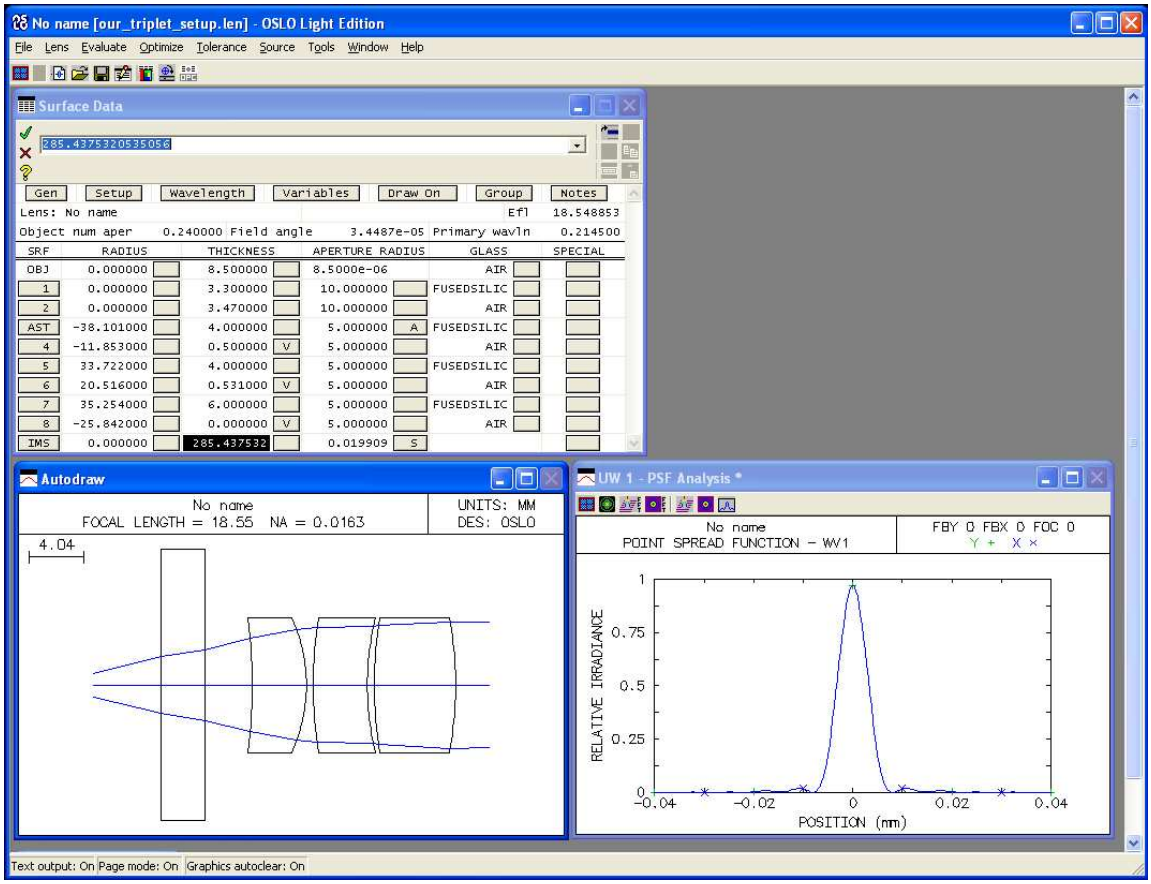

Figure 4.23: OSLO simulation of the 214.5 nm imaging setup. As seen in this screenshot from OSLO, the optimal distance for the lens from the chamber window is 3.47 mm, resulting in an image distance of $\approx$ 285.4 mm (highlighted). The "Surface Data" window displays the radii of curvature and thickness of each element, the "Autodraw" window displays the imaging system, and the "PSF Analysis" shows a scan of the point spread function of the image of the ion.

In cadmium, in addition to imaging the 214.5 nm radiation, we were also interested in imaging light from the $^2S_{1/2} \leftrightarrow {}^2P_{1/2}$ transition at 226.5 nm. As can be seen in Figure 4.24, because of the chromatic aberration in the imaging system, light at 226.5 nm is not focused to the same intermediate image plane. In order to image

light at 226.5 nm, the imaging lenses needed to be moved further away from the ion by $\approx$ 0.37 mm (Figure 4.25). This allowed us to selectively image radiation at different wavelengths, and was further used to image yet another transition at 231.35 nm as described in Appendix B. The results from OSLO were very good simulations of how far to move the triplet lens to image different wavelengths.

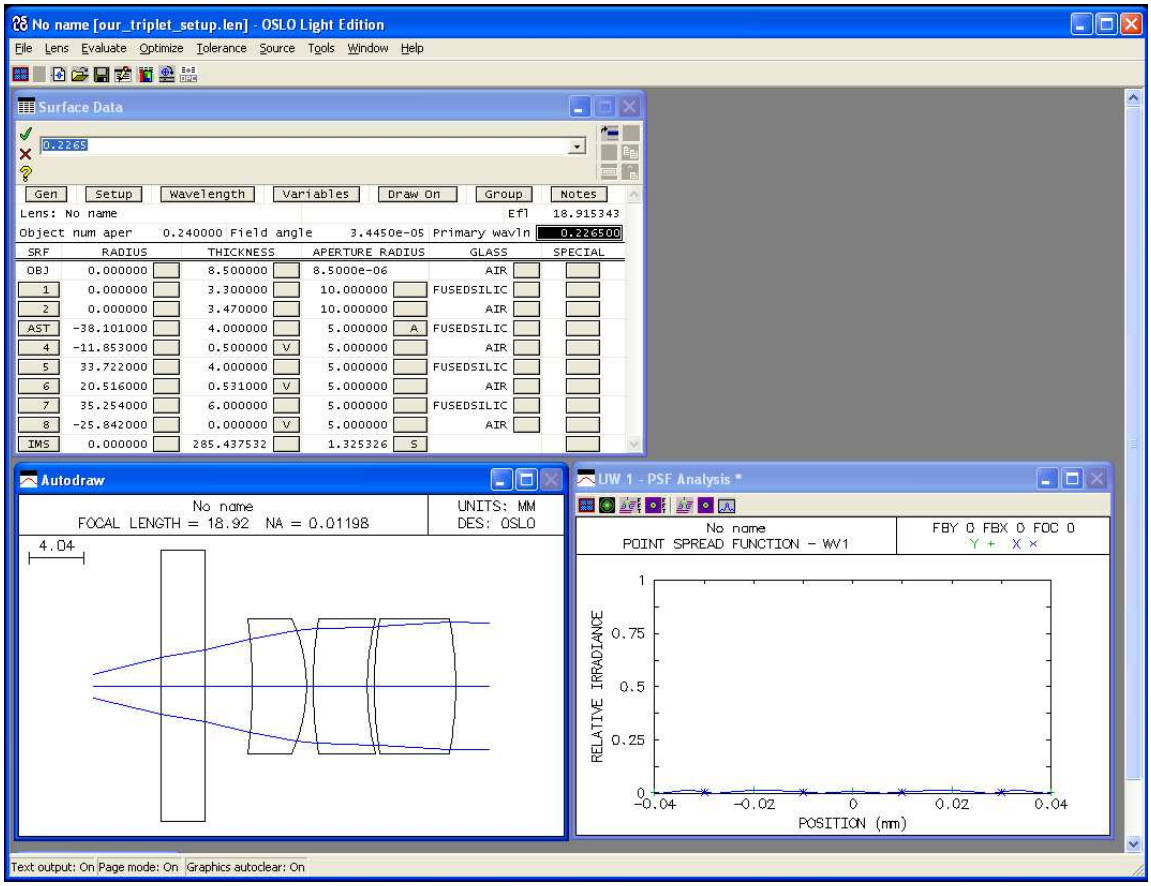

Figure 4.24: OSLO simulation of 226.5 nm light collection at the 214.5 nm setup. Because of chromatic aberration in the imaging lens, the 226.5 nm light does not have the same focal plane.

The setup used for imaging the emitted photons on the camera and the PMTs for state detection in the ytterbium system is shown in Figure 4.26. However, as mentioned before, the relatively long wavelength of the $^2S_{1/2} \leftrightarrow {}^2P_{1/2}$ transition in ytterbium at 369.5 nm also allows use of single-mode fibers. Optimization of coupling into a single-mode fiber was also simulated using OSLO. As shown in Figure 4.27, we

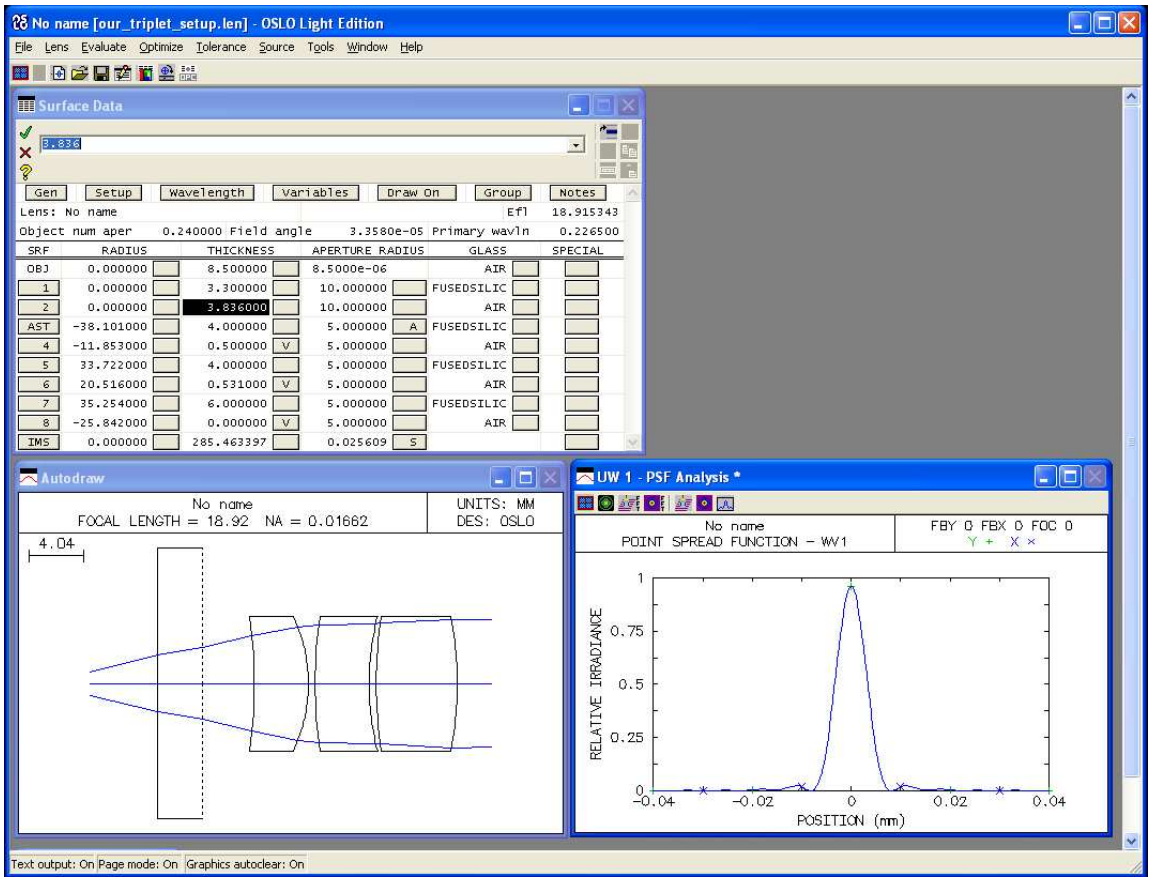

Figure 4.25: OSLO simulation for the lens readjustment for collection of 226.5 nm light. By moving the imaging lens away from the ion by ≈ 370 μm (see highlighted selection and compare to Figure 4.23), the image plane is again 285.4 mm with a similar PSF as compared to that of 214.5 nm.

used a CVI Laser triplet lens to collect the emitted photons and an aspheric lens to couple the collected light into the fiber. The overlap of our ion image from the CVI lens with the input mode of the fiber was approximately 76%. After accounting for transmission losses and reflective losses because the faces of the fibers were not AR coated, this fiber coupling troughput decreases to 55%. Experimentally, we achieved a maximum coupling of between 25-30%, estimated by comparing the count rate on a PMT after the fiber compared to the count rate on a free-space PMT. This number is somewhat lower than the potential 55%, but not too disappointing considering the non-ideal spatial mode characteristics of these triplet lenses (see Section 7.3).

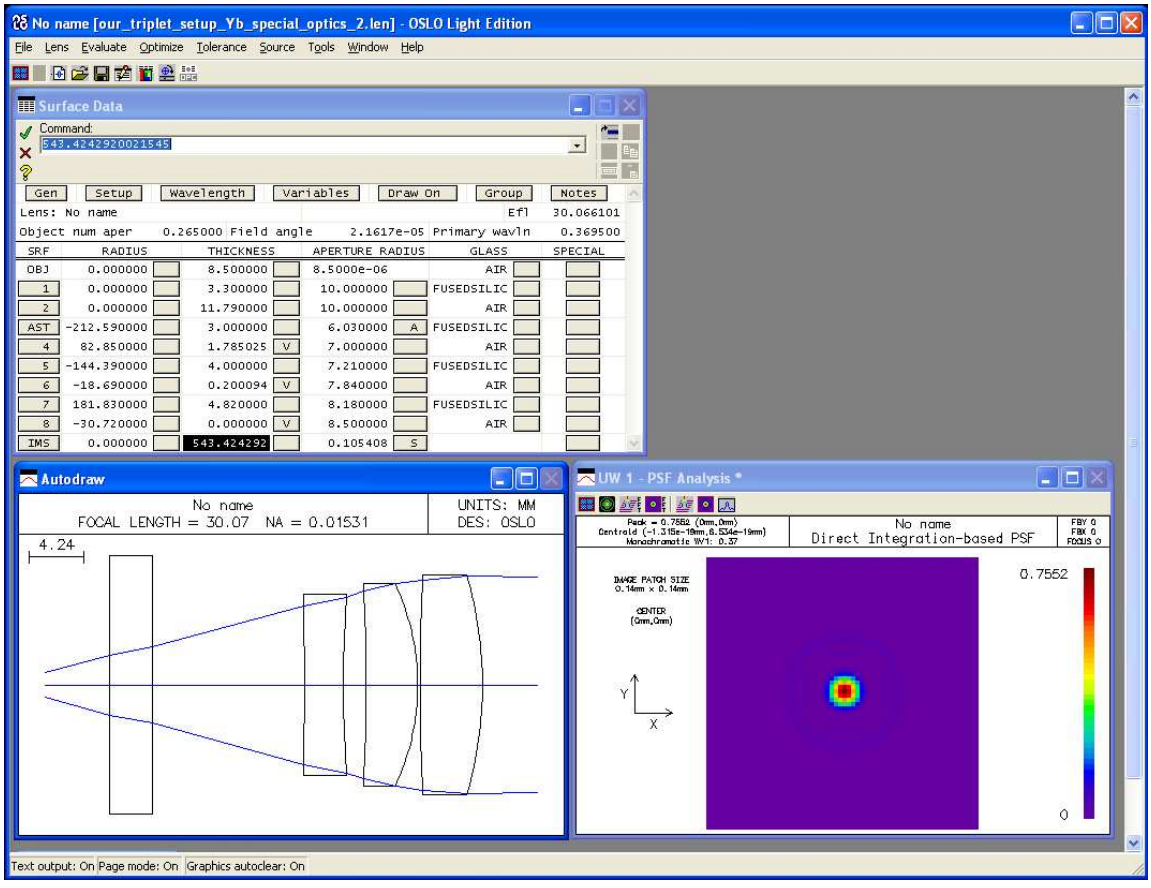

Figure 4.26: OSLO simulation of the 369.5 nm free-space imaging setup. The imaging system for the ytterbium ion is similar to that of cadmium, but with a different triplet imaging lens.

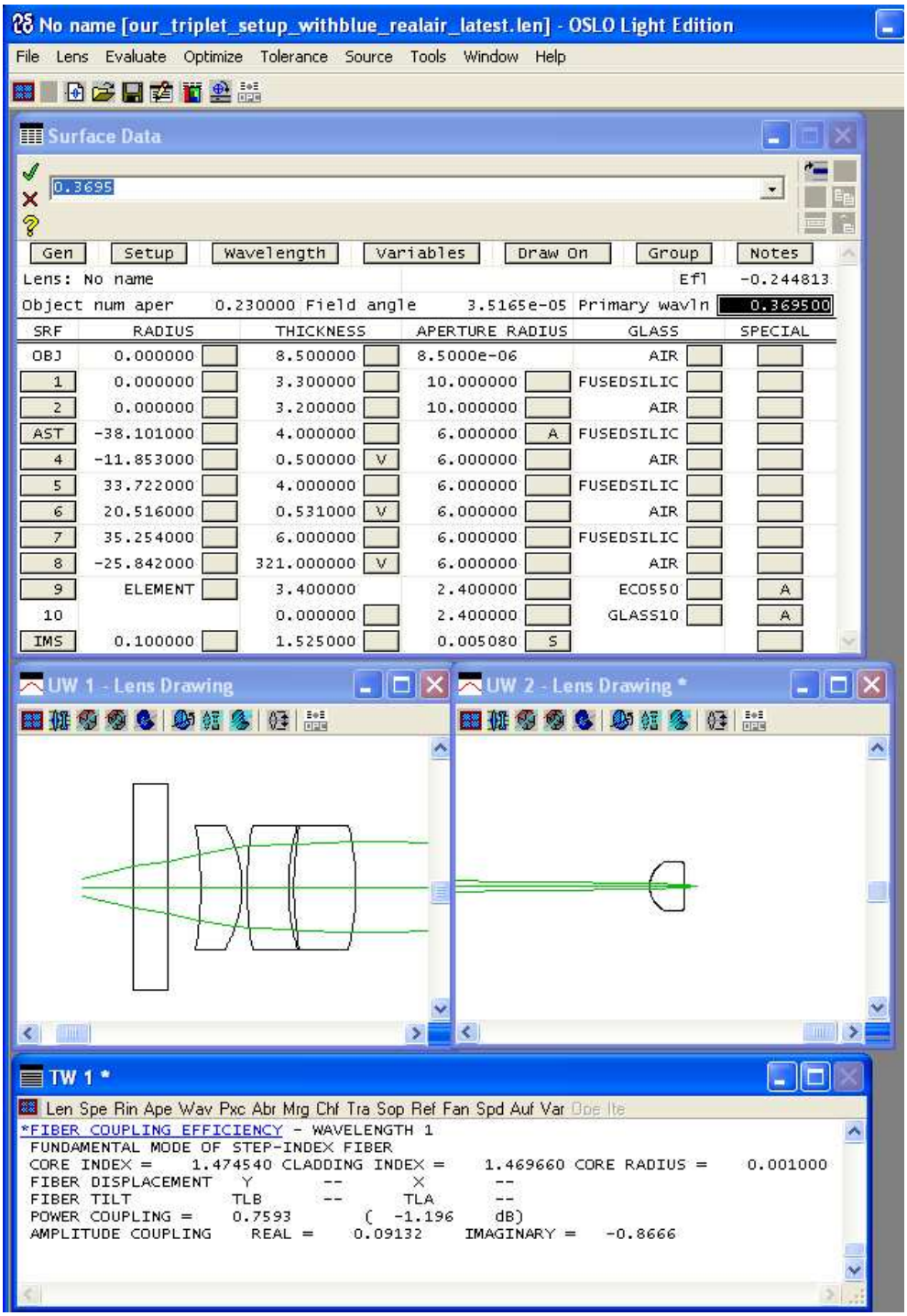

Figure 4.27: OSLO simulation of the 369.5 nm fiber-coupling imaging setup. The fiber coupling estimation from OSLO shows that if everything is aligned perfectly, we may expect an $\approx 76\%$ mode overlap with the collected mode of our ion and the input mode of the fiber. As will be discussed in more detail in Section 7.3, the imaging system is certainly not perfect. Our maximum fiber coupling efficiency through the fiber is estimated to be between 25-30% by comparing the count rate on the PMT after the fiber to the free-space PMT.

CHAPTER V

Experiments with Ions and Photon Polarization Qubits

As mentioned in the introduction, the first system with sufficient control for direct measurement of entanglement between matter and light was our trapped cadmium ion system [116, 15]. While matter-light entanglement had been implicit in many experimental systems leading up to our experiments [117, 118, 119, 5, 6, 75, 120, 121, 122, 123, 124, 116, 15, 125, 126, 18], ours was the first to explicitly measure non-classical correlations of the states between an atom and a photon. In our experiments, a photon is spontaneously emitted from a single trapped atomic $^{111}Cd^{+}$ ion, which is initially excited to a state with two decay channels. Along a certain emission direction selected by an aperture, the photon's polarization is entangled with particular hyperfine ground states in the de-excited atom [Figure 2.1(b)]. The entanglement is directly verified through subsequent polarization analysis of the photon and state detection of the trapped ion. Given the small collection solid angle and other losses, the post-selected probability of detecting the ion-photon entangled pair $P_{\text{a-p}}$ in a given trial (which relies on the detection of the emitted photon) is small. This is reminiscent of the production of entangled photon pairs through spontaneous optical parametric down-conversion [127], but in this system one of the two daughter qubits resides within a trapped atomic ion – perhaps the most reliable of

all qubit memories [128]. Hence, when this probabilistic entanglement generation is accompanied by conventional quantum gates between local trapped ions [22, 24, 38], it can form the basis for a scalable architecture for quantum communication [129] and computation [89]

5.1 Entanglement Generation

A diagram of the experimental setup is shown in Fig. 5.1. We trap and laser cool a single $^{111}Cd^{+}$ ion in the asymmetric-quadrupole ring-and-fork radio frequency trap described in Chapter IV. As mentioned in Chapter III, it is not necessary to laser cool the ion to the Lamb-Dicke limit. Several laser pulses tuned near the $^2S_{1/2} \leftrightarrow {}^2P_{3/2}$ atomic resonance at 214.5nm (1) initialize the internal atomic qubit state, (2) excite the atom for the subsequent spontaneous emission of a photon, and (3) detect the internal state of the atom. An applied magnetic field of $B \approx 0.7$ G provides a quantization axis for definition of the photon polarization and the internal atomic qubit levels, stored in $^2S_{1/2}$ hyperfine ground states.

Figure 5.2 shows a diagram of the relevant energy levels of the $^{111}Cd^{+}$ atomic ion, along with the step-by-step description of the experimental procedure. A short π-polarized laser pulse followed by a resonant microwave transfer pulse initializes the ion in the $|1,0\rangle$ state (Fig. 5.2a). A 50-ns pulse of σ^{+}-polarized laser light weakly excites the ion to the $^2P_{3/2}|2,1\rangle$ state[1], which has a radiative lifetime of $\tau \approx 2.65$ ns [95]. The ion then spontaneously decays to either the $^2S_{1/2}|1,1\rangle \equiv |\uparrow\rangle$ ground state while emitting a π-polarized photon, or the $^2S_{1/2}|1,0\rangle \equiv |\downarrow\rangle$ ground

[1]An alternative option for exciting to the $^2P_{3/2}|2,1\rangle$ state would be to excite from the $^2S_{1/2}$ $|1,1\rangle$ state using π-polarized excitation light. However, this was not done originally since confidence in alignment of the σ^{+}-polarized light is much better than the π-polarized light. This is because great care was taken to align the σ^{+}-polarized light for qubit state detection, which has a very strong dependence on the quality of the σ^{+} light. No such strong dependence exists for the π-polarized light. Later (unpublished) experiments were performed using this alternative method which has the advantage that the repetition rate can be much greater — you can pump to the $^2S_{1/2}$ $|1,1\rangle$ state using σ^{+}-polarized light and immediately drive the ion to the excited state without the use of a microwave pulse. While this method resulted in a slightly lower fidelity, the increase in speed would be important for remote ion entanglement where the success probability $P_{\text{a-a}}$ is small.

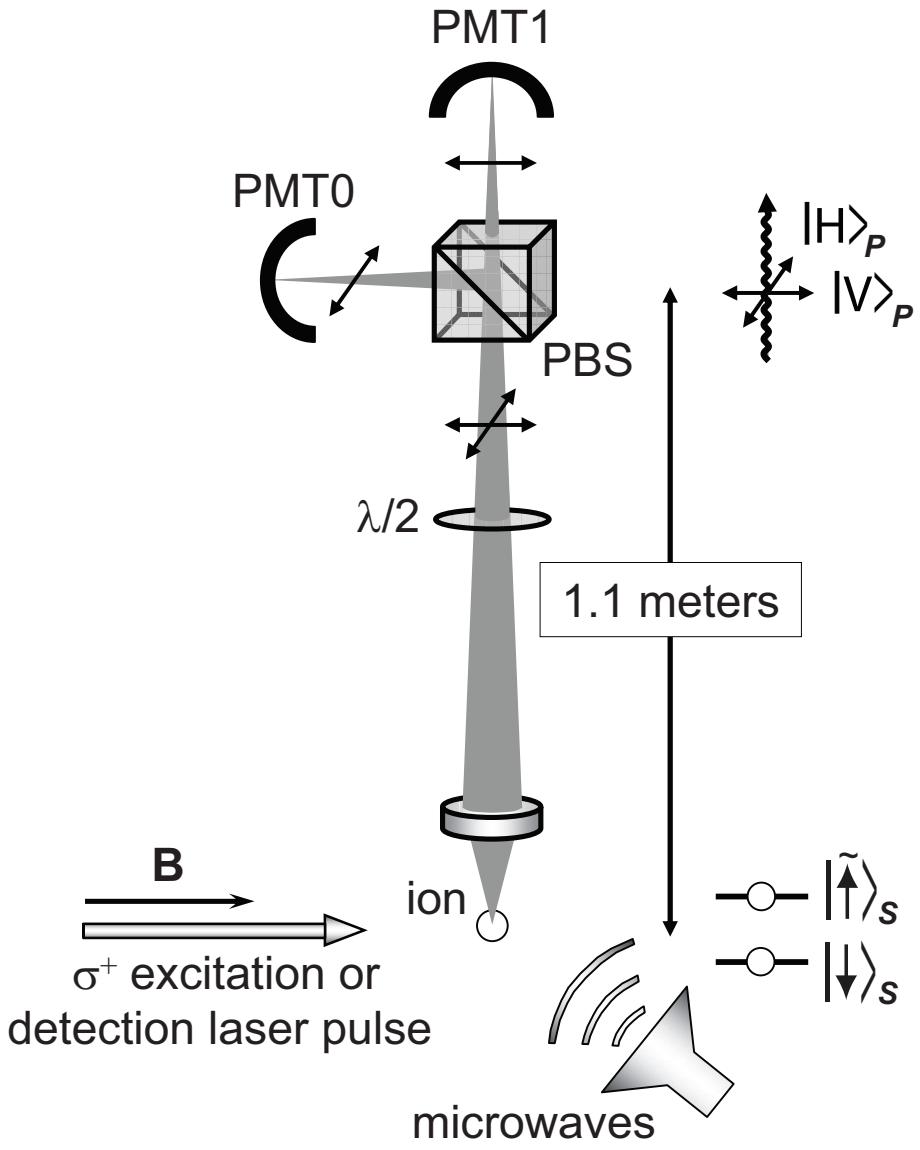

Figure 5.1: Experimental apparatus for ion-photon entanglement. Following excitation of the atom from a 50 ns laser pulse, the scattered photons are collected by an imaging lens, directed to a polarizing beam splitter (PBS), and registered by one of two photon-counting photomultiplier tubes (PMTs). A $\lambda/2$ waveplate is used to rotate the photon polarization for photonic qubit measurements in different bases, and the microwaves are similarly used on the ion to drive coherent transitions between the atomic qubit hyperfine ground states at a frequency near 14.5 GHz. Following application of the microwaves, a 125 μs laser pulse is directed on the ion for atomic fluorescence qubit state detection.

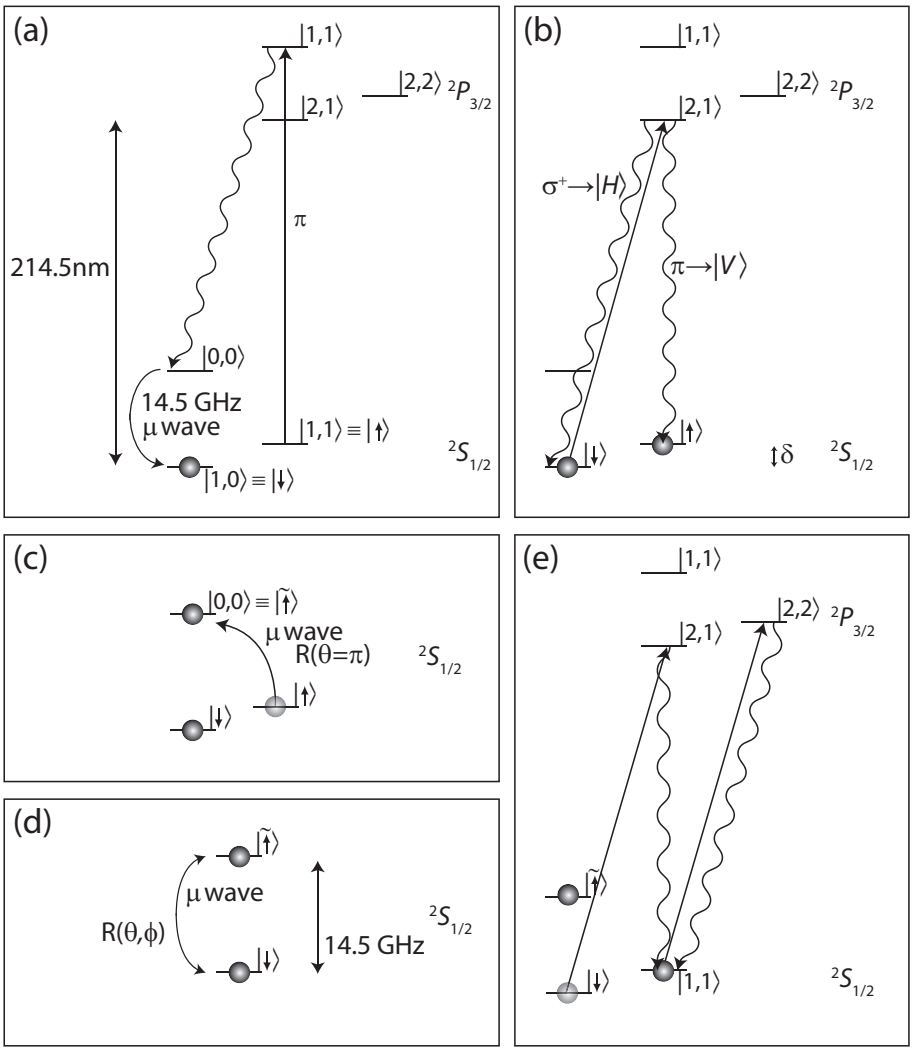

Figure 5.2: Experimental procedure for atom-photon entanglement with photon polarization qubits [116, 15]. (a) The atom is initialized to the $|1,0\rangle$ state via optical pumping to the $|0,0\rangle$ state and a microwave (μwave) transfer pulse. (b) The atom is weakly excited with a 50-ns σ^+-polarized optical pulse, resulting in spontaneous emission to either state $|\downarrow\rangle$ or state $|\uparrow\rangle$ (separated by frequency $\delta \approx 2\pi(1.0\text{ MHz})$), accompanied by emission and detection of a photon polarized in state $|H\rangle$ or state $|V\rangle$, respectively (when viewed perpendicularly to the quantization axis). The resulting entangled state is $\sqrt{1/3}\,|\downarrow\rangle\,|H\rangle + \sqrt{2/3}\,|\uparrow\rangle\,|V\rangle$. (c) A microwave pulse resonant with the $|1,1\rangle \leftrightarrow |0,0\rangle$ transition coherently transfers the population to the "clock" qubit states. (d) A second microwave pulse prepares the atomic qubit for measurement in any basis. (e) A σ^+-polarized laser pulse performs state detection of the atomic qubit using resonance fluorescence techniques.

state while emitting a σ^+-polarized photon (Fig. 5.2b). The single photon pulses are collected with the CVI triplet lens of numerical aperture 0.23 whose axis is perpendicular to the quantization axis. As described in Chapter II, the states of polarization of the σ^+ and the π photons along this direction are orthogonal: the former (defined as $|H\rangle$) is polarized perpendicular to the quantization axis, while the latter (defined as $|V\rangle$) is polarized along the quantization axis. The resulting state created upon a photon emission in this direction is $\sqrt{\frac{1}{3}}|\downarrow\rangle|H\rangle + \sqrt{\frac{2}{3}}|\uparrow\rangle|V\rangle$, which exhibits an entanglement fidelity of 0.97 under ideal conditions with respect to a maximally entangled Bell state[2]. During a successful entanglement event, the collected photon first passes through a polarization rotator (a $\lambda/2$ waveplate) and is sent to a polarizing beam splitter. The two polarization components are then directed to photon-counting photomultiplier tubes (PMTs), each of quantum efficiency $\eta \approx 20\%$. Following a single photon detection on either PMT, a microwave rotation is applied to the atom, which prepares the atomic qubit to be measured in any basis. This measurement is performed with a σ^+-polarized detection pulse following standard trapped ion fluorescence techniques (Fig. 5.2e) [130, 113], with an atomic qubit detection efficiency greater than 95%.

We first measure the conditional probabilities[3] of detecting a certain atomic qubit state given the photonic qubit state after ∼1,000 successful trials in an unrotated basis. Before atomic qubit measurement, the $|1,1\rangle \equiv |\uparrow\rangle$ state is shelved into $|0,0\rangle \equiv \left|\tilde{\uparrow}\right\rangle$ before state detection (Fig. 5.2c). The resulting probabilities are plotted in Fig. 5.3, with $P(\downarrow|H) = 0.97 \pm 0.01$, $P(\uparrow|H) = 0.03 \pm 0.01$, $P(\downarrow|V) = 0.06 \pm 0.01$ and

[2]Unit fidelity could be achieved by detecting the scattered photons along the quantization axis, with the initial atom excitation to a $|m_F = 0\rangle$ excited state, such that only σ^+- and σ^--polarized photons are collected [see Figure 2.1(c)]. We avoid this option, however, as it would require placement of PMTs in a direct line-of sight with the σ^+-polarized atomic qubit detection laser beam.

[3]Probabilities are reported conditioned on the polarization state of the detected photon because the two output ports of the PBS have different transmission and detection efficiencies. Specifically, the side port of the PMT was only approximately 70% as efficient as the through port.

$P(\uparrow|V) = 0.94 \pm 0.01$, where the errors are statistical. To verify entanglement, we repeat the correlation measurement in a different basis of both photonic and atomic qubits. The photon polarization is rotated by 45° using the $\lambda/2$ waveplate, and the atomic qubit is rotated by applying microwaves driving the $|1,0\rangle \leftrightarrow |0,0\rangle$ and the $|1,1\rangle \leftrightarrow |0,0\rangle$ transitions as indicated in Fig. 5.2(c-d) and described in detail in Appendix A.2. Both qubit rotations are through an effective Bloch polar angle of $\pi/2$, and the relative phase of the photonic and atomic qubit rotations is given by $\phi = \delta t + \phi_\mu$, where $\delta \approx 2\pi(1.0 \text{ MHz})$ is the Zeeman splitting between the $|1,0\rangle$ and the $|1,1\rangle$ levels, and $t \approx 1$ μs is the time delay between the photon emission and the application of the microwave pulse of phase ϕ. Varying the relative phase of the two qubit rotations by adjusting ϕ produces the correlation fringes shown in Fig. 5.4(a). Figure 5.4(b) shows the values of conditional probabilities at the point of maximum correlation, $\phi = 0$. These probabilities are $P(\downarrow|H) = 0.89 \pm 0.01$, $P(\uparrow|H) = 0.11 \pm 0.01$, $P(\downarrow|V) = 0.06 \pm 0.01$ and $P(\uparrow|V) = 0.94 \pm 0.01$. If the atomic and photonic qubits were not entangled but instead prepared in a statistical mixture, then all of these conditional probabilities would have been 0.5.

From these measured correlations, we calculate a bound on the entanglement fidelity to be $\mathscr{F} = 0.87$ (described in the Appendix C.1), somewhat lower than the potential 0.97 fidelity described above, but still significantly larger than the entanglement threshold of $\mathscr{F} > 0.5$ [27]. Several factors contribute to this decrease in fidelity, including: multiple excitations of the atom during the pump pulse (2.5%), mixing of the photon polarizations owing to the nonzero solid angle (0.5%), imperfect rotations of the atomic qubit, mainly due to a 50-ns jitter in the delay t (1.5%), background counts and dark counts on the PMTs leading to false positives (5-10%), and imperfections in the polarizing beam splitter (3%). We estimate that magnetic

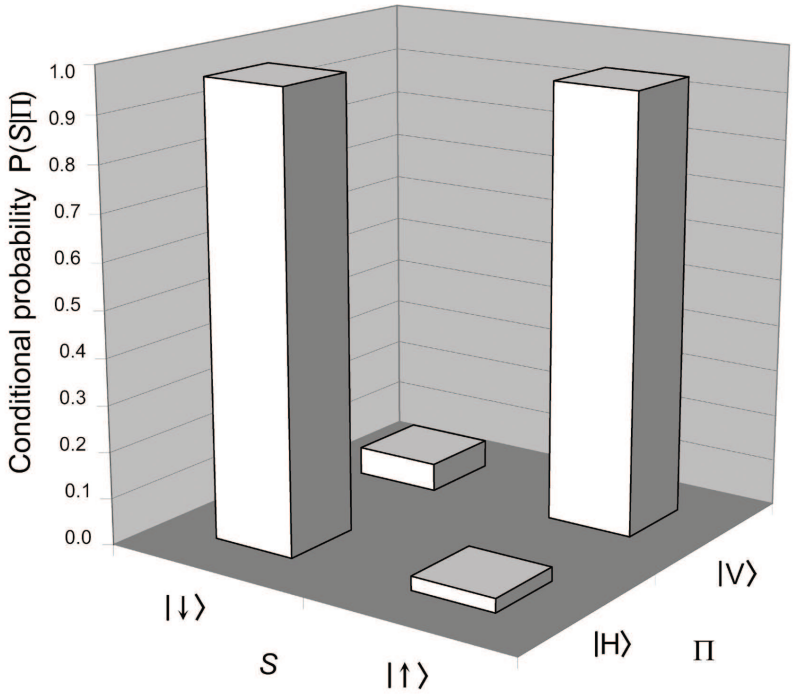

Figure 5.3: Measured conditional probabilities in the unrotated basis (no atomic or photonic qubit rotation before measurement). The bars indicate the probabilities $P(S|\Pi)$ of detecting atomic qubit states $S = |\downarrow\rangle$ or $|\uparrow\rangle$ conditioned upon detecting photon qubit states $\Pi = |H\rangle$ or $|V\rangle$

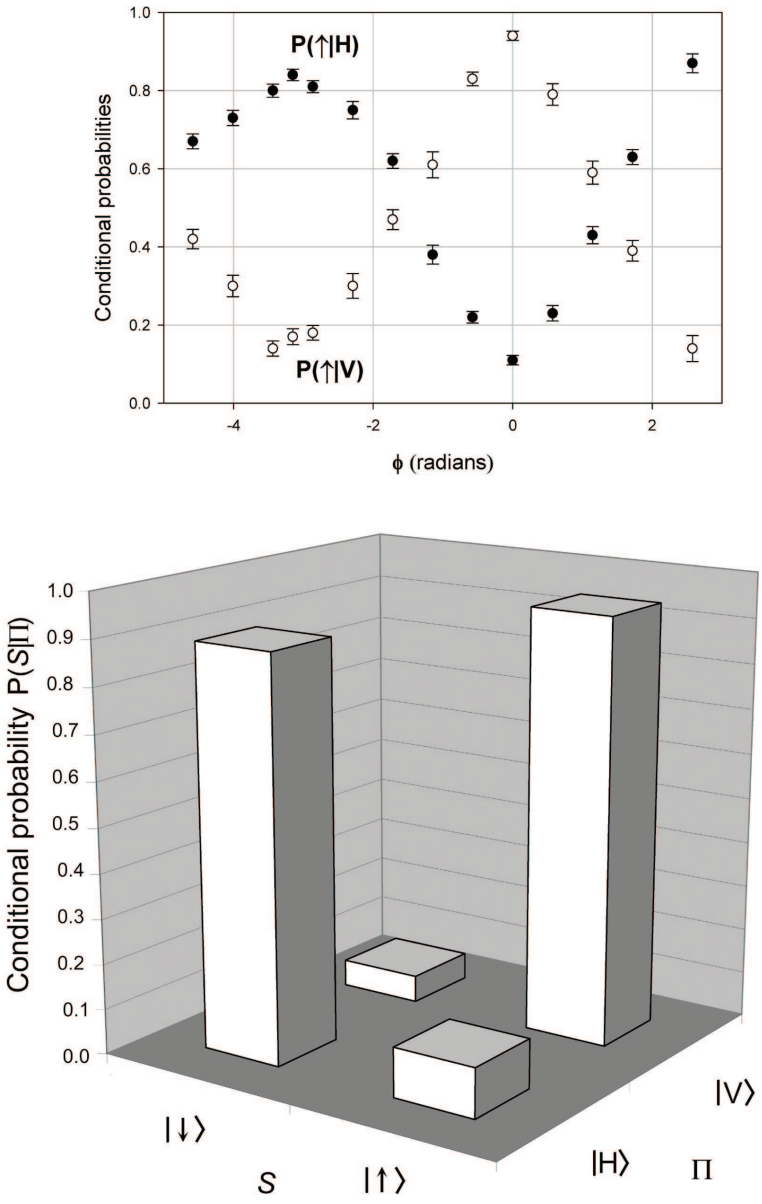

Figure 5.4: Measured conditional probabilities in the rotated basis. Conditional probabilities after both atomic and photonic qubits are rotated by a polar angle of $\pi/2$ in the Bloch sphere. (a) Measured conditional probabilities $P(\uparrow |H)$ and $P(\uparrow |V)$ as the relative phase ϕ between the atomic and photonic rotations is varied. (b) Measured conditional probabilities $P(S|\Pi)$ at the point of highest correlation, defined as $\phi = 0$. If the atomic and photonic qubits were not entangled but instead prepared in a statistically mixed state, then all conditional probabilities in the figure would have been 0.5.

field fluctuations affecting the atomic qubit reduce the fidelity by $\ll 1\%$. All sources of errors combine to give a $\sim 9\%$ reduction of entanglement fidelity, consistent with the observation.

As mentioned in Chapter II, this entanglement generation is a probabilistic process. With the cw excitation scheme, the probability of emitting a single photon in each trial is restricted to $p_e \approx 0.1$ to suppress multiple-excitations. The resulting success probability is $P_{\text{a-p}} = p_e \eta T(\Delta\Omega/4\pi) = (0.1)(0.2)(0.4)(0.02) \approx 1.6 \times 10^{-4}$. The experiment repetition rate is $R = 1/T_{\text{rep}} = 10^4 s^{-1}$, resulting in an entanglement generation rate $R_{\text{a-p}} = P_{\text{a-p}} R \approx 1.6 s^{-1}$.

Several improvements could significantly increase this yield. The repetition rate R could approach the excited-state spontaneous emission rate of $1/\tau \approx 10^8 \text{s}^-1$. Using a fast, tailored laser pulse for the excitation could push p_e toward unity, while eliminating multiple excitations. In addition, an imaging lens with a larger numerical aperture would improve the collection solid angle. A trade-off here is that higher collection efficiency comes at the cost of lower fidelity of the entangled state, which can be shown to vary as $\mathscr{F} = 0.97 - 0.24(\Delta\Omega/4\pi)$ for $\Delta\Omega \ll 4\pi$. An alternative is to surround the ion with an optical cavity [36, 66] that would allow the collection of most of the photons scattered in each experiment and effectively make $\Delta\Omega/4\pi$ approach unity without sacrificing fidelity. It is important to note that this cavity need not be in the strong-coupling regime, as it affects only the entanglement efficiency, not the fidelity.

5.2 Bell Inequality Violation

In addition to the measurement of fidelity, entanglement can be verified by measuring non-classical correlations in order to violate a Bell inequality. As discussed

in the introduction, the famous 1935 Einstein-Podolsky-Rosen thought experiment showed how measurements of certain entangled quantum systems require a nonlocal description of nature [1], thus leading to the suggestion that quantum mechanics is incomplete. However, starting in 1965, Bell and others discovered that certain measured correlations between multiple systems, averaged over many identical trials, must obey particular inequalities for *any* local (hidden-variable) theory to apply [2, 4]. Experiments showing violations of these Bell inequalities followed shortly thereafter involving entangled photon pairs [5, 6, 7, 8, 9], low-energy protons [10], neutral kaons [11], trapped atomic ions [12] and individual neutrons [14].

In this section, I report our measurement of a Bell inequality violation ion our cadmium ion system, representing the first violation of a Bell inequality in a hybrid system. While this experiment closes neither the locality [7, 9] nor detection [12] loophole, the atom-photon system has future promise to close both loopholes simultaneously (Section 10.2).

The form of Bell inequality violated in our experiment was first proposed by Clauser, Horne, Shimony, and Holt (CHSH) [4]. Their extension of Bell's original work accommodates non-ideal (experimentally realizable) systems and requires (i) the repeated creation of identical entangled pairs of two-level systems (qubits), (ii) independent rotations of the two qubits, and (iii) measurement of the qubits, each of which has two possible outcomes, $|0\rangle_i$ or $|1\rangle_i$, where i refers to qubit A or B. The inequality is based on the statistical outcome of correlation function measurements defined as,

$$\begin{aligned} q(\theta_A, \theta_B) = f_{00}(\theta_A, \theta_B) + f_{11}(\theta_A, \theta_B) \\ -f_{10}(\theta_A, \theta_B) - f_{01}(\theta_A, \theta_B), \end{aligned} \tag{5.1}$$

where $f_{\alpha\beta}(\theta_A, \theta_B)$ is the fraction of the total events where particle A was in state $|\alpha\rangle_A$ and particle B was in state $|\beta\rangle_B$ following rotations by polar angles θ_A and θ_B on the Bloch sphere[4]. CHSH show that all local hidden-variable theories must obey the inequality

$$B(\theta_{A1}, \theta_{A2}; \theta_{B1}, \theta_{B2}) \equiv |q(\theta_{A2}, \theta_{B2}) - q(\theta_{A1}, \theta_{B2})| + |q(\theta_{A2}, \theta_{B1}) + q(\theta_{A1}, \theta_{B1})| \leq 2. \quad (5.2)$$

According to quantum mechanics, however, this inequality can be violated for certain states and measurements. For instance, quantum theory predicts the state $|\Psi_i\rangle = (|0\rangle_A|0\rangle_B + |1\rangle_A|1\rangle_B)/\sqrt{2}$ has a correlation function $q(\theta_A, \theta_B) = \cos(\theta_A - \theta_B)$. This results in a maximum violation of Eq. (5.2) for certain settings; for example, $B(0, \pi/2; \pi/4, 3\pi/4) = 2\sqrt{2}$.

The experiment follows the same three steps as above, with a single photon qubit composed of two orthogonal polarization directions, and a single atom qubit stored in the ground state hyperfine (spin) levels of a trapped $^{111}Cd^+$ ion. As in the previous section, the atom and photon are probabilistically entangled following the spontaneous emission of a photon from the $^2P_{3/2}$ $|2,1\rangle$ excited state of the atom to multiple ground states, resulting in the entangled state: $\sqrt{1/3}\,|\downarrow\rangle\,|H\rangle + \sqrt{2/3}\,|\uparrow\rangle\,|V\rangle$ [Figure 5.2(b)].

Following the photon detection on either PMT, two phase-coherent microwave pulses are applied to the ion. The first pulse performs a complete population transfer from the $|1,1\rangle$ ground state to the $|0,0\rangle$ ground state [Fig. 5.2(c)], transferring the atomic qubit to the states $|1,0\rangle \equiv |\downarrow\rangle$ and $|0,0\rangle \equiv |\tilde{\uparrow}\rangle$, as required for atomic qubit state detection. The second pulse, resonant with the $|0,0\rangle \leftrightarrow |1,0\rangle$ transition, rotates the atomic qubit by any amount in the Bloch sphere $R_S(\theta_S, \phi_S)$ determined by the

[4]Equation 5.1 is equivalent in form to the expectation value of the parity operator, $\langle \sigma_z^{(A)} \sigma_z^{(B)} \rangle$.

pulse length and phase [Fig. 5.2(d)], and is followed by measurement of the atomic qubit [Fig. 5.2(e)].

The use of two microwave pulses is not only important for the subsequent atomic qubit detection, but also simplifies the phase-locking of atomic and photonic qubit rotations. In order to reliably rotate the atomic qubit with respect to the photonic qubit, it is important to control the microwave phase with respect to the arrival time of the photon, which occurs randomly within a 50 ns window. For example, if the atomic qubit begins in the initial state $(|\downarrow\rangle + |\tilde{\uparrow}\rangle)/\sqrt{2}$ and is rotated directly with a single microwave pulse, $R_S(\theta_S,\phi_S)$, the final state measurement would depend on the absolute phase of the microwave source, with a probability of measuring $|\downarrow\rangle$ of $P(|\downarrow\rangle) = (1 - \cos\phi_S \sin\theta_S)/2$. However, if before the qubit rotation pulse, the population of one of the qubit states is first completely transfered to another state (i.e. $|\uparrow\rangle \rightarrow |\tilde{\uparrow}\rangle$ via a $R_S(\tilde{\theta}_S = \pi,\tilde{\phi}_S)$ transfer pulse), then the final state measurement depends only on the phase *difference* between the two microwave pulses: $P(|\downarrow\rangle) = (1 - \cos(\phi_S - \tilde{\phi}_S)\sin\theta_S)/2$. Hence, the phase of the atomic qubit rotation can be easily controlled by setting the relative phase of the two microwave sources.

A complete measurement of the CHSH form of Bell inequality requires the accumulation of four correlations, with maximum violation occurring when one qubit is rotated by $\theta_A = 0, \pi/2$ and the other by $\theta_B = \pi/4, 3\pi/4$. Here, two complete inequality measurements are taken by rotating the ion by $\theta_S = 0, \pi/2$ ($\theta_S = \pi/4, 3\pi/4$), and rotating the photon by $\theta_P = \pi/4, 3\pi/4$ ($\theta_P = 0, \pi/2$). Each correlation measurement consists of approximately 2000 successful entanglement events and takes around 20 minutes, requiring about 80 minutes for the complete Bell inequality measurement. From these correlation measurements, the Bell signals are $B = 2.203 \pm 0.028$ ($B = 2.218 \pm 0.028$), where the uncertainties are statistical (Table 5.1). One possible

source of systematic error considered is the unequal efficiencies of the photon detectors, where as mentioned above, the side port of the PMT was only approximately 70% as efficient as the through port. In order to give the proper weight to the data collected on each PMT, each correlation measurement consists of two runs, in which the role of the two PMTs are reversed via a 45 degree rotation of the $\lambda/2$ waveplate.

θ_S	θ_P	q(θ_S,θ_P)	
0	$\pi/4$	0.558	
0	$3\pi/4$	-0.519	$B(\theta_{S1}{=}0, \theta_{S2}{=}\pi/2; \theta_{P1}{=}\pi/4, \theta_{P2}{=}3\pi/4) = 2.203 \pm 0.028$
$\pi/2$	$\pi/4$	0.513	
$\pi/2$	$3\pi/4$	0.613	
θ_S	θ_P	q(θ_S,θ_P)	
$\pi/4$	0	0.636	
$\pi/4$	$\pi/2$	0.461	$B(\theta_{P1}{=}0, \theta_{P2}{=}\pi/2; \theta_{S1}{=}\pi/4, \theta_{S2}{=}3\pi/4) = 2.218 \pm 0.028$
$3\pi/4$	0	-0.516	
$3\pi/4$	$\pi/2$	0.605	

Table 5.1: Results of the Bell inequality experiments.

Upon emission of the photon, the two qubits would ideally be in the entangled state $|\Psi\rangle_{ideal} = (|\downarrow\rangle |H\rangle_P + |\uparrow\rangle |V\rangle_P)/\sqrt{2}$, while the actual prepared state, represented by the density matrix ρ, has a fidelity of $\mathscr{F} = {}_{ideal}\langle\Psi|\rho|\Psi\rangle_{ideal} \approx 0.87$ [116]. Depending on the particular decomposition of the density matrix, this should produce a Bell signal between 2.09 and 2.46. Hence, our measured values agree well with the predictions of quantum mechanics and violate the Bell inequality by greater than seven standard deviations.

While these results are in good agreement with quantum mechanics, neither the detection nor the locality loopholes are closed. The locality loophole is the theory that if the measurement of one particle falls within the backwards lightcone of the other particle, then the measurement of the second particle could still be determined by local hidden variables, while the detection loophole points out that without a sufficiently high detection efficiency of the entangled pair, the subset of pairs detected must be assumed to represent a "fair sample" of all created pairs [131].

In our experiment, the probabilistic nature of photon detection leaves open the detection loophole, as the results rely on the detected events representing a fair sample of the entire ensemble. Similarly, the locality loophole is not closed since the photon's polarization rotation and detection take place approximately 1.1 meters away from the atom, and the detection of the atomic qubit takes 125 μs, falling well within the backward lightcone of the photonic detection event. On the other hand, the detection and locality loopholes have been previously closed in two separate experiments involving pairs of entangled ions where the detection efficiency of each ion is near perfect [12], and entangled photons with entangled photons that were separated by a distance sufficiently far for the "spacelike" separation of the two measurement apparatuses [6, 9]. Yet, despite a number of proposals [132, 133, 134, 54], no experiment to date has simultaneously closed both loopholes. However, as will be discussed in Chapter X, the method demonstrated in this Chapter, may provide the first step toward such a loophole-free Bell inequality test involving pairs of remotely-entangled ions [54].

CHAPTER VI

Experiments with Ions and Photon Frequency Qubits

As described in Chapter II, in addition to two orthogonal polarizations, the photonic qubit can alternatively be composed of two resolved frequencies. However, qubit rotation and detection of the two frequency components is difficult. Nonetheless, indirect evidence of the entanglement between an atomic qubit and a photon frequency qubit was demonstrated in our cadmium ion system using the technique from Figure 2.1(f) [65]. (For an detailed discussion on this experiment, see the Ph.D. thesis of Martin Madsen [114].)

A diagram of the relevant energy levels and a description of the experiment are given in Figure 6.1. First, the ion is optically pumped to $|0,0\rangle \equiv |\uparrow\rangle$, and a microwave pulse prepares the ion in a superposition of the clock states $(|\downarrow\rangle + |\uparrow\rangle)/\sqrt{2}$, where $|1,0\rangle \equiv |\downarrow\rangle$ [Figure 6.1(a)]. Next, a single π-polarized ultrafast laser pulse coherently drives the superposition to the corresponding clock states in the excited $^2P_{3/2}$ levels with near unit probability, $|2,0\rangle \equiv |\downarrow'\rangle$ and $|1,0\rangle \equiv |\uparrow'\rangle$, resulting in the superposition $(|\downarrow'\rangle + |\uparrow'\rangle)/\sqrt{2}$. Cross-coupling between the levels $|\uparrow\rangle \leftrightarrow |\downarrow'\rangle$ and $|\downarrow\rangle \leftrightarrow |\uparrow'\rangle$ is prohibited by selection rules. After spontaneous emission of a π-polarized photon into the appropriate mode, the atom and photon would be in an the entangled state $(|\downarrow\rangle|\nu_\downarrow\rangle + |\uparrow\rangle|\nu_\uparrow\rangle)/\sqrt{2}$. However, in this experiment, the entangled state is

not directly verified because measurement of the photon polarization, frequency, and emission time (with respect to the 14.5 GHz frequency qubit separation) is not performed.

The *coherence* in this excitation scheme, however, is demonstrated using a microwave Ramsey experiment. With the application of two microwave pulses alone (with the phase of the second microwave pulse phase shifted with respect to the first pulse), the Ramsey contrast is essentially perfect (circles in Figure 6.1(e)). However, if between the two microwave pulses, a single ultrafast laser pulse drives the ion to the excited state (Figure 6.1(b)), and the excited ion spontaneously decays without precise measurement of the photon parameters, then the coherence is lost (squares in Figure 6.1(e)). The uncontrolled measurement of the photon results in tracing over the photon portion of the density matrix, and the resulting loss in contrast is consistent with prior ion-photon entanglement.

To show that the excitation pulse is indeed coherently driving the superposition to the excited state, the Ramsey coherence is recovered by driving the ion back down to the ground state before spontaneous emission occurs [Figure 6.1(c)]. With a pair of picosecond laser pulses incident on the ion between the microwave pulses, the contrast reappears with a phase shift proportional to the time t spent in the excited state and the hyperfine frequency difference between the ground and excited state levels: $t(\nu_0 - \nu_1)$=(680 ps)(13.9 GHz) = 18.9π (triangles in Figure 6.1(e)). The observed contrast is only 40% of the contrast without ultrafast laser pulses, but is consistent with the limited laser power in the second pulse and spontaneous decay (probability of $\sim 23\%$) during the delay time between the ultrafast pulses [65]. While this experiment did not show the entangled state between the ion and photon frequency qubit directly, it is a proof of principle that coherence in the atomic qubit

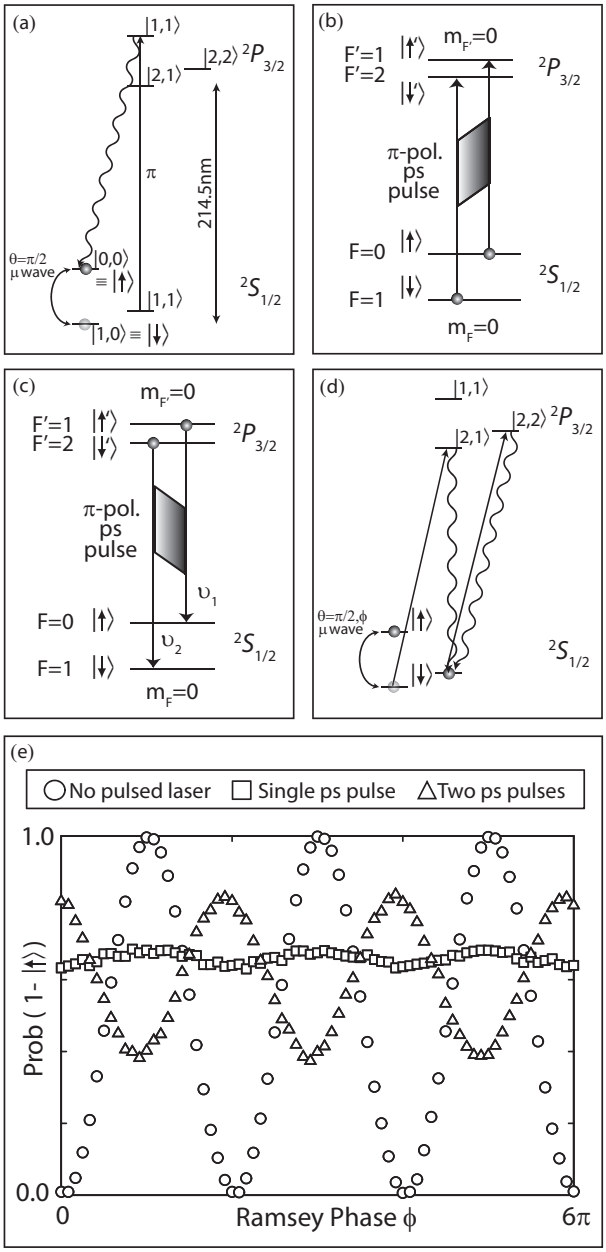

Figure 6.1: Experimental procedure for atom-photon entanglement with photon frequency qubits. (a) The ion is initialized in the state $(|\downarrow\rangle + |\uparrow\rangle)/\sqrt{2}$ via optical pumping to the $|0,0\rangle$ state and a microwave $\pi/2$ pulse. (b) The superposition of atomic qubit states is coherently driven to the $^2P_{3/2}$ excited state via a resonantly tuned π-polarized ultrafast laser pulse. (c) A second pulse drives the qubit back to the ground state a short time later. (d) A second $\pi/2$ microwave pulse with variable phase completes the Ramsey experiment and the atomic state is measured using a resonance fluorescence technique. (e) Results from the microwave Ramsey experiment. Circles show the near perfect Ramsey fringes for the case with no ultrafast laser pulses. With a single ultrafast laser pulse, the coherence is lost due to the spontaneous emission of a photon that is not measured in a controlled, precisely timed fashion (squares). The average population in the bright state is above 0.5 due to the fluorescence branching ratios [see Figure 7.2(inset)]. Upon application of a second ultrafast laser pulse, the coherence in the ion is maintained by driving the qubit states back down to the ground states (triangles) [65].

can be driven with optical fields. As will be seen in Chapter IX, the photon frequency qubit is what was used to demonstrate remote-ion entanglement.

CHAPTER VII

Toward Remote Atom Entanglement with Cadmium

With the demonstration of ion-photon entanglement with the cadmium ion system, there remain two major obstacles for remote ion entanglement: the ion as a good single photon source and the interference of the two emitted photons from two ions. This chapter discusses the progress made with the cadmium ion system, and the limitations of cadmium that ultimately led to our switch to ytterbium.

7.1 Single Photon Source

As shown at the end of Chapter III, it is important for each atom to emit only a single photon during an entanglement trial. Such a single photon source was demonstrated in our lab by optically exciting a single cadmium ion using a picosecond mode-locked Ti:sapphire laser [135]. This laser is tuned to 858 nm and is sent through a pulse picker to reduce the repetition rate from 81 MHz to 27 MHz with an extinction ratio of better than 100:1 in the infrared[1]. The pulses are frequency quadrupled through single pass nonlinear crystals and the resulting 214.5 nm laser pulses have a pulse extinction ratio near 10^{-8} and a transform-limited pulse width of about 1 ps. This allows excitation of the ion on a timescale much faster than the $\tau = 2.65$ ns excited state lifetime.

[1]The pulse picker is necessary in order to resolve the peaks in the autocorrelation function in Figure 7.1

To demonstrate that an ion emits only a single photon when excited via the ultrafast laser, a single ion is repeatedly excited with the picosecond laser resulting in a periodic emission of photons at the laser pulse separation time of 37.5 ns. The intensity autocorrelation function of the photons is recorded using a multi-channel scaler, with the results shown in Figure 7.1. The half width of each peak is given by the excited state lifetime and the peak at zero time delay corresponding to coincidentally detected photons is almost entirely suppressed. This near-perfect antibunching is highly non-classical and demonstrates that at most one photon is emitted from the ion following an excitation pulse (fundamentally limited by the possibility of emitting and detecting a photon during the excitation pulse $\sim 10^{-5}$). The residual peak at zero time delay has a height of about 2% of the other peaks, originating from diffuse scattered light from the pulsed laser. With fast electronics, this residual peak could be identically zero by vetoing photons emitted during the picosecond laser pulse.

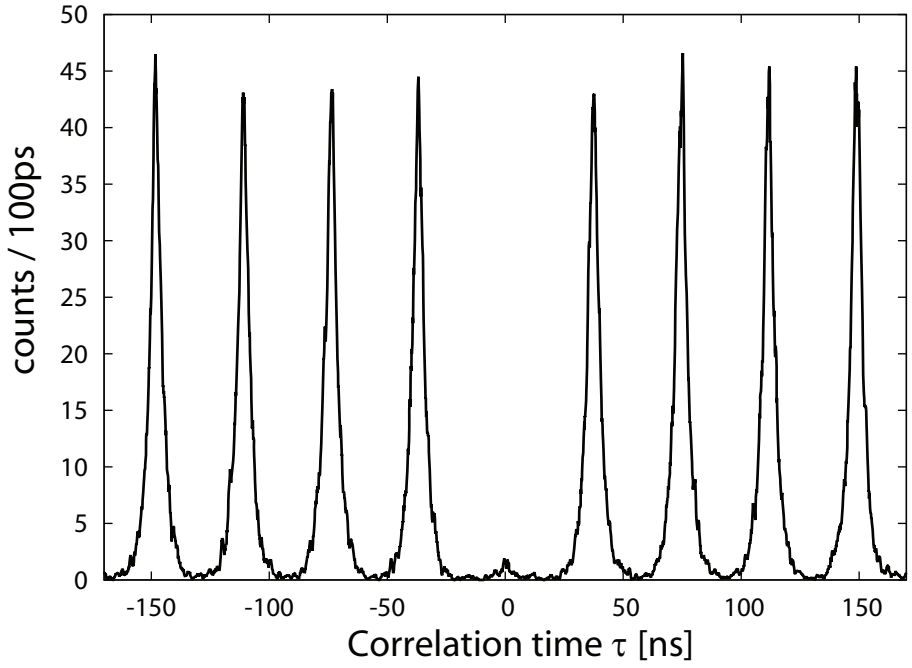

Figure 7.1: Intensity autocorrelation of the light emitted by a single ion excited by an ultrafast laser. The near perfect antibunching at $t = 0$ shows that at most one photon is emitted from an excitation pulse.

In addition to eliminating double excitations ($p_{2e} \rightarrow 0$), the use of ultrafast lasers also allows for unit-probability excitation ($p_e \sim 1$). This corresponds to performing a Rabi π pulse on the optical $S - P$ transition. We observe optical Rabi flopping by measuring the Rabi angle as a function of pulse energy.

In the experiment, the Rabi angle is measured by preparing the ion in a known initial ground state and applying a single excitation pulse of known polarization [65]. With knowledge of the fluorescence branching ratios and the ability to perform efficient state detection, Rabi flopping with the pulsed laser can be detected using every laser pulse with a high signal to noise ratio [Figure 7.2]. An alternative method would be to detect the photon scattering rate from an ion as a function of the pulse energy where Rabi angles with an odd (even) multiple of π would have a maximum (minimum) of scattered photons as the ion would be left in the excited (ground) state at the end of each pulse (as was later done in our ytterbium ion system [Figure 7.3]) [136].

In the experiment, the ion is prepared in the $|0, 0\rangle$ ground state through optical pumping as described previously. A single linearly polarized ps laser pulse excites the ion to the $P_{3/2}$ $|1, 0\rangle$ state. After a time (10 μs) much longer than the excited state lifetime, the ion has decayed back to the $S_{1/2}$ ground state levels via spontaneous emission following the fluorescence branching ratios. The atomic ground states are then measured using resonance fluorescence detection where all three $F = 1$ states are equally bright, while the $F = 0$ state is dark [130, 137, 113], with the results shown in Figure 7.2. The available power from the pulsed laser limits the Rabi rotation angle to roughly π, and the data agree well with the estimates based on the beam waist, pulse length and pulse shape [65, 114]. The probability of measuring the bright state is equal to 1/3 the probability of excitation to the $P_{3/2}$ state, as follows

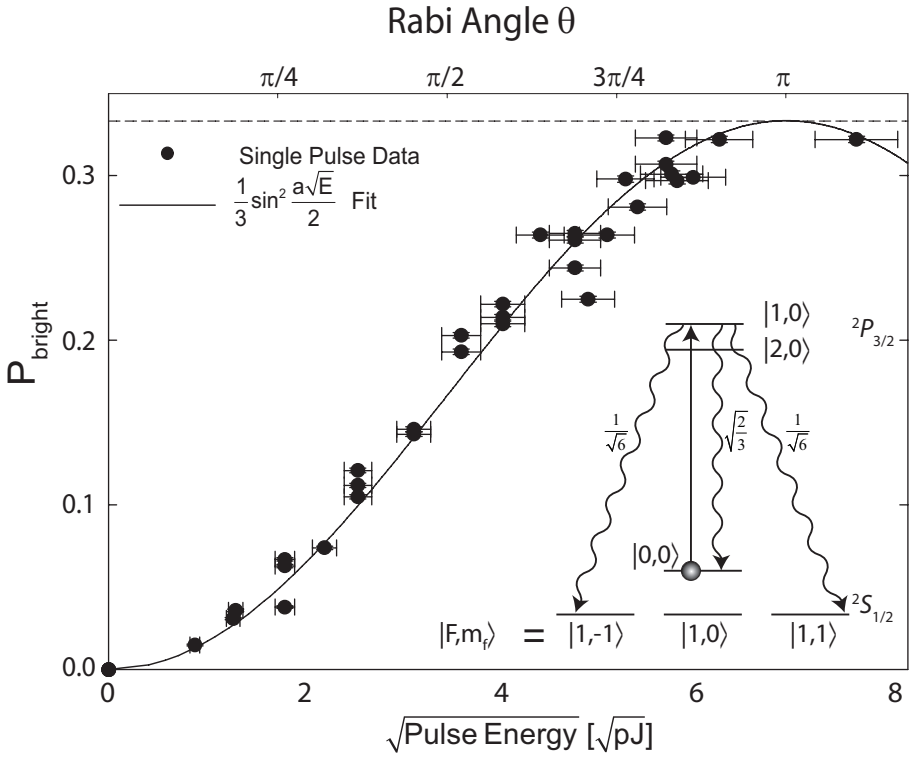

Figure 7.2: Ion bright state population as a function of pulse energy. Each point represents a collection of 60,000 runs. As the population in the excited P state is driven to unity, the bright state population approaches 1/3 (horizontal dashed line), determined by the spontaneous emission branching ratio. The data are fit to a single parameter giving a value $a = 0.42$ pJ$^{-1/2}$. INSET: Relevant energy levels for the $S-P$ Rabi oscillation experiment. A π-polarized ultrafast laser pulse excited the ion from the ground state to the excited state with variable energy. The three possible decay channels are shown with their respective fluorescence branching ratios. After a time (10 μs) following the excitation pulse, the bright state population of the ion was measured using resonance fluorescence detection.

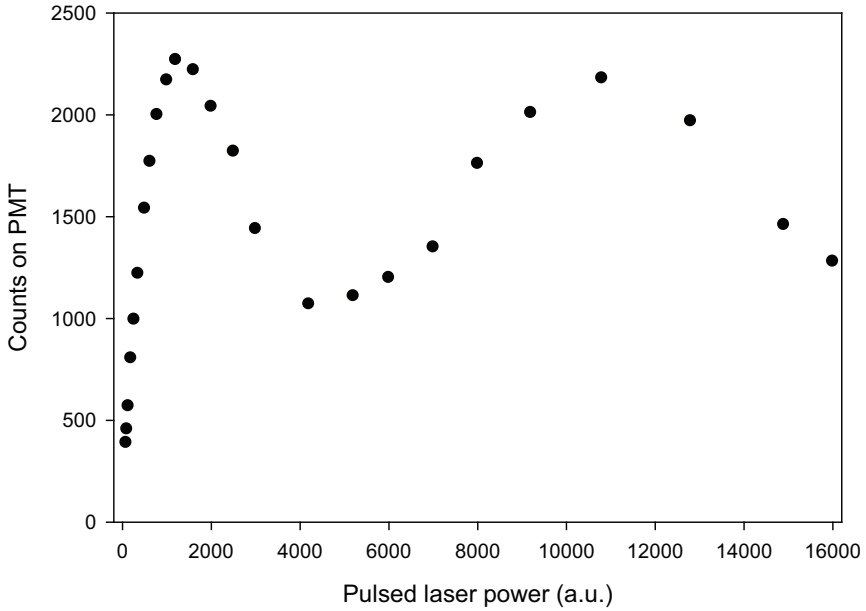

Figure 7.3: Photon scattering rate as a function of pulse energy. Rabi angles with an odd (even) multiple of π would have a maximum (minimum) of scattered photons as the ion would be left in the excited (ground) state at the end of each pulse. This data shows a maximum Rabi angle of greater than 3π, and was taken with the ytterbium system.

from the Clebsch-Gordan coefficients [Figure 7.2(inset)]. Hence, we have shown that unit excitation and single photon emission can be achieved with ultrafast laser pulses.

7.2 Two Photon Interference

With the ability to entangle atoms with their single emitted photons, the next step for remote atom entanglement is the interference of the photon modes from each atom on a beam splitter. For the demonstration of this interference in our cadmium ion system [135], two ions are aligned in a linear trap and a beam splitter setup is used to interfere the emitted photons [Figure 7.4]. In this setup, light scattered by the two ions is collected using the same f/2.1 objective lens as in Chapter V. A 600 μm pinhole is placed at the intermediate image for suppression of background photons and the intermediate image is re-imaged by a doublet lens. This image is then broken

up into two paths by a beam splitter: the transmitted and the reflected beam[2]. These two beams are directed to a second beam splitter where the light from each ion is superimposed. Irises are used to block the unwanted beams (see Figure 7.5), and the overlapping beams are directed to PMTs with a time resolution of about 1 ns [95]. The equal path lengths of the transmitted and reflected beams ensure that the photons emitted by two ions are mode-matched in size and divergence. Coarse alignment is performed by imaging the light after the second beam splitter on a single photon sensitive camera and looking at different focal planes by temporarily inserting lenses. The overall magnification of the imaging system is about 1000 and the diffraction-limited images of the two ions are separated by 2 mm, each with a spot size of 0.5 mm.

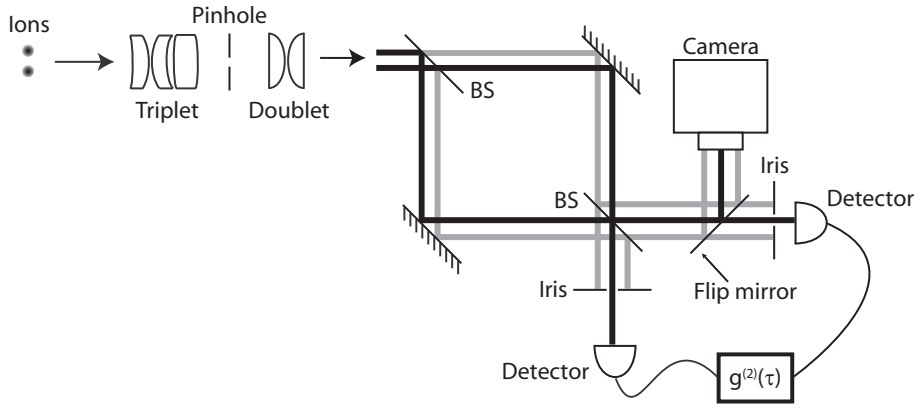

Figure 7.4: Detection system for the two-photon interference experiment. The light from the two ions is separated on a beam splitter (BS) and mode-matched on the second BS. The photons are detected on single photon sensitive photomultiplier tubes (PMTs). A camera is used for coarse alignment, and the non-overlapping photon modes are blocked by irises.

To demonstrate two photon interference, first the photon statistics of a single ion excited by a σ^+-polarized cw laser is investigated (dashed line in Figure 7.6). In this case, the $g^{(2)}$ autocorrelation function shows the expected damped Rabi oscillations [139, 140] between the ${}^2S_{1/2}$ $|1,1\rangle$ and ${}^2P_{3/2}$ $|2,2\rangle$ levels. It is unlikely that

[2]The first beam splitter serves the same role as the pickoff mirror in reference [138]. In our imaging system, however, the images from the two ions are still overlapping on this first beam splitter. The image separation from each ion is done instead at the irises.

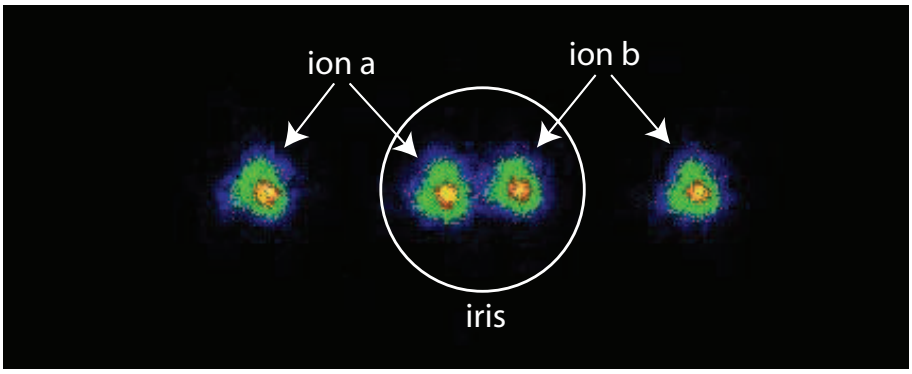

Figure 7.5: Camera image of two ions after second beam splitter. The photon modes are purposely not overlapped in this image. When overlapped, the outer images are blocked via an iris.

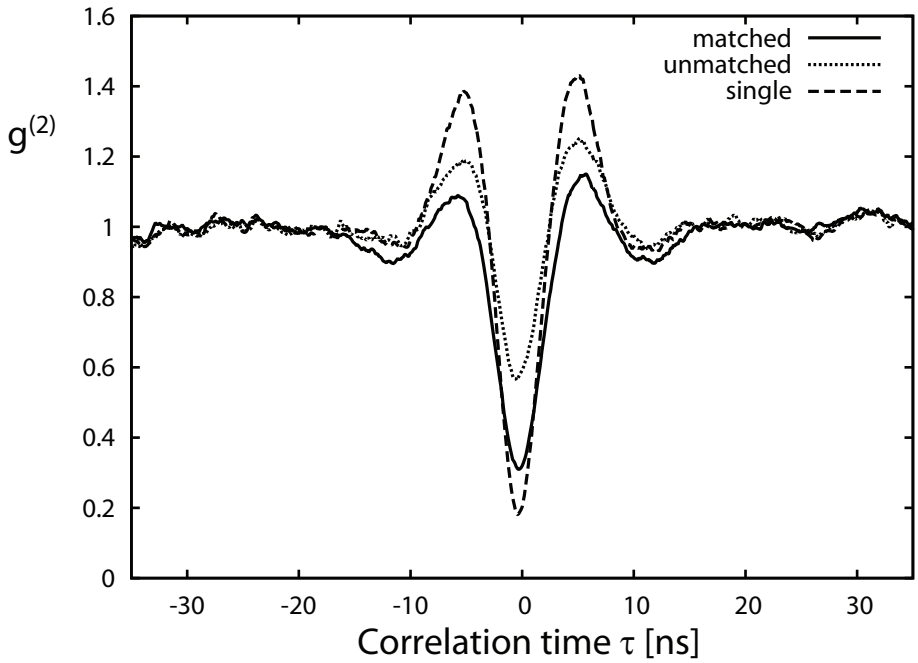

Figure 7.6: Intensity autocorrelation for cw-excitation. The dashed line shows strong antibunching for a single ion with $g_1^{(2)}(0) = 0.18$, limited by the resolution of the detection system. With this value, the expected antibunching of light from two non-overlapping ions is expected to be $g_{2,um}^{(2)}(0) = 0.59$ in good agreement with the experimental value (dotted line). If the two photon modes are matched, the interference leads to a significant reduction of coincidence detections (solid line). The measured antibunching was $g_{2,m}^{(2)}(0) = 0.31$, corresponding to a mode overlap of about 57%.

two photons are emitted from one ion in close proximity since after emission of a single photon, the ion is assured to be in the ground state. The maximum observed antibunching for the single ion is $g_1^{(2)}(0) = 0.18$. Theoretically, this antibunching should go all the way to $g_1^{(2)}(0) = 0$, but experimentally this is not possible due to the time resolution and dark counts of the PMTs [135].

Next, two ions are equally illuminated and purposefully not mode-matched on the beam splitter. In this case, half of the signal results from two photons from the same ion, and the other half result from one photon from each ion. Since these photon modes are not matched on the beam splitter, the detected photons are uncorrelated. We therefore expect a reduced antibunching, $g_{2,um}^{(2)}(0) = \frac{1}{2}(1 + g_1^{(2)}(0)) \approx 0.59$, in good agreement with the measurement (dotted line in Figure 7.6).

If the photon modes from each ion are matched on the beam splitter, then the photons always leave on the same output port, and thus no coincident detections are observed [141]. The suppression of coincidence events is clearly visible in the autocorrelation signal of the mode-matched ions (solid line in Figure 7.6) and has a measured $g_{2,m}^{(2)}(0)$ of 0.31. This corresponds to an interference signal of about 57% (amplitude matching of 75%), and compares well to the results observed in reference [138]. This mode overlap is clearly not perfect and is limited by phase front distortions of the short wavelength photons from the two atomic sources as they sample different parts of many optical surfaces before finally interfering on the beam splitter.

In order to entangle two remotely located atoms, the use of single mode optical fibers will almost certainly be required. Since remote-atom entanglement relies on the interference of two photons on a beam splitter, interfering the two photon modes would require very high stability of the atom and collection optics with respect to

the beam splitter, as well as good spatial mode matching from the two imaging systems. With free-space mode-matching, any relative motion of the trapped atoms and the imaging optics would ruin the entanglement fidelity by producing false positive detection events. However, in the fiber coupled case, effects such as mechanical vibrations and thermal drifts of the ion and ion trap will simply lower the rate of coincidence counts since instead of detecting photons that are not mode-matched, these photons are filtered out by the fiber.

7.3 Limitations of the Cadmium Ion System

An attempt was actually made to interfere the photon modes from two cadmium ions located in different traps separated by $\sim$ 1 m. In the end it was found that not only was the mode of each imaging system significantly different (Figure 7.7), but even more detrimental was the drift of each ion position — caused perhaps by the movement of the trap or chamber itself, or by slowly varying electrode voltages (Figure 7.8). As seen in Figure 7.9, an attempt was made to characterize the mode overlap of each ion, but the drifting position made adjustment prohibitive. Due to these issues, we believe that single mode fibers are necessary for high-fidelity remote atom entanglement. Unfortunately, in the cadmium system the spontaneously emitted photons are deep in the ultraviolet at 214.5 nm where it is very difficult to use optical fibers. We attempted to use photonic crystal fibers, which have a decent mode profile, but the fiber attenuation was too large ($\sim$ 10 dB/meter) for efficient transmission and mode cleaning. These issues are what led us to try the interference experiment reported in the previous section with both ions in the same trap. This setup allowed each ion to have a similar spatial profile (since they were collected with the same f/2.1 lens), and be insensitive to common-mode motion, due to the

interferometer-like setup.

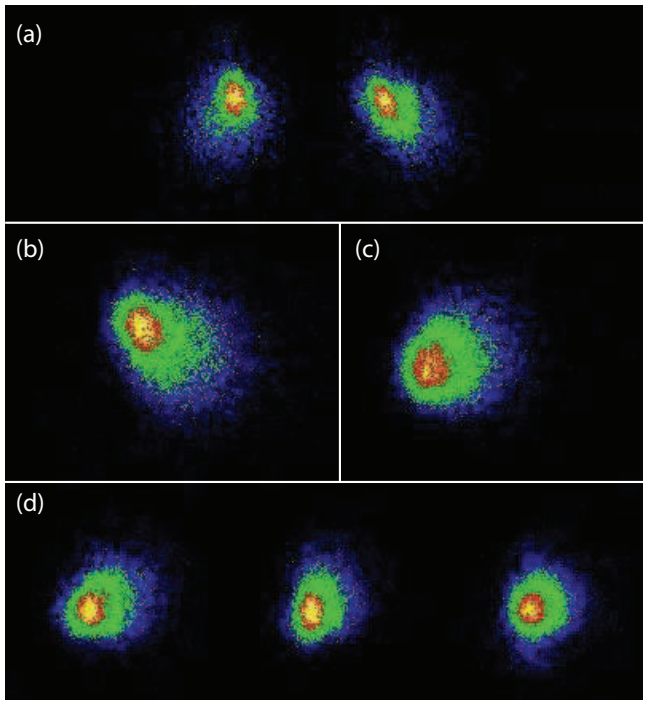

Figure 7.7: Free space photon mode quality from different Cd ions. (a) Two ions from two different traps imaged simultaneously. It is clear that the modes from each imaging system are different. (b-c) Image of an ion from a single trap before (a) and after (b) rotation of the triplet imaging lens by 90 degrees. (d) The three triplet lenses can be independently adjusted. These three images show different (random) adjustments of the lenses.

Even though the interference reported in this chapter may have been sufficient to measure photon-mediated entanglement between the two ions, this interference was reported with cw excitation. As mentioned on more than one occasion, high-fidelity entanglement suggests the excitation of the ions with a laser pulse much shorter than the lifetime of the ion. We attempted to repeat the interference experiment with the ultrafast picosecond laser, but were never able to measure substantial interference. It is our belief that this lack of interference was due to the high energy photons of the (not perfectly focused) 214.5 nm pulsed laser liberating electrons from the trap electrodes, creating a locally high pressure in the trapping zones and affecting the ion position. While, this theory was not fully investigated, evidence supports the

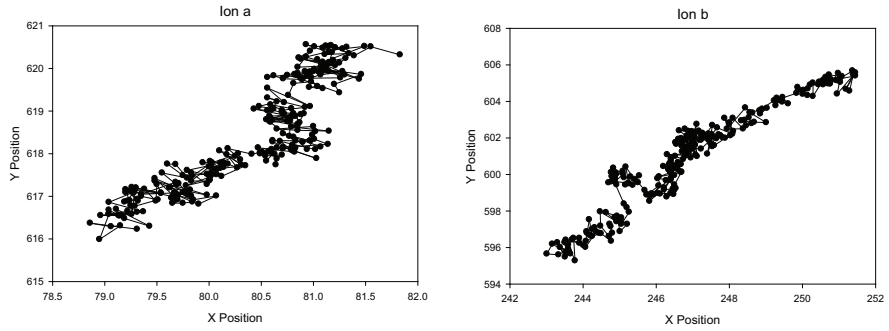

Figure 7.8: Ion position on the camera vs. time. The center position of each ion was taken every 30 seconds, where the x-axis and y-axis positions are measured in pixels on the camera (1 pixel = 25 μm). The size of the ion on the camera is approximately 500 μm. Ion a drifted up and to the right while ion b drifted down and to the left.

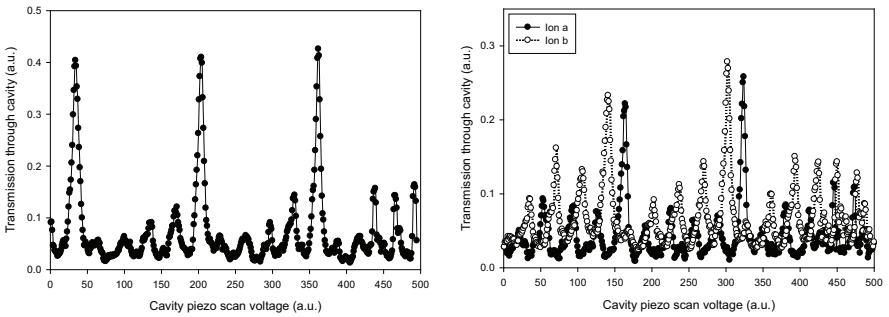

Figure 7.9: Photon mode characterized via an optical cavity. (a) Light transmission through a cavity of photons emitted from a single ion. (b) Comparison of the photon modes from two ions in separate traps. Alignment was very difficult due to the drifting position of the ions and the cavity length.

emission of electrons from the trap surfaces, as this was one method for loading cadmium ions prior to photoionization [142]. Furthermore, when running an experiment with alternating time periods of cw and pulsed excitation, the cw excitation yielded results similar to those in Figure 7.6, whereas the pulsed excitation did not show interference.

While the lack of fibers was enough for us to abandon cadmium in favor of ytterbium for the remote-ion entanglement experiment, the lack of available laser power at the resonant transition of cadmium was also an important issue. As shown in Section 7.1, the available laser power after frequency quadrupling was sufficient for driving a π pulse, however, twice as much power would have been necessary for the simultaneous excitation of two ions in two separate vacuum chambers. Certainly, ytterbium has its downsides — more complicated atomic structure requiring more lasers and more complex atomic transitions — but the high power which is available since only frequency doubling the main 739 nm laser is necessary and the use of single-mode fibers at 369.5 nm made the switch very favorable.

CHAPTER VIII

Quantum Interference of Photon Pairs from Distant Ytterbium Ions

This chapter describes our first experiments with ytterbium ions. I discuss our results on the improved demonstration of the ion as a single photon source as well as the observation of quantum interference between pairs of single photons emitted from two remotely trapped atomic $^{174}Yb^{+}$ ions. While two photon interference has been observed previously with photons generated in a variety of physical processes and systems, including nonlinear optical down-conversion [86, 143], quantum dots [144], atoms in cavity-QED [145, 146], atomic ensembles [147, 148, 149], two nearby trapped neutral atoms [138], and our cadmium ion system [135], reported here is the first observation of interference between two single photons emitted from two remotely trapped atoms.

The experimental apparatus consists of two congeneric four-rod rf traps, each storing a single atomic ytterbium ion, and located in separate vacuum chambers separated by about one meter. The storage time of each trap is on the order of days, and impressively, all the data presented in this chapter was obtained with the same two ions.

Laser cooling localizes the ions to within the resolution of the diffraction-limited imaging optics but well outside the Lamb-Dicke limit. The ions are excited with ul-

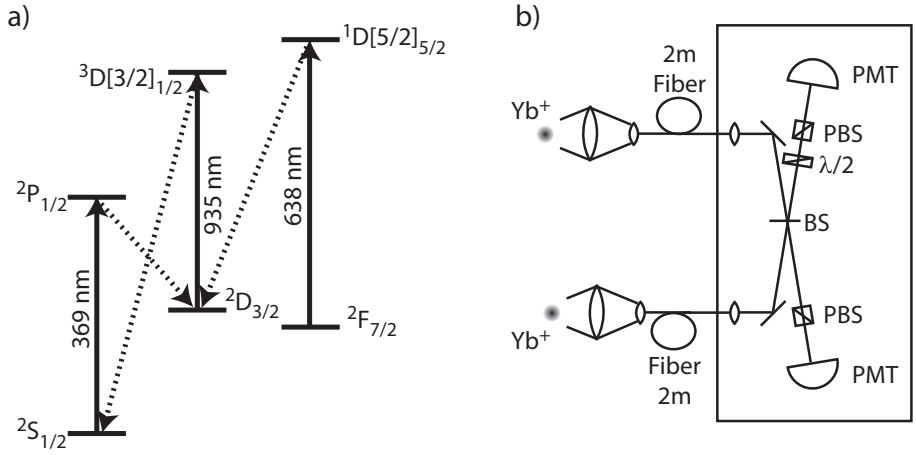

Figure 8.1: The Ytterbium set-up for two photon interference. a) Relevant level scheme of $^{174}Yb^+$. b) Schematic of the detection system. The unpolarized light from each $^{174}Yb^+$ ion is collected using a triplet lens with a numerical aperture of 0.23 and a working distance of 13 mm. It is coupled into a single-mode fused silica fiber using an aspheric collimation lens with a numerical aperture of 0.6. About 20% of the light collected from each ion is transmitted through the 2 m fibers. The light from both fibers is collimated with a monochromatic lens and mode-matched on a polarization independent beam splitter (BS). Behind the beam splitter two removable polarizers (PBS) can be used to select parallel polarization. Inserting a $\lambda/2$-plate allows the detection of perpendicularly polarized photons. Subsequently, the light is detected by two photon-counting photomultipliers (PMT) with a quantum efficiency of about 20% and a time resolution of about 1 ns. The photon arrival times at the photomultipliers are recorded using a time to digital converter with a resolution of 4 ps (PicoQuant PicoHarp300). The contrast of the interferometer is measured using 369.5 nm laser light to be better than 96%.

trafast laser pulses generated by the same mode-locked Ti:sapphire laser as described in previous chapters tuned to a center wavelength of 739 nm. Each pulse is then frequency doubled to 369.5 nm through a phase-matched LBO nonlinear crystal. An electro-optic pulse picker is used to reduce the pulse repetition rate from 81 MHz to 8.1 MHz with an extinction ratio of better than $10^4 : 1$ in the UV. The second harmonic is filtered from the fundamental with a prism, split between the two traps using a beam splitter and aligned to arrive at the two ions within 100 ps of each other. Each pulse has a near transform-limited pulse duration of 2 ps and excites the ions on a timescale much faster than the excited state lifetime of 8.1 ns [150]. The pulse energy is adjusted to simultaneously excite both ions with near unit probability.

Two re-entrant viewports at opposing sides of each trap are used to simultaneously image the ions in free space and couple light scattered from the ions into single mode optical fibers. In free space, a telescope similar to that used in the cadmium setup (Chapter VII) is used to image scattered photons on a camera to monitor loading and to verify the presence of a single $^{174}Yb^+$ ion in each trap. Fiber coupling is realized from the opposite side of the trap using a second objective lens to collect spontaneously emitted photons (Fig. 8.1b). Each beam is focused onto a single mode fiber using an aspheric lens. About 20% of the spontaneously emitted photons collected by the objective are transmitted through the 2 m fiber (estimated by comparing the count rate on the free space PMT to the count rate on the PMT behind the fiber). The ion light transmitted through the single mode fibers is collimated and mode-matched on a 50/50 beam splitter at as small an angle of incidence as possible (approximately 10° such that the splitting is polarization independent). The light emerging from the beam splitter is detected using photomultipliers. Removable polarizers and a removable $\lambda/2$-waveplate allow detection of unpolarized photons, or

photons of parallel or perpendicular polarization. The arrival times of the photons at the photomultipliers are recorded using a time to digital converter.

8.1 Single Photon Source

To demonstrate that the excitation of an ion with an ultrashort pulse leads to the emission of at most one photon, we first analyze the light scattered by a single $^{174}Yb^{+}$ ion by blocking the fluorescence from one of the two traps. We employ a repetitive sequence consisting of a 40 μs measurement interval and a 10 μs cooling interval. During the cooling interval the ion is Doppler cooled with cw-light only, while during the measurement interval the ion is excited only by ultrafast laser pulses with a 124 ns pulse separation. From the arrival times of the photons at the photomultipliers the intensity autocorrelation function $g^{(2)}(\tau)$ is evaluated and shown in Figure 8.2.

As in the cadmium experiment from Chapter VII, the periodic ultrafast excitation of the ion leads to peaks at multiples of the pulse separation time. Since the ions are excited on a timescale much faster than the excited state lifetime, the emission probability during the excitation pulse is negligible. Thus, the ion is transfered into the excited state and the spontaneously emitted photons have an exponential envelope [95]. Therefore the peaks in the autocorrelation function have a two-sided exponential decay where the 1/e half width is given by the 8.1 ns lifetime of the excited state. Compared to the cadmium experiment, the coincidence peak at zero time delay is completely suppressed (neglecting dark counts on the PMTs). This is because of the fibers used in the ytterbium experiment which geometrically filter out all unwanted scattered photons — only photons emitted by the ion have the correct spatial mode to couple into the fiber. Theoretically, the probability to scatter two

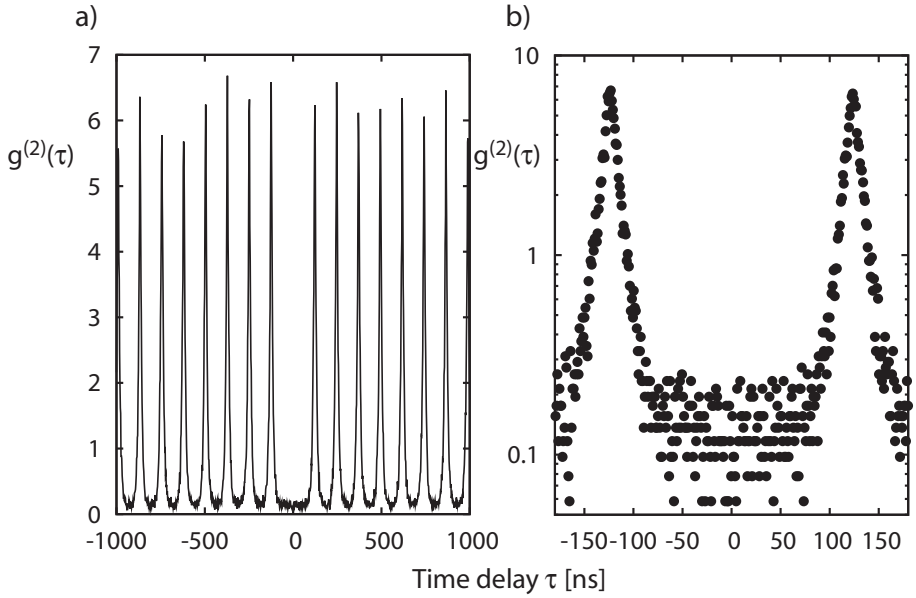

Figure 8.2: Intensity autocorrelation of the light emitted by a single $^{174}Yb^{+}$ ion excited by picosecond pulses. a) The periodically emitted photons from the pulsed excitation lead to peaks at multiples of the 124 ns pulse repetition time. b) The near-perfect photon anti-bunching, revealed by the logarithmic scale, proves that at most one photon is emitted from an excitation pulse. The correlation function is evaluated from the stored photon arrival times using 2 ns binning. The probability to detect a photon from one excitation pulse is 6×10^{-4}. The data shown were integrated 3 hours; 1.5 hours for each ion.

photons from one ion excited with one pulse is limited by the emission probability of an excited atom during the excitation pulse ($\approx 10^{-5}$ here). This very clean single photon source is a good starting point for the observation of two-photon interference and necessary for high fidelity photon mediated ion entanglement.

8.2 Two Photon Interference

To observe two-photon interference, the single ions in both traps are excited simultaneously by picosecond laser pulses and the fluorescence photons are combined on the beam splitter. The polarizers after the beam splitter are used to measure the coincidences of parallel polarized photons. To measure coincidences of perpendicularly polarized photons in the two output ports of the beam splitter, a $\lambda/2$-waveplate is added in front of one polarizer. The resulting cross correlation functions are shown

in Figure 8.3. For perpendicular polarization the photons are distinguishable and do not interfere, thus we find a peak at zero delay. This peak has half the area of the others, because at zero delay each ion can only contribute one photon, while for non-simultaneous pulses each ion can produce both photons in the correlation measurement. Integrated over photon pairs detected within 8 ns of each other (one lifetime) this peak consists of 1087 coincidences corresponding to a coincidence detection probability of 1.4×10^{-8} per excitation pulse or an absolute coincidence rate of about 0.1/ s. For parallel polarization of the two photons, the two-photon interference eliminates coincidence detections. In our case the remaining peak at zero delay, after subtracting dark count background, has an amplitude of about 5% of the perpendicularly polarized signal, corresponding to a 95% interference contrast. Integrating all photon pairs that are detected within 8 ns of each other, including dark counts, we detect 14% of the photon pairs we observe for perpendicular polarization[1].

The interference contrast observed here, including dark counts, could potentially lead to a entanglement fidelity of about 90%, limited by the ratio between photon detection events and dark counts. This ratio can be improved by lowering detector dark counts, achieving a higher detection efficiency, or by collecting photons from a larger effective solid angle. This potential fidelity would surpass the threshold needed to violate a Bell inequality, however as will be seen in the next chapter, the resulting fidelity is somewhat lower.

[1]It was later discovered that a large fraction of the "dark counts" were due to the cw laser still exciting the ions during the 40 μs measurement interval. This was caused by an rf switch not sufficiently attenuating the rf that drives the AOM.

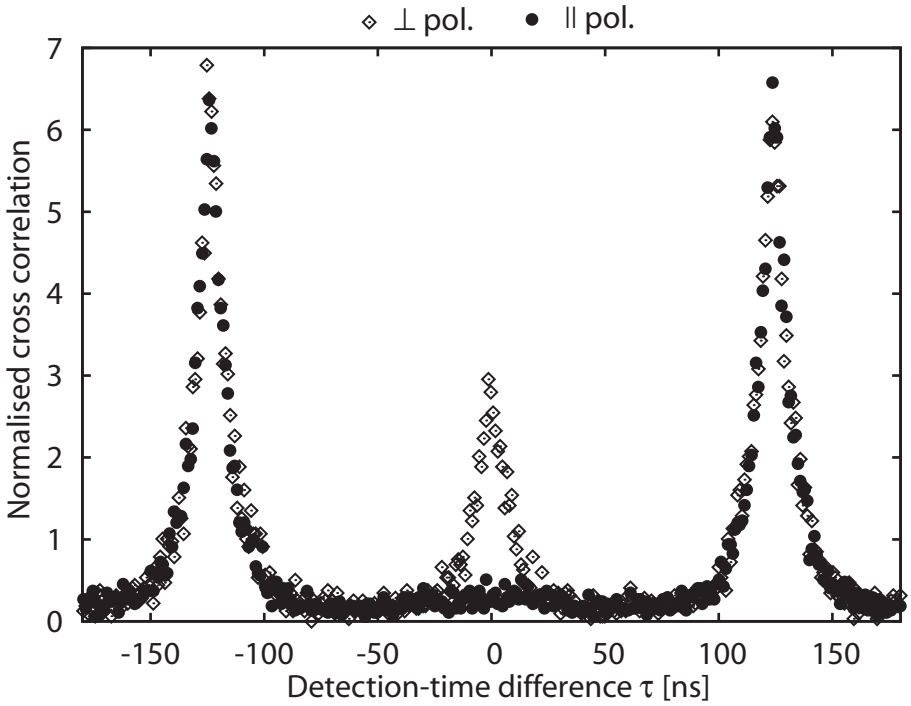

Figure 8.3: Normalized intensity cross correlation of photons emitted by two ions. For perpendicular linear polarization (diamonds) the photons from the two ions are distinguishable, thus we observe a peak at zero delay. In contrast to the peaks at longer delay times, for which the two photons can be emitted by the same ion, the two photons leading to a coincidence at zero delay must be emitted by different ions. Thus the peak at zero delay has half the area than the peaks at longer delay times. Integrating all photon pairs with a detection-time difference of $|\tau| < 8\,\mathrm{ns}$ results in a coincidence detection probability of 1.4×10^{-8} per excitation pulse (or 2×10^{-8} for the photon pairs with less than 16 ns detection-time difference). For parallel linear polarization (dots) the two-photon interference suppresses the coincidence detection of two photons on different output ports of the beam splitter. Including dark counts, the number of photon pairs with less than 8 ns and 16 ns detection-time difference is reduced by 86% and 81%, respectively. Each curve was integrated for about 4 hours and evaluated using a 1 ns binning.

CHAPTER IX

Entanglement of Ytterbium ion quantum bits at a distance

With the demonstration of ion-photon entanglement in Chapter V, and a good single photon source and two-photon interference in Chapter VIII, all necessary requirements were met for the entanglement of two remotely located ions.

In this chapter, I report our experimental realization of quantum entanglement of two fixed single-atom quantum memories separated by one meter. Two remotely-located trapped atomic ions each emit a single photon, and the interference and detection of these photons heralds the entanglement of the atomic quantum bits. The entanglement is characterized by directly measuring qubit correlations with near perfect detection efficiency.

As with the previous chapter, we trap and laser cool the single ytterbium ions in two congeneric four-rod linear rf ion traps. However, this time $^{171}Yb^{+}$ ions are used in order to have an atomic qubit. As depicted in Fig. 9.1(a), a magnetic field of $B \approx 5.5$ Gauss provides a quantization axis for definition of the photon polarization and the internal atomic qubit level is stored in the hyperfine levels of the $^{2}S_{1/2}$ ground state.

Figure 9.2 shows a diagram of the relevant energy levels of $^{171}Yb^{+}$ along with the step-by-step description of the experimental procedure. After Doppler cooling,

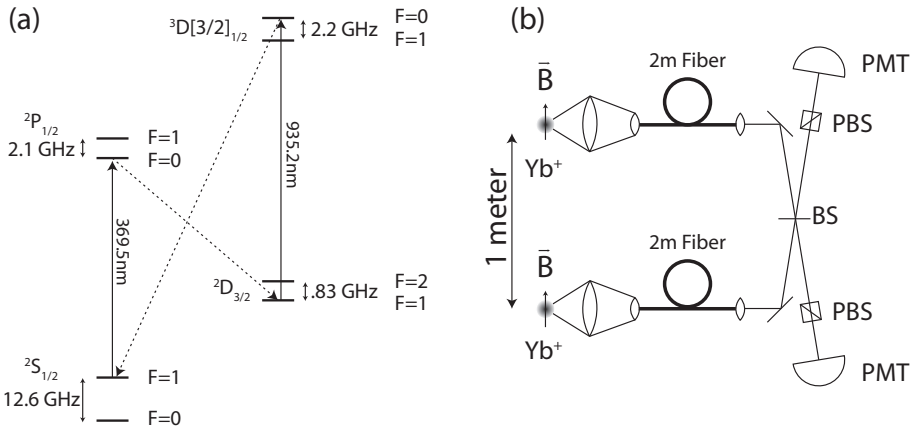

Figure 9.1: Relevant energy levels for $^{171}Yb^+$. (a) The $^2S_{1/2} \leftrightarrow {}^2P_{1/2}$ transition is driven by light at 369.5 nm. A frequency-doubled continuous-wave diode laser is used for Doppler cooling, state initialization, and state detection of the ion, whereas the excitation of the ion for single photon generation is accomplished with a mode-locked, frequency-doubled Ti:Sapphire laser with a pulse duration of 2 ps [151]. When excited to $^2P_{1/2}$, the ion can decay to the $^2D_{3/2}$ level with a branching ratio of ~ 0.005. A diode laser at 935.2 nm pumps the ion out of this state through the $^3D[3/2]_{1/2}$ level. (b) Two ions are trapped in independent vacuum chambers separated by approximately one meter. Spontaneously emitted photons from each ion are collected by an f/2.1 imaging lens and coupled into single-mode fibers. The polarization of each emitted photon is defined with respect to the applied magnetic field $\vec{B}$ oriented perpendicularly to the collection direction. Polarization is maintained through the fibers and can be adjusted via polarization-controlling paddles. The output of each fiber is spatially mode-matched on a 50/50 non-polarizing beam splitter (BS) leading to an interference contrast of greater than 97%. Polarizers (PBS) are used to filter out the photons of unwanted polarization and the remaining photons are detected on photon counting photomultiplier tubes (PMT).

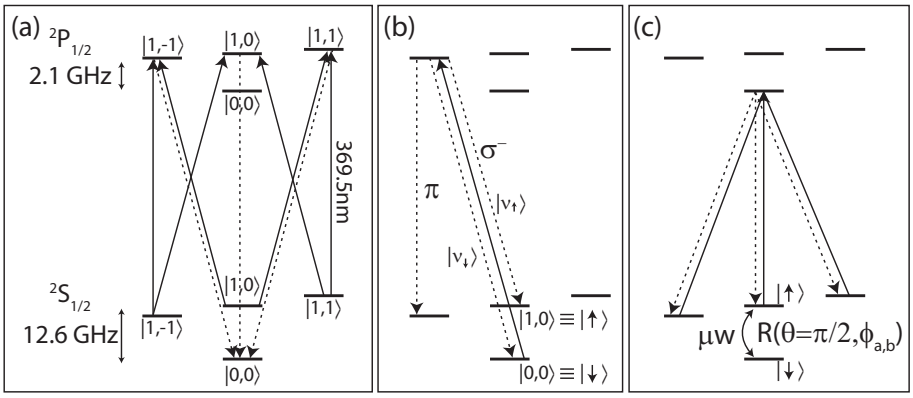

Figure 9.2: Experimental procedure of $^{171}Yb^+$ entanglement experiment. (a) Each atomic qubit is initialized to the $|F, m_F\rangle = |0, 0\rangle$ hyperfine ground state via a 500 ns optical pumping pulse resonant with the $^2S_{1/2}|F = 1\rangle \leftrightarrow {}^2P_{1/2}|F = 1\rangle$ transition including all polarizations. (b) Each ion is excited with a 2 ps σ^--polarized optical pulse, resulting in the spontaneous emission of at most a single photon to either the $^2S_{1/2}|1, -1\rangle$ state while emitting a π-polarized photon or to the $|\uparrow\rangle$ and $|\downarrow\rangle$ states while emitting a σ^--polarized photon. The π-polarized photon is filtered out by a polarizer resulting in the entangled state $(|\uparrow\rangle |\nu_\uparrow\rangle - |\downarrow\rangle |\nu_\downarrow\rangle)/\sqrt{2}$. Steps (a) and (b) are repeated on both ions until simultaneous detection occurs on the two PMTs. (c) Upon simultaneous detection of a photon on each PMT, an optional microwave (μw) rotation pulse prepares each atomic qubit for measurement in a rotated basis, followed by measurement of the atomic qubits using standard trapped ion fluorescence techniques, here by resonantly driving all $^2S_{1/2}|F = 1\rangle \leftrightarrow {}^2P_{1/2}|F = 0\rangle$ transitions.

pulses of light tuned to the $^2S_{1/2} \leftrightarrow {}^2P_{1/2}$ transitions initialize, excite, and detect the internal states of the ions. First, a 500 ns pulse of light resonant with the $^2S_{1/2}|F = 1\rangle \leftrightarrow {}^2P_{1/2}|F = 1\rangle$ transition prepares each ion in the $|0, 0\rangle$ state with greater than 98% efficiency. Next, a 2 ps σ^--polarized laser pulse from pulsed laser excites the ion to the $^2P_{1/2}|1, -1\rangle$ state. The ion is prepared in the excited state with an excitation probability of $p_e \approx 0.5$ (see Appendix A.3 for why p_e is not unity), and spontaneously decays to either the $^2S_{1/2}|1, -1\rangle$ state while emitting a π-polarized photon or to the $|1, 0\rangle \equiv |\uparrow\rangle$ and $|0, 0\rangle \equiv |\downarrow\rangle$ states while emitting a σ^--polarized photon (Fig. 9.2(b)). The spontaneously emitted photon at 369.5 nm is collected perpendicular to the quantization axis and is coupled into a single-mode fiber. Along this direction, the polarizations of the π and σ^- decay channels are orthogonal [116], and the π-polarized photons are filtered out with polarizers (see Figure 2.1(e)). The resulting entangled state between the ion and the photon is $(|\uparrow\rangle |\nu_\uparrow\rangle - |\downarrow\rangle |\nu_\downarrow\rangle)/\sqrt{2}$,

where $|\nu_\downarrow\rangle$ and $|\nu_\uparrow\rangle$ refer to the two resolved frequencies comprising the photonic qubit, as described in Chapter II. The two frequency components are separated by the 12.6 GHz ground state hyperfine splitting.

The output modes of the fibers from each trap are directed onto the two input ports of a 50/50 non-polarizing beam splitter with a transverse spatial mode-overlap leading to an interference contrast of greater than 97% (Fig. 9.1(b)) [151]. The photons emerging from the beam splitter are sent through polarizers to filter out the π-polarized decay channel and then to photon-counting photomultiplier tubes (PMTs), each of quantum efficiency $\eta \approx 0.15$.

While the end-to-end coupling efficiency through each fiber is only $\zeta \approx 0.2$, the use of single-mode fibers is essential for the rejection of photons in other spatial modes that would not properly interfere and thereby lower the entanglement fidelity [138, 151]. Temporal mode-matching of photons is accomplished by matching the arrival times of the photon from each ion on the beam splitter to better than 30 ps. Compared to the 8.1 ns photon duration, this temporal matching corresponds to a decrease in the mode overlap of under 1%. Finally, spectral matching of the photonic qubits is accomplished by equalizing the magnetic field at the traps to better than 30 mG, resulting in a photonic frequency mismatch of less than 0.2% of the $1/(2\pi\tau) \approx 20$ MHz photon bandwidth. Doppler broadening of the photon emission, from both residual motion of the Doppler-cooled ions and micromotion [152], is expected to affect the interference by well under 1% [151, 146].

When each ion emits a photon into the mode of interest, the quantum state of

the system before the photons interact on the 50/50 beam splitter is:

$$\frac{1}{2}[(|\uparrow\rangle_a|\nu_\uparrow\rangle_a - |\downarrow\rangle_a|\nu_\downarrow\rangle_a) \otimes (|\uparrow\rangle_b|\nu_\uparrow\rangle_b - |\downarrow\rangle_b|\nu_\downarrow\rangle_b)] = \frac{1}{2}(|\Phi^+\rangle_{\text{atom}}|\Phi^+\rangle_{\text{photon}} + |\Phi^-\rangle_{\text{atom}}|\Phi^-\rangle_{\text{photon}} - |\Psi^+\rangle_{\text{atom}}|\Psi^+\rangle_{\text{photon}} - |\Psi^-\rangle_{\text{atom}}|\Psi^-\rangle_{\text{photon}}). \quad (9.1)$$

With the photon modes matched on the 50/50 beam splitter, the photons exit on different ports only if they are in the antisymmetric state $|\Psi^-\rangle_{\text{photon}} = (|\nu_\uparrow\rangle_a|\nu_\downarrow\rangle_b - |\nu_\downarrow\rangle_a|\nu_\uparrow\rangle_b)/\sqrt{2}$, respecting the symmetry of the overall photonic wavefunction [86]. Therefore, coincident photon detection in the two output ports of this beam splitter ideally projects the ions onto $|\Psi^-\rangle_{\text{atom}} = (|\uparrow\rangle_a|\downarrow\rangle_b - |\downarrow\rangle_a|\uparrow\rangle_b)/\sqrt{2}$ [54]. (This result assumes equal path lengths from each ion to the beam splitter. A simple extension considering differing path lengths can be found in Appendix D.) Following such a heralded entanglement event, near resonant microwave pulses coherently rotate the trapped ion qubits and prepare them for measurement in a rotated basis. The atomic qubit measurement is performed using standard trapped ion fluorescence techniques with an average detection efficiency greater than 97% (Fig. 9.2(c)).

We first measure the state of the two ions following the coincident photon detection without microwave rotations. Since the expected resulting ion-ion entangled state is $|\Psi^-\rangle_{\text{atom}}$, the atomic wavefunction should have odd parity ($|\uparrow\rangle_a|\downarrow\rangle_b$ or $|\downarrow\rangle_a|\uparrow\rangle_b$). The probability distribution from 274 coincidence detection events is shown in Figure 9.3 with a resulting probability of measuring odd parity $p_{\uparrow\downarrow} + p_{\downarrow\uparrow} = 0.78 \pm 0.02$. Here, p_{ab} refers to the probability of measuring the two atomic qubits (ions a and b) in the given spin states.

To verify the entanglement, we repeat the experiment and measure in a rotated basis. Each ion is rotated through a Bloch polar angle of $\theta = \pi/2$ by applying

microwaves near the measured $|\uparrow\rangle_i \leftrightarrow |\downarrow\rangle_i$ frequency splitting of 12.642821 GHz (Fig. 9.2(c)). The two atomic qubit transition frequencies are matched to better than 100 Hz, so they are essentially equal over the time scale of the rotations. We vary the relative phase $\Delta\phi = \phi_b - \phi_a$ of the rotations at the two ions by detuning the applied microwaves by 10 kHz from resonance and delaying the microwave pulse on one ion with respect to the other. Here ϕ_i refers to the microwave phase on ion $i = a, b$ and a 100 μs delay results in a phase difference of $\Delta\phi = 2\pi$. Figure 9.4 displays the resulting oscillations of the measured atomic qubit parity as a function of the relative phase of the $\pi/2$ rotations. The contrast of this oscillation is directly related to the coherence between $|\downarrow\rangle_a |\uparrow\rangle_b$ and $|\uparrow\rangle_a |\downarrow\rangle_b$.

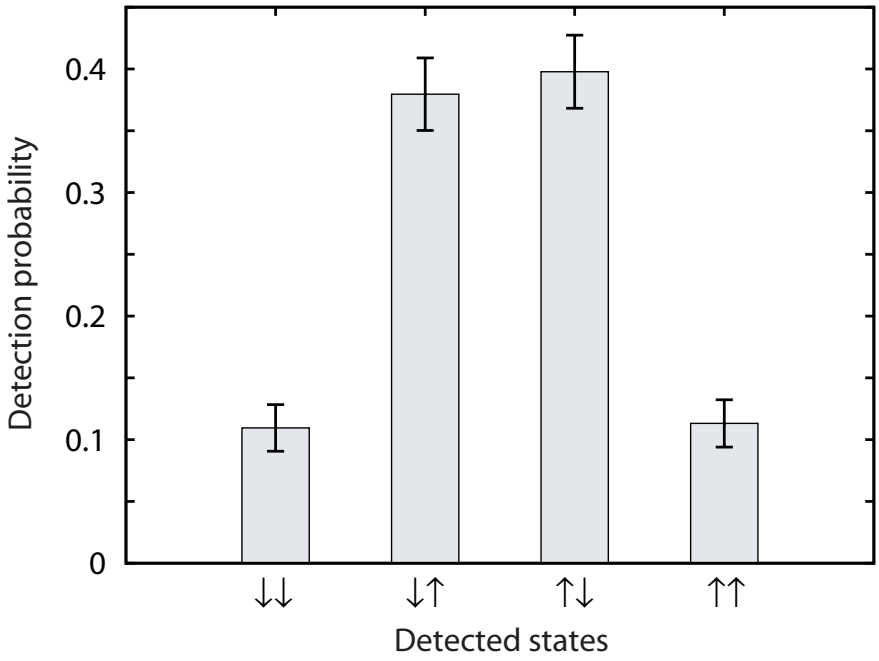

Figure 9.3: Measured probabilities in the unrotated basis (no atomic qubit rotation before measurement) conditioned upon coincident detection of photons on each PMT (photon pairs with less than 16 ns detection-time difference). The measured probabilities are $p_{\downarrow\downarrow} = 0.11 \pm 0.02$, $p_{\downarrow\uparrow} = 0.38 \pm 0.03$, $p_{\uparrow\downarrow} = 0.40 \pm 0.03$, and $p_{\uparrow\uparrow} = 0.11 \pm 0.02$, thus odd parity is found with a probability of $p_{\uparrow\downarrow} + p_{\downarrow\uparrow} = 0.78 \pm 0.02$. The errors are statistical and are collected from 274 coincidence detection events.

From these measurements, we calculate a fidelity of $\mathscr{F} = 0.63 \pm 0.03$ and a lower bound on the entanglement of formation to be $\mathscr{E} \geq 0.12 \pm 0.03$ as described in

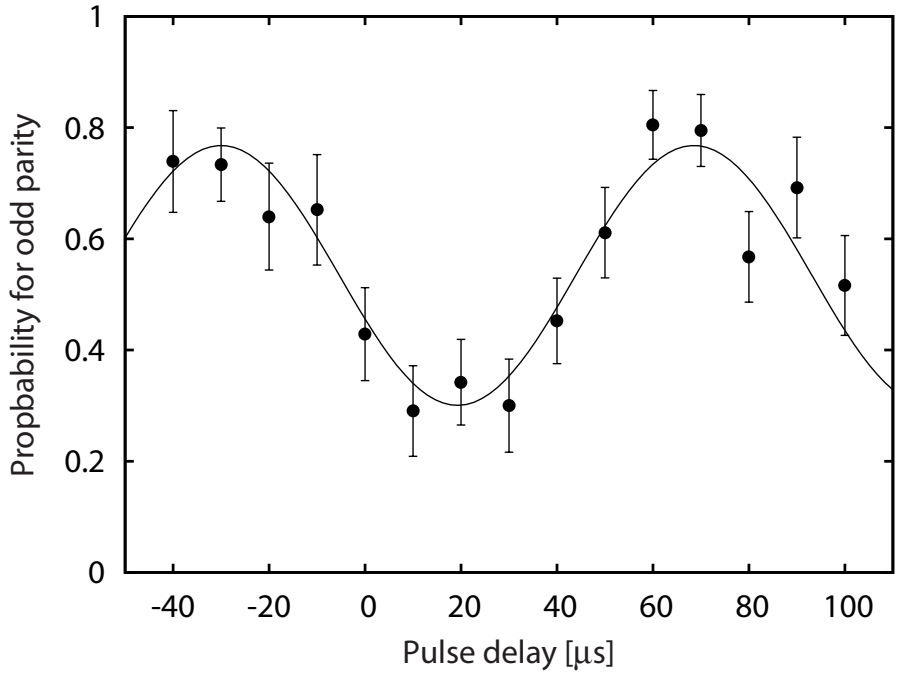

Figure 9.4: Measured probabilities in the rotated basis. Probability of measuring odd parity of the atomic qubits after rotations on each ion by a polar angle of $\pi/2$ on the Bloch sphere. The horizontal axis corresponds to the delay of the microwave pulse on one ion with respect to the other. Because of the 10 kHz detuning of the applied microwave radiation from resonance, the relative phase of the microwaves pulses, $\Delta\phi = \phi_b - \phi_a$, has a period of 100 μs. The solid line is a fit to the data resulting in a contrast of 0.47 ± 0.05, where the absolute phase of the interference pattern depends on the difference in microwave transmission lines to each ion. Results are from a total of 502 coincidence detection events.

Appendix C.2. The results are limited mainly by dark counts on the PMTs which lead to false events in $\sim 20\%$ of the measured coincidence events. Other factors contributing to the decrease in fidelity include imperfect atomic state detection (limited to $\geq 97\%$ for each ion), imperfect mode-matching on the 50/50 beam splitter (3%), mixing of the photon polarizations owing to the nonzero solid angle (1.5% of detected photons result from a $\Delta m_F = 0$ decay), excitations to the wrong atomic state ($\sim 1\%$), and imperfect rotations of the atomic qubit ($\sim 1\%$). Sources of error from imperfections in the optical fibers and magnetic field fluctuations are estimated to affect the measured entanglement by less than 1%.

As mentioned above, the remote-atom entanglement is a probabilistic process. The success probability $P_{\text{a-a}}$ in a given trial depends on the efficiency of generating a single photon from each ion in a specific mode and detecting the photons in coincidence. In our excitation scheme (Fig. 9.2(b)), each ion has a probability $p_e \approx 0.5$ of emitting a single photon after the excitation pulse, and only $\beta \sim 0.995$ of the emitted photons are at 369.5 nm due to the branching ratio to the $^2\text{D}_{3/2}$ state. The detection probability of each photon depends on the light collection solid angle $\Delta\Omega/4\pi \approx 0.02$, coupling efficiency and transmission through the single-mode fiber ζ, transmission through other optical elements $T \sim 0.8$, and the quantum efficiency of the detectors η. In addition, half of the collected photons are π-polarized and are filtered out by the polarizer [116]. Finally, since only the $|\Psi^-\rangle_{\text{photon}}$ state results in the two photons exiting the 50/50 beam splitter in different output ports, there is an additional factor of 1/4 in our success probability: $P_{\text{a-a}} = \frac{1}{4}[\frac{1}{2}\eta\zeta T\beta p_e(\Delta\Omega/4\pi)]^2 \approx (0.25)[(0.5)(0.15)(0.2)(.8)(0.995)(0.5)(0.02)]^2 \approx 3.6 \times 10^{-9}$. With an experiment repetition rate of $R_{\text{a-a}} \approx 5.5 \times 10^5$ s^{-1}, this results in a heralded entanglement event approximately every 9 minutes.

Since this rate is proportional to the square of the probability of measuring an emitted photon, improvements in the generation of single photons in the desired mode can significantly increase this yield. Possible improvements include increasing the probability of excitation to unity by using an alternative excitation scheme or collecting the emitted photons along the quantization axis where the radiation strength of the emitted photons is greatest. However, the most substantial improvement would be to place the ion within an optical cavity, which would allow the effective solid angle $\Delta\Omega/4\pi$ to approach unity. Not only would these changes increase the success probability, they would also substantially improve the entanglement fidelity by lowering the relative contribution of dark count events.

CHAPTER X

Conclusion and Outlook

The demonstration of photon-mediated atom-atom entanglement opens up a number of possibilities for tests on quantum theory as well as for scalable quantum information processing. In this concluding chapter, I describe how this entanglement method can be used for either deterministic quantum computation, or alternatively quantum computing using a measurement based approach. I also discuss the use of this entanglement for an implementation of a loophole free Bell inequality.

10.1 Scaling to Complex Quantum Networks

As the number of atoms grows within a trap used for a quantum register, so too does the complexity of the system. While there is progress in constructing more elaborate atom traps capable of deterministically separating and shuttling atoms [42, 43, 45, 44], an alternative approach is to keep traps relatively simple and have the atoms remain in a given trapping zone where the necessary atomic motional control is relaxed. This approach requires the ability to interconnect different zones via photon-mediated entanglement [Figure 10.1].

Recent progress has shown that deterministic quantum gates can be constructed for remotely located atoms even with the use of probabilistic entanglement [89]. Even though the entanglement is probabilistic, it is heralded, and one can simply repeat the

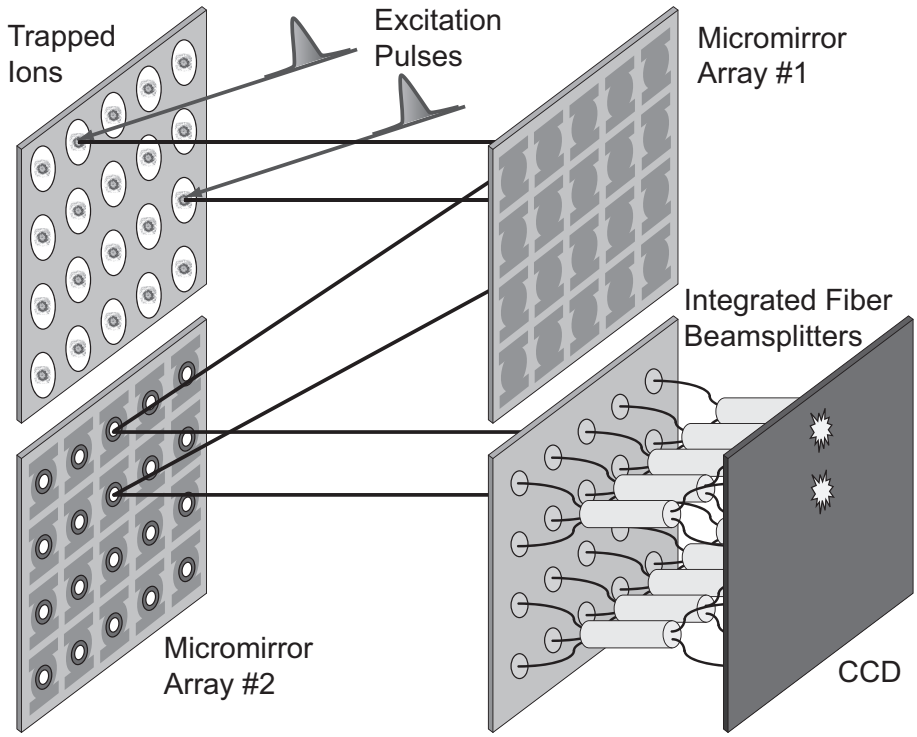

Figure 10.1: Entanglement device capable of entangling multiple atoms simultaneously using micromirror arrays [153]. Any pair of atoms can be entangled by routing the emitted photon from each atom to a beam splitter where single photon detections can project the atoms into an entangled state. Parallelism is possible with this setup for N atoms with $2N$ mirrors and $N/2$ beam splitter pairs.

procedure until the detectors announce the creation of the entangled pair of atoms. Once successful, the entanglement shared by the two atoms can be further used with local deterministic gates within each trapping zone. This is in contrast to the coupling of small samples of atomic gases through photonic channels [21, 129], where the post-selected entanglement between light and atoms [154, 155] and the observation of entanglement signatures between remotely-located atomic ensembles [122, 126, 17] is perhaps suitable only for quantum communication.

10.1.1 Deterministic Quantum Computation and Quantum Repeaters One approach to scalable quantum computation based on probabilistic entangling gates is to have an array of trapping zones, each containing two atoms — a "logic atom" and an "ancilla atom" denoted as i and i' respectively [Figure 10.2(a)] [89]. The purpose of the logic atoms is to encode all quantum information, and the ancilla atoms, linked using the probabilistic entangling protocol, are used as a "quantum bus". Once successful entanglement between the ancilla atoms is established, conventional local deterministic gates allow for an effective quantum gate between the two logic atoms. The resulting logic gate is deterministic because the quantum information stored within the logic atoms is not affected by unsuccessful attempts to entangle the ancilla atoms. This can be assured by either spatial separation of the logic and ancilla atoms so that laser operations on one atom do not affect the other, or by using different atomic species [156, 157, 158] where the two atoms could be in very close proximity since light resonant for operations on one atom would not affect the other.

There are four necessary steps to create deterministic remote atom entanglements: (1) attempt entanglement of the ancilla atoms until successful, (2) apply local deterministic motional CNOT gates on each logic-ancilla pair, (3) measure the ancilla

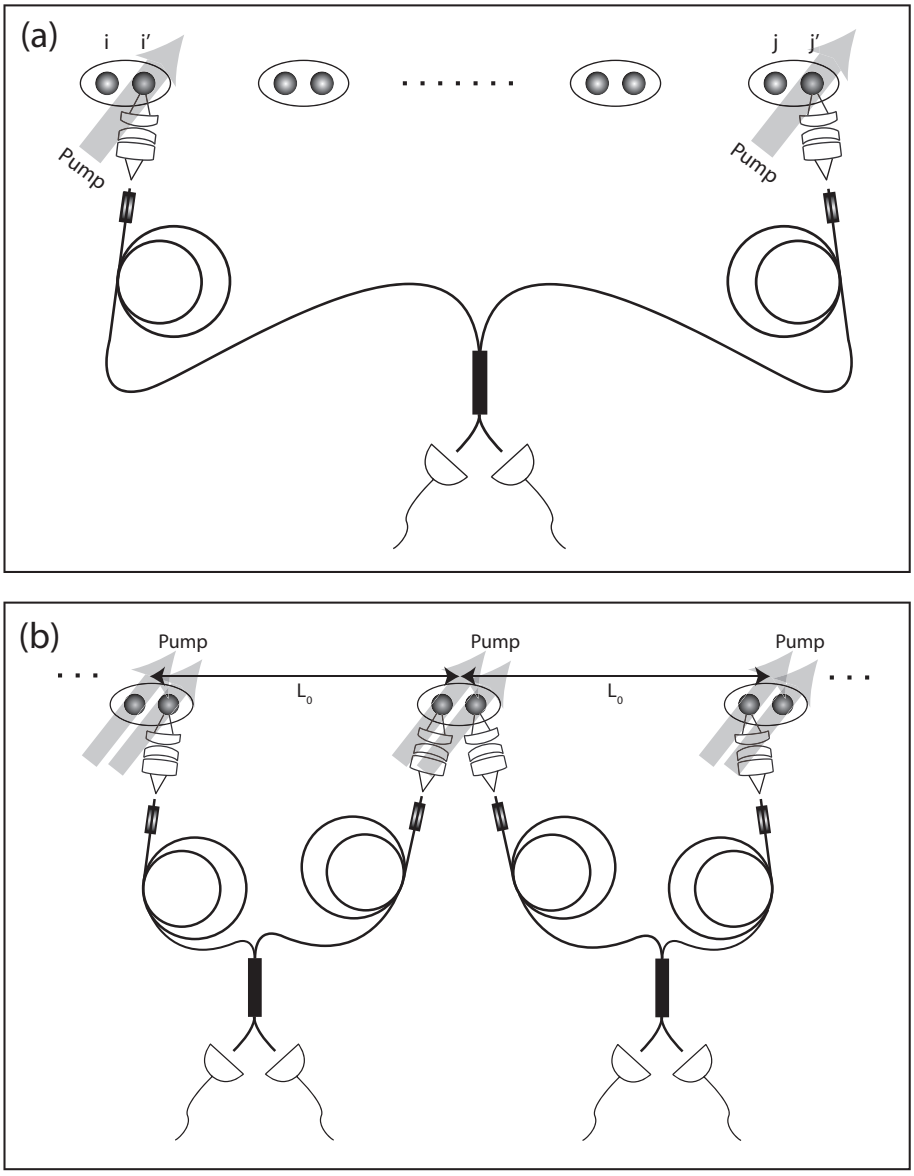

Figure 10.2: Scalable deterministic quantum computation with probabilistic photon-mediated entanglement. (a) Schematic of the quantum computation model based on probabilistic photon-mediated entanglement between atoms. The ancilla atoms (i', j') are entangled through the probabilistic protocols described in the text, and deterministic gates on the logic atoms (i, j) are constructed from local motional gates and probabilistic remote ancilla entanglement. (b) Schematic of quantum repeaters with trapped atoms based on probabilistic remote entanglement and local Coulomb interactions.

atoms in the appropriate bases, and (4) apply single qubit rotations to the logic atoms based on the measurement results. The speed of each four-step procedure is limited by the first step. With a probability of successful entanglement $P_{\text{a-a}}$ (of order $p^2 p_e^2$) the average time for completion of the remote CNOT gate is $T_{\text{rep}}/P_{\text{a-a}}$, where as before, T_{rep} is the time needed for an ancilla entanglement trial.

Efficient quantum repeaters can also be constructed using this setup, allowing reliable quantum information transfer over very long distances [Figure 10.2(b)]. In addition to the entanglement probability mentioned previously, one must also consider the probability of photon loss within the fiber connecting the atomic nodes. This lowers the probability of successful ancilla atom entanglement to $P'_{\text{a-a}} = P_{\text{a-a}} P_{\text{fiber}}$, where $P_{\text{fiber}} = e^{-\alpha L_0}$ is the photon attenuation in the channel over the communication distance L_0, and α is the fiber attenuation coefficient. The time necessary to connect two nearest-neighbor segments (distance of L_0) would be $T_1 = T_{\text{rep}}/P'_{\text{a-a}}$. This leads to a next nearest neighbor communication time of $T_2 = 2T_1$, and hence over n segments (total distance $D = nL_0$) of $T_n = nT_1 = De^{\alpha L_0} \left(T_{\text{rep}}/P_{\text{a-a}}\right)/L_0$. This linear scaling with distance compares favorably to the exponential scaling behavior if no repeater nodes are used: $T_n = e^{\alpha D} \left(T_{\text{rep}}/P_{\text{a-a}}\right)$.

10.1.2 Measurement-Based Quantum Computation Even though the above model for quantum computation is efficiently scalable with probabilistic entanglement between ancilla qubits, the robustness of the computation relies on the ability to perform local deterministic gates. Recent advances have shown that even if *all* entangling gates are probabilistic with arbitrarily small probability, one can still realize efficient quantum computation based on the use of deterministic single-bit operations and quantum memory [48, 47]. The proof of this result is most convenient with the cluster-state approach to quantum computing. The cluster-state model is com-

putationally equivalent to the conventional circuit model, but in terms of physical operations, it is quite different [159]. In this model, one first prepares a large-scale entangled state called the cluster state. Together with single-bit operations, the cluster state with a two-dimensional geometry becomes sufficient for universal quantum computation [159]. As deterministic single-bit operations for trapped atoms has been demonstrated, the task then reduces to how to realize large scale cluster states with only probabilistic entangling gates.

A pictorial description of the generation of cluster states with atomic qubits is shown in Figure 10.3. The first step in creating a 2-dimensional (2-D) cluster state is to generate long 1-D cluster chains. One could start with entanglement of two atoms, and then get these atoms further entangled with others one by one through the probabilistic gates. However, this direct approach leads to very inefficient (super-exponential) scaling of the required resources due to the probabilistic nature of the gate operation [48]. For preparation of 1-D cluster states, a way to overcome the inefficient scaling is through the divide-and-conquer protocol [48, 47] (also known as the quantum repeater protocol in [129]). With this approach, short 1-D clusters of length n are created and their end qubits are entangled through the probabilistic gate [Figure 10.3(a)]. If the entanglement attempt between the end qubits is successful, then a 1-D cluster of $2n$ qubits is made. If the attempt is unsuccessful, then only the end qubits and their nearest neighbors need to be removed from the cluster, rather than the entire system losing its entanglement. The process is then repeated with the two clusters, now each of a different length. Because this approach connects two cluster chains of almost equal lengths with the probabilistic gates, the number of connections grows logarithmically with the size of the chain, which is critical for efficient scaling.

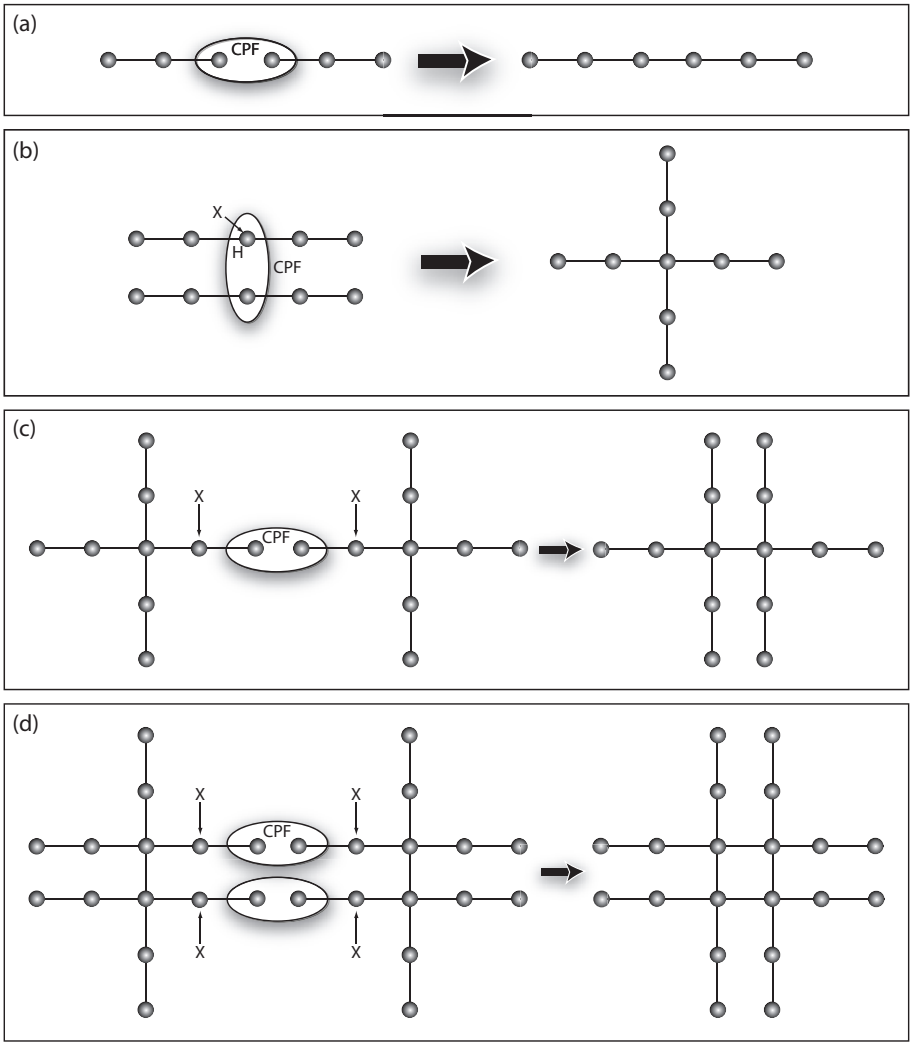

Figure 10.3: Illustration of the necessary steps for construction of cluster states. (a) A controlled phase flip entangling (CPF) gate is used to extend the length of a 1-D cluster. (b) Construction of a cross-shaped cluster from two 1-D cluster chains. A Hadamard gate (H) is applied on the middle qubit of one chain and a CPF gate connects the two middle qubits. Finally an X measurement on one middle qubit removes the extra atom. (c-d) Construction of a square lattice cluster state from the cross-shaped cluster states. CPF gates combine the shapes along ends of the crosses and X measurements are used to remove the remaining redundant qubits.

Since 1-D cluster states are not sufficient for universal computation, 2-D clusters need to be built from the 1-D chains. A straightforward extension of the divide-and-conquer method will not work as 2-D and 1-D geometries have very different characters [47], in particular for the number of the boundary qubits. In order to create 2-D cluster states, these 1-D clusters are first combined into a special type of state, called the cross state, as shown in [Figure 10.3(b)], where 1-D chains are first linked in their middles creating a cross shaped cluster after a single-bit measurement. These cross states with four sufficiently long tails can be used as the basic building blocks for the 2-D geometry [47]. Once a cross is created, two such crosses are linked together via their long 1-D tails. If the tail is sufficiently long, the two clusters can be connected almost deterministically before running out of qubits along the tail. Once connected, the remaining tail qubits separating the cross sections can be removed via single bit X measurements, finally creating the joined cluster [Figure 10.3(c)]. These steps can be repeated to create a 2-D cluster of any size. The fidelity of the cluster state approach is not affected by the probabilistic nature of linking the atoms together since the unsuccessful atoms are removed from the system. The scaling of the computational resources with this approach was demonstrated in Reference [47]. Supposing the success probability of the entangling gate is $P_{\text{a-a}}$, it has been proven there that the computational overhead to prepare a large-scale two-dimensional cluster state scales nearly polynomially with $1/P_{\text{a-a}}$ and n, where n is the total number of qubits in the cluster.

10.2 Loophole Free Bell Inequality Violation

As mentioned previously, in addition to applications in quantum information, the entanglement protocols of this thesis can be used for tests on quantum theory,

particularly for a loophole free Bell inequality test. Recent results have shown that atom-photon experiments themselves can be used for a loophole free Bell inequality violation [160, 161], but the difficulty for these experiments is that the probability to detect the emitted photon $P_{\text{a-p}}$ must be ≥ 0.43, requiring cavity QED techniques and significant improvements in photodetectors at the required wavelengths. Perhaps a more feasible option is via photon-mediated remote-atom entanglement [54].

This begins by first entangling two atom-photon pairs simultaneously in distant locations. Next, the emitted photon from each atom is directed to an intermediate location where a partial Bell state analysis is performed [162, 163], thus projecting the remotely-located atoms into a known entangled state. This entangled-atom pair is the starting point for a loophole-free Bell inequality test, which is completed by independently rotating each atom on the Bloch sphere, followed by qubit state detections (Figure 10.4). By reducing the time needed for the atomic qubit rotation and detection to 50 μs (0.5 μs), a separation of $L = 15$ km (150 m) is sufficient to satisfy the time constraints of the locality loophole [15, 18]. With this shorter detection time, sufficiently high atomic qubit detection efficiency is still possible to close the detection loophole. In the ion trap system, transmission of the ultraviolet photons over the necessary distance to the analyzer would be difficult with current technologies. However, one could also perform the experiment with a more suitable photon color via frequency conversion [164]. Additionally, one could use a quantum repeater method, entailing intermediately-located atom traps, thereby decreasing the distance any one photon needs to travel [165, 166, 89].

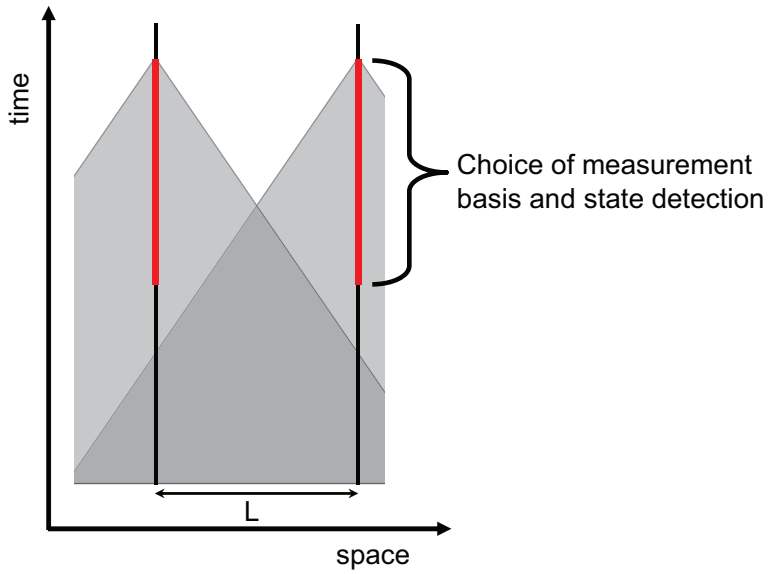

Figure 10.4: Timing requirements for a loophole free Bell inequality violation. For a distance L between ions a and b, the total time required for the choice of basis and the completion of the detection cannot be larger than L/c, where c is the speed of light. This ensures that the measurement of one ion falls outside the backward lightcone of the other ion.

APPENDICES

APPENDIX A

Three Level Systems

The three level system is one that has come up several times throughout this thesis. In all cases, it has been of the form shown in Figure A.1 with resonant coupling between the $|0\rangle \leftrightarrow |2\rangle$ and $|1\rangle \leftrightarrow |2\rangle$ states, each of strength $\Omega = dE/\hbar$. Additionally, during the interaction time, the three levels do not undergo spontaneous decay. The Schroedinger equation for this system can be written as:

$$\begin{cases} \frac{dc_0}{dt} = -i\Omega c_2 \\ \frac{dc_1}{dt} = -i\Omega c_2 \\ \frac{dc_2}{dt} = -i\Omega(c_0 + c_1). \end{cases} \tag{A.1}$$

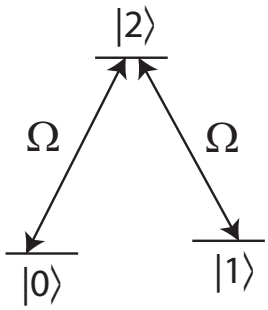

Figure A.1: General setup for relevant three level systems.

Below, I list three different relevant initial conditions.

1. The ion begins in $|0\rangle$: $c_0(t=0)=1,\ c_1(t=0)=0,\ c_2(t=0)=0$. The resulting solution is

$$\begin{cases} c_0 = \frac{1}{2}(\cos(\sqrt{2}\Omega t)+1) \\ c_1 = \frac{1}{2}(\cos(\sqrt{2}\Omega t)-1) \\ c_2 = \frac{-i}{\sqrt{2}}(\sin(\sqrt{2}\Omega t)). \end{cases} \tag{A.2}$$

This results in the probability to find the ion in each state of

$$\begin{cases} |c_0|^2 = \cos^4(\frac{\Omega t}{\sqrt{2}}) \\ |c_1|^2 = \sin^4(\frac{\Omega t}{\sqrt{2}}) \\ |c_2|^2 = \frac{1}{2}\sin^2(\sqrt{2}\Omega t). \end{cases} \tag{A.3}$$

2. The ion begins in $(|0\rangle+|1\rangle)/\sqrt{2}$: $c_0(t=0)=1/2,\ c_1(t=0)=1/2,\ c_2(t=0)=0$. The solution in this case is

$$\begin{cases} c_0 = \frac{1}{\sqrt{2}}\cos(\sqrt{2}\Omega t) \\ c_1 = \frac{1}{\sqrt{2}}\cos(\sqrt{2}\Omega t) \\ c_2 = i\ \sin(\sqrt{2}\Omega t), \end{cases} \tag{A.4}$$

resulting in the measurement probability of

$$\begin{cases} |c_0|^2 = \frac{1}{2}\cos^2(\sqrt{2}\Omega t) \\ |c_1|^2 = \frac{1}{2}\cos^2(\sqrt{2}\Omega t) \\ |c_2|^2 = \sin^2(\sqrt{2}\Omega t). \end{cases} \tag{A.5}$$

3. As a final example, consider the evolution when the ion begins in $(|0\rangle-|1\rangle)/\sqrt{2}$: $c_0(t=0)=1/2,\ c_1(t=0)=-1/2,\ c_2(t=0)=0$. The solution in this case

does not evolve due to destructive interference:

$$\begin{cases} |c_0|^2 = \frac{1}{2} \\ |c_1|^2 = \frac{1}{2} \\ |c_2|^2 = 0. \end{cases} \tag{A.6}$$

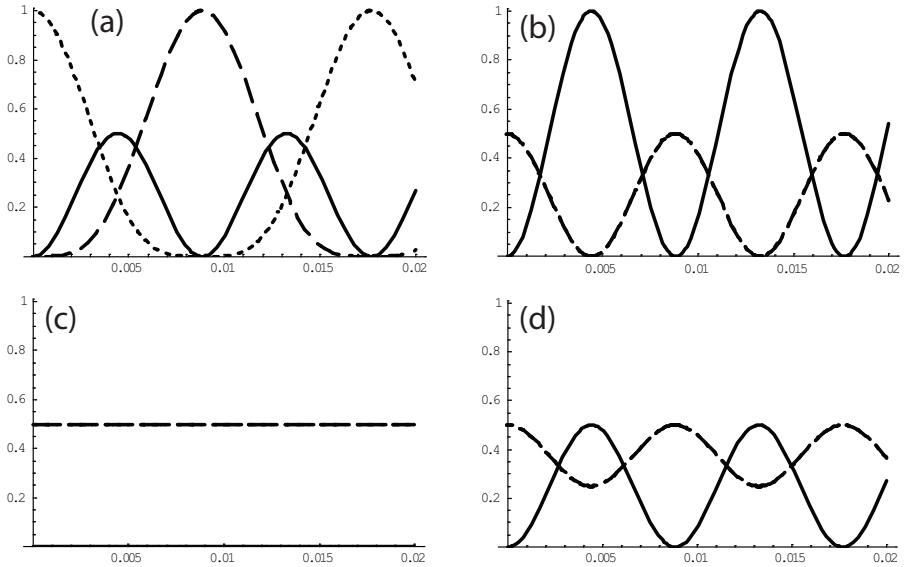

Figure A.2: State population vs. microwave time for three level systems. Dotted line corresponds to probability to be in state $|0\rangle$, dashed is for $|1\rangle$, and solid line is for $|2\rangle$. (a) Initial conditions $c_0 = 1,\ c_1 = 0,\ c_2 = 0$. (b) Initial conditions $c_0 = 1/2,\ c_1 = 1/2,\ c_2 = 0$. (c) Initial conditions $c_0 = 1/2,\ c_1 = -1/2,\ c_2 = 0$. (d) Initial conditions $c_0 = 1/2,\ c_1 = i/2,\ c_2 = 0$.

A.1 Method for Realization of Entanglement from Figure 2.1(d)

The realization for the entanglement method of Figure 2.1(d) is obtained from case 2 above, with $|0\rangle \equiv |1,-1\rangle,\ |1\rangle \equiv |1,1\rangle$, and $|2\rangle \equiv |0,0\rangle$ (Figure A.3). When the $|1,-1\rangle$ and $|1,1\rangle$ states have zero relative phase, two microwave pulses resonant with the $|1,-1\rangle \leftrightarrow |0,0\rangle$ and $|1,1\rangle \leftrightarrow |0,0\rangle$ transitions will drive these populations completely into $|0,0\rangle$ after a microwave time of $\pi/(2\sqrt{2}\Omega)$ (Figure A.2(b)).

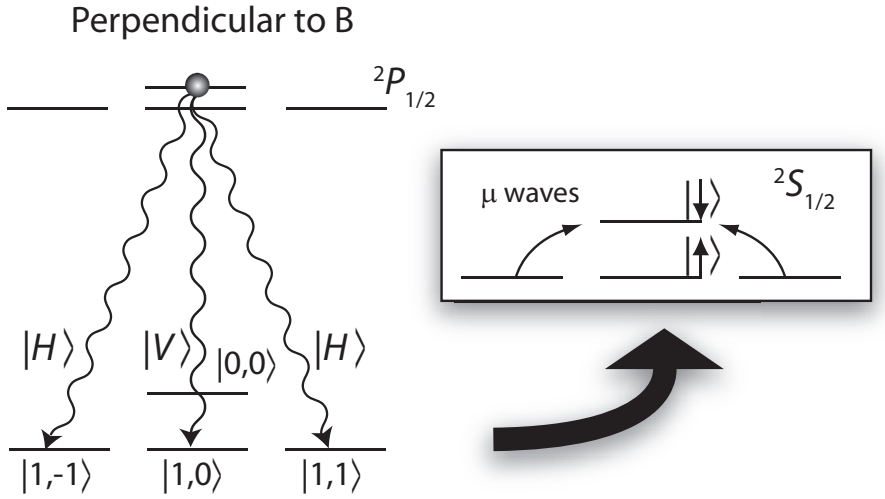

Figure A.3: Realization of entanglement method of Figure 2.1(d). When the photon is viewed perpendicularly to the quantization axis, the $\Delta m = 0$ photon decay channel is linearly polarized and orthogonal to the $\Delta m = \pm 1$ decay channels. After decay, the $|1,-1\rangle$ and $|1,1\rangle$ can be coherently combined in the $|0,0\rangle$ state establishing the atomic qubit.

A.2 Atomic Qubit Rotations in the Ion-Photon Entanglement Experiment

The importance of measuring the ion and the photon in the rotated basis, is to show that following spontaneous emission of the photon, the atom still has phase coherence between the resulting qubit states. This is done similar to Section A.1 by applying simultaneous microwave pulses between the $|1,0\rangle \leftrightarrow |0,0\rangle$ and $|1,1\rangle \leftrightarrow |0,0\rangle$ transitions with a pulse length of $\pi/(2\sqrt{2}\Omega)$. If the relative phase between the two states is equal to zero (or $(|\downarrow\rangle + |\uparrow\rangle)/\sqrt{2}$), then case 2 from above applies. However, if the relative phase is π (or $(|\uparrow\rangle - |\downarrow\rangle)/\sqrt{2}$), then case 3 applies (Figure A.4). As this phase is rotated, it rotates between cases 2 and 3 as shown in Figure 5.4(a). See also Figure A.2(b-d). The two microwave frequencies are applied by tuning the microwave source halfway between the two $|1,0\rangle \leftrightarrow |0,0\rangle$ and $|1,1\rangle \leftrightarrow |0,0\rangle$ transitions and mixing with a frequency equal to half the $|1,0\rangle \leftrightarrow |1,1\rangle$ splitting.

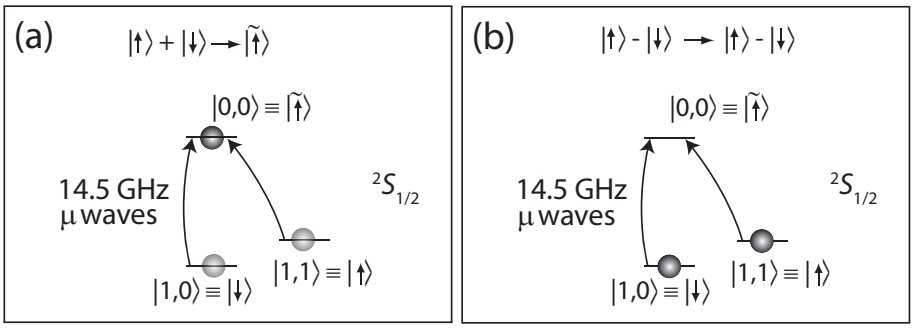

Figure A.4: Atomic qubit rotations in the ion-photon entanglement experiment. (a) With the relative phase between the two states is equal to zero, $(|\downarrow\rangle + |\uparrow\rangle)/\sqrt{2}$, then upon simultaneous microwave pulses between the $|1,0\rangle \leftrightarrow |0,0\rangle$ and $|1,1\rangle \leftrightarrow |0,0\rangle$ transitions the ion is driven to the $|0,0\rangle$ state. (b) If the relative phase between the two states is π, $(|\uparrow\rangle - |\downarrow\rangle)/\sqrt{2}$, then the atomic state remains unchanged.

A.3 Limits on Excitation Probability in the Remote-Ion Entanglement Experiment

In order to assure that at most a single photon is emitted from each ion following an excitation pulse, it is important to use a laser pulse that is much shorter than the lifetime of the excited state [151]. Here, we use a 2 ps laser pulse from a mode-locked, frequency-doubled Ti:Sapphire laser that is much shorter than the 8.1 ns excited state lifetime of the $^2P_{1/2}$ level. This near transform-limited pulse has a bandwidth of ~ 400 GHz which is not only much larger than the $^2P_{1/2}$ linewidth, but also much larger than the $^2\mathrm{S}_{1/2}$ hyperfine splitting. Hence, the σ^--polarized optical pulse that resonantly excites the $^2\mathrm{S}_{1/2}|0,0\rangle$ state to the $^2P_{1/2}|1,-1\rangle$ is also resonant with the $^2\mathrm{S}_{1/2}|1,0\rangle \leftrightarrow {}^2P_{1/2}|1,-1\rangle$ transition [65].

In this three level lambda system, the largest population which can be transfered to the $|1,-1\rangle$ state when starting from $|0,0\rangle$ is $p_e = 50\%$, with the other 50% in an equal superposition of $|0,0\rangle$ and $|1,0\rangle$. This can be seen from case 1 above with $|0\rangle \equiv {}^2\mathrm{S}_{1/2}|0,0\rangle$, $|1\rangle \equiv {}^2\mathrm{S}_{1/2}|1,0\rangle$, and $|2\rangle \equiv {}^2P_{1/2}|1,-1\rangle$, and a "rotation time" of $\pi/(2\sqrt{2}\Omega)$ (Figure A.2(a)). In principle, the excitation probability can be improved to near unity by preparing an appropriate initial superposition of $|0,0\rangle$ and $|1,0\rangle$

(cases 2 and 3 above) or by using spectral pulse-shaping techniques. Alternatively, a different excitation scheme can be adopted [167].

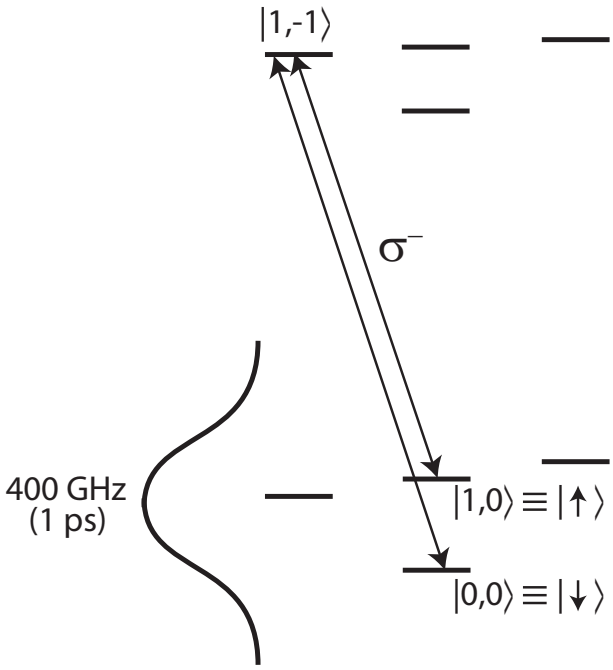

Figure A.5: Explanation for excitation probability of $p_e = 50\%$. Due to the large bandwidth of the pulsed excitation laser (~ 400 GHz) the σ^--polarized optical pulse that resonantly excites the ${}^2\mathrm{S}_{1/2}|0,0\rangle$ state to the ${}^2P_{1/2}|1,-1\rangle$ is also resonant with the ${}^2\mathrm{S}_{1/2}|1,0\rangle \leftrightarrow {}^2P_{1/2}|1,-1\rangle$ transition.

APPENDIX B

Ytterbium and Cadmium Ion Resonant Wavelengths

Listed below are the resonant wavelengths of the ytterbium and cadmium ions that we have measured (Figure B.1). These numbers are obtained from our Burleigh WA-1500 Wavemeter. The wavelengths are not accurate to the fourth decimal, but are precise to a given adjustment of the Wavemeter.

Isotope	Abundance	739 nm	935 nm	638 nm	864 nm	399 nm
170	3.1%	739.0474	935.1983			
171	14.3%	739.0521	935.1878	638.6101/638.6151		398.9118
172	21.9%	739.0489	935.1875		864.8375	398.9116
174	31.8%	739.0500	935.1800	638.6187	864.8426	398.9113
176	12.7%	739.0512	935.1725			398.9111

Table B.1: Resonant wavelengths for ytterbium ions, as measured in our lab.

Isotope	Abundance	858 nm
106	1.25%	858.0272
108	0.89%	858.0278
110	12.49%	858.0283
111	12.80%	858.0261
112	24.13%	858.0288
113	12.22%	858.0265
114	28.73%	858.0292
116	7.49%	858.0295

Table B.2: Resonant wavelengths for cadmium ions, as measured in our lab.

In addition to the wavelengths listed above, one further transition was driven in the cadmium ion. Following the measurement of the excited state lifetimes in cadmium using the ultrafast laser [95], we briefly explored the possibility of measuring

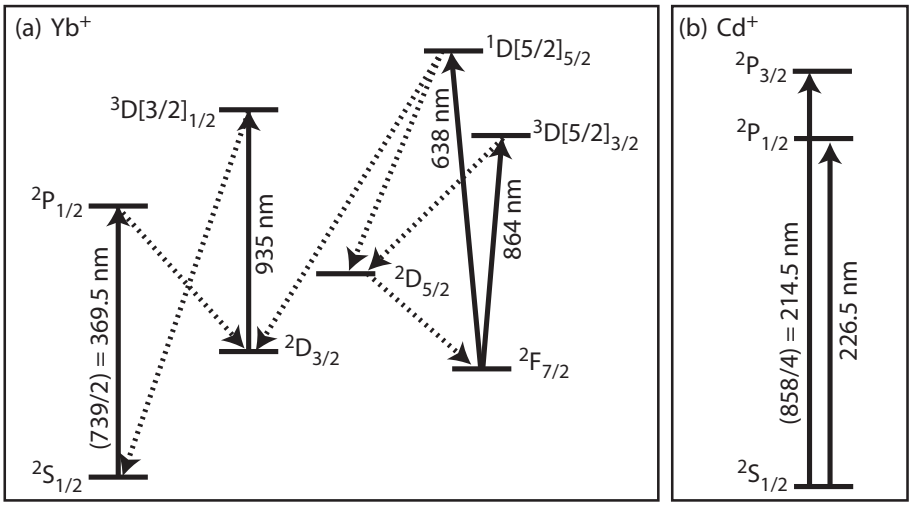

Figure B.1: Energy levels for Ytterbium and Cadmium. (a) Ytterbium. (b) Cadmium.

Element	10^{-8}	10^{-7}	10^{-6}	10^{-5}	10^{-4}
Yb	247	279	317	365	417
Cd	155	181	209	242	280

Table B.3: Vapor pressures for ytterbium and cadmium atoms. The required temperature for each partial pressure is listed in degrees Celsius

high excited states. One candidate was the $4d^{10}5d\ ^2D_{5/2}$ level 231.35 nm above the $^2P_{3/2}$ level (Figure B.2). This state was prepared by driving the ion to the $^2P_{3/2}$ level with the cw laser and further exciting the ion to $4d^{10}5d\ ^2D_{5/2}$ with the pulsed laser. Confirmation of the excitation to this level was provided by adjusting the triplet imaging lens and imaging the 231 nm scattered photons on the camera (by moving the imaging lens further away from the ion by $\approx 490\ \mu$m with respect to the 214.5 nm imaging position as discussed in Section 4.4). A lifetime measurement was not taken on this transition, however, because it was found that when driving ions to this state, they became doubly ionized (Cd^{2+}) because a further excitation with the 214.5 nm laser pulse will drive the ion directly to the continuum at 136374.74 cm^{-1}. This was directly confirmed on the camera by imaging three ions, whereby the outer two ions were pushed further apart upon double ionization of the middle ion (which became dark), due to the Coulomb repulsion.

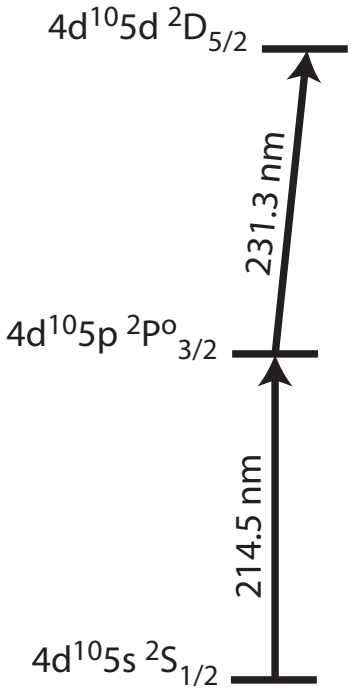

Figure B.2: Excitation to $4d^{10}5d\ ^2D_{5/2}$ level in Cd^+. The ion is driven to the $4d^{10}5p\ ^2P^o_{3/2}$ with the 214.5 nm cw laser and further excited to the $4d^{10}5d\ ^2D_{5/2}$ level with the pulsed laser tuned to 231.35 nm.

APPENDIX C

Fidelity and Entanglement of Formation

C.1 Fidelity Estimation for the Ion-Photon Experiment

The entanglement fidelity of an arbitrary two-qubit quantum state can be written as its overlap with an appropriate maximally entangled two-qubit state [168]. In the atom-photon entanglement experiment from Chapter V, the two qubits are represented by a 4×4 density matrix ρ with photon and atomic basis states $|\downarrow\rangle|H\rangle$, $|\uparrow\rangle|H\rangle$, $|\downarrow\rangle|V\rangle$, and $|\uparrow\rangle|V\rangle$. The entanglement fidelity with respect to the particular maximally entangled state $|\Psi_{ME}\rangle = \frac{1}{\sqrt{2}}(|\downarrow\rangle|H\rangle + |\uparrow\rangle|V\rangle)$ is given by:

$$\mathscr{F} = \langle\Psi_{ME}|\rho|\Psi_{ME}\rangle = \frac{1}{2}(\rho_{\downarrow H,\downarrow H} + \rho_{\uparrow V,\uparrow V} + \rho_{\downarrow H,\uparrow V} + \rho_{\uparrow V,\downarrow H}), \tag{C.1}$$

where $\rho_{\Pi S,\Pi' S'} = \langle \Pi S|\rho|\Pi' S'\rangle$ with $\Pi = H$ or V and $S = \downarrow$ or $\uparrow$. (This expression also holds for any maximally entangled target state by appropriately redefining the basis states.) The first two terms in this expression are the measured correlation probabilities of detecting state $|H\rangle$ with $|\downarrow\rangle$ and state $|V\rangle$ with $|\uparrow\rangle$. The last two coherence terms can be determined by repeating the experiment while independently rotating each qubit through a polar angle of $\pi/2$ in the Bloch sphere before measurement. The rotated quantum state is then given by $\tilde{\rho} = R_{\pi/2}(\phi)\rho R^{\dagger}_{\pi/2}(\phi)$ where $R_{\pi/2}(\phi)$ is

a $\pi/2$ polar rotation operator for both qubits with relative phase ϕ. We find that:

$$\begin{aligned} &\mathrm{e}^{-i\phi}\rho_{\downarrow H,\uparrow V} + \mathrm{e}^{i\phi}\rho_{\uparrow V,\downarrow H} \\ &\quad = \tilde{\rho}_{\downarrow H,\downarrow H} + \tilde{\rho}_{\uparrow V,\uparrow V} - \tilde{\rho}_{\uparrow H,\uparrow H} - \tilde{\rho}_{\downarrow V,\downarrow V} - (\mathrm{e}^{-i\phi}\rho_{\downarrow V,\uparrow H} + \mathrm{e}^{i\phi}\rho_{\uparrow H,\downarrow V}) \\ &\quad \geq \tilde{\rho}_{\downarrow H,\downarrow H} + \tilde{\rho}_{\uparrow V,\uparrow V} - \tilde{\rho}_{\uparrow H,\uparrow H} - \tilde{\rho}_{\downarrow V,\downarrow V} - 2\sqrt{\rho_{\uparrow H,\uparrow H}\rho_{\downarrow V,\downarrow V}} \end{aligned} \quad \text{(C.2)}$$

so that a lower bound on the entanglement fidelity can be expressed in terms of diagonal density matrix elements in the original and rotated basis (with ϕ set to zero):

$$\mathscr{F} \geq \frac{1}{2}(\rho_{\downarrow H,\downarrow H} + \rho_{\uparrow V,\uparrow V} - 2\sqrt{\rho_{\uparrow H,\uparrow H}\rho_{\downarrow V,\downarrow V}} + \tilde{\rho}_{\downarrow H,\downarrow H} + \tilde{\rho}_{\uparrow V,\uparrow V} - \tilde{\rho}_{\uparrow H,\uparrow H} - \tilde{\rho}_{\downarrow V,\downarrow V}). \quad \text{(C.3)}$$

These diagonals are expressed in terms of the measured probabilities as:

$$\rho_{\Pi S,\Pi S} = P(S|\Pi)P(\Pi) \text{ and } \tilde{\rho}_{\Pi S,\Pi S} = \tilde{P}(S|\Pi)\tilde{P}(\Pi). \quad \text{(C.4)}$$

For fidelities $\mathscr{F} > 0.5$, the underlying quantum state is entangled [27].

C.2 Fidelity and Entanglement of Formation for the Ion-Ion Experiment

Since the desired resulting entangled state is $|\Psi^-\rangle_{\text{atom}} = (|\uparrow\rangle_a|\downarrow\rangle_b - |\downarrow\rangle_a|\uparrow\rangle_b)/\sqrt{2}$, the calculated fidelity is $\mathscr{F} = (\rho_{\downarrow\uparrow,\downarrow\uparrow} + \rho_{\uparrow\downarrow,\uparrow\downarrow})/2 + |\rho_{\downarrow\uparrow,\uparrow\downarrow}|$, where $\rho_{ij,kl} = \langle ij|\rho|kl\rangle$ and $i,j,k,l \in (\uparrow,\downarrow)$. The unrotated basis measurements yield $\rho_{\downarrow\downarrow,\downarrow\downarrow}$, $\rho_{\downarrow\uparrow,\downarrow\uparrow}$, $\rho_{\uparrow\downarrow,\uparrow\downarrow}$, and $\rho_{\uparrow\uparrow,\uparrow\uparrow}$ directly. The rotated basis measurements yield $\tilde{\rho}_{\downarrow\downarrow,\downarrow\downarrow}$, $\tilde{\rho}_{\downarrow\uparrow,\downarrow\uparrow}$, $\tilde{\rho}_{\uparrow\downarrow,\uparrow\downarrow}$, and $\tilde{\rho}_{\uparrow\uparrow,\uparrow\uparrow}$, where $\tilde{\rho}_{ij,kl}$ corresponds to the density matrix elements after the applied microwave $\pi/2$ rotations with phase ϕ_a and ϕ_b on the two ions. We find

$$\tilde{\rho}_{\downarrow\downarrow,\downarrow\downarrow} + \tilde{\rho}_{\uparrow\uparrow,\uparrow\uparrow} - \tilde{\rho}_{\downarrow\uparrow,\downarrow\uparrow} - \tilde{\rho}_{\uparrow\downarrow,\uparrow\downarrow} = 2\,|\rho_{\downarrow\uparrow,\uparrow\downarrow}|\cos(\phi_a - \phi_b) + 2\,|\rho_{\downarrow\downarrow,\uparrow\uparrow}|\cos(\phi_a + \phi_b). \quad \text{(C.5)}$$

In the experiment, we control the relative phase $\Delta\phi = \phi_b - \phi_a$ between the microwave pulse on each ion, but have no control over the absolute phase of the applied microwaves. Therefore, the measured contrast in the rotated basis measurement comes

entirely from the $\rho_{\downarrow\uparrow,\uparrow\downarrow}$ term, with a resulting fidelity: $\mathscr{F} = (\rho_{\downarrow\uparrow,\downarrow\uparrow} + \rho_{\uparrow\downarrow,\uparrow\downarrow} + C)/2 = 0.63 \pm 0.03$, where C is the contrast of the oscillations in Figure 9.4.

A lower bound on the entanglement of formation can be calculated by suppressing the unobserved single-qubit coherences (e.g., $\rho_{\downarrow\downarrow,\downarrow\uparrow}$ or $\rho_{\uparrow\downarrow,\uparrow\uparrow}$), which cannot increase the entanglement. The resulting density matrix can then be expressed as

$$\begin{array}{c} \\ |\downarrow\rangle_a|\downarrow\rangle_b \\ |\downarrow\rangle_a|\uparrow\rangle_b \\ |\uparrow\rangle_a|\downarrow\rangle_b \\ |\uparrow\rangle_a|\uparrow\rangle_b \end{array} \begin{array}{c} \begin{array}{cccc} |\downarrow\rangle_a|\downarrow\rangle_b & |\downarrow\rangle_a|\uparrow\rangle_b & |\uparrow\rangle_a|\downarrow\rangle_b & |\uparrow\rangle_a|\uparrow\rangle_b \end{array} \\ \begin{pmatrix} 0.11 & 0 & 0 & \rho_{\downarrow\downarrow,\uparrow\uparrow} \\ 0 & 0.38 & 0.235 & 0 \\ 0 & 0.235 & 0.40 & 0 \\ \rho_{\uparrow\uparrow,\downarrow\downarrow} & 0 & 0 & 0.11 \end{pmatrix} \end{array}. \tag{C.6}$$

From this, the lower bound is numerically calculated using the procedure outlined in references [168, 169] resulting in a concurrence of $\mathscr{C} \geq 0.25 \pm 0.04$ and an entanglement of formation of $\mathscr{E} \geq 0.12 \pm 0.03$.

APPENDIX D

Phase of Entangled State.

When considering all phases, the quantum state of the system before interference on the beam splitter is:

$$\frac{1}{2}[(e^{-i\omega_\uparrow t}\,|\uparrow\rangle_a\, e^{ik_{\nu_\uparrow}x_a - i\omega_{\nu_\uparrow}t}|\nu_\uparrow\rangle_a - e^{-i\omega_\downarrow t}\,|\downarrow\rangle_a\, e^{ik_{\nu_\downarrow}x_a - i\omega_{\nu_\downarrow}t}|\nu_\downarrow\rangle_a) \otimes$$
$$(e^{-i\omega_\uparrow t}\,|\uparrow\rangle_b\, e^{ik_{\nu_\uparrow}x_b - i\omega_{\nu_\uparrow}t}|\nu_\uparrow\rangle_b - e^{-i\omega_\downarrow t}\,|\downarrow\rangle_b\, e^{ik_{\nu_\downarrow}x_b - i\omega_{\nu_\downarrow}t}|\nu_\downarrow\rangle_b)], \tag{D.1}$$

where $\hbar(\omega_\uparrow - \omega_\downarrow)$ and $\hbar(\omega_{\nu_\uparrow} - \omega_{\nu_\downarrow})$ are the energy differences between the two atomic and photonic qubit states, respectively, and x_i is the photon path length from the ith ion to the beam splitter. However, since $\omega_\uparrow + \omega_{\nu_\uparrow} = \omega_\downarrow + \omega_{\nu_\downarrow}$, the equation can be rewritten as:

$$\frac{1}{2}[(e^{ik_{\nu_\uparrow}x_a}\,|\uparrow\rangle_a\,|\nu_\uparrow\rangle_a - e^{ik_{\nu_\downarrow}x_a}\,|\downarrow\rangle_a\,|\nu_\downarrow\rangle_a) \otimes (e^{ik_{\nu_\uparrow}x_b}\,|\uparrow\rangle_b\,|\nu_\uparrow\rangle_b - e^{ik_{\nu_\downarrow}x_b}\,|\downarrow\rangle_b\,|\nu_\downarrow\rangle_b)]. \tag{D.2}$$

The two photons emerge from the beam splitter along separate paths only if they are in the antisymmetric state $|\Psi^-\rangle_{\text{photon}} = (|\nu_\uparrow\rangle_a|\nu_\downarrow\rangle_b - |\nu_\downarrow\rangle_a|\nu_\uparrow\rangle_b)/\sqrt{2}$. Therefore, the ions are projected onto:

$$\frac{1}{\sqrt{2}}(-\,|\uparrow\rangle_a\,|\downarrow\rangle_b + e^{-i\Delta k\Delta x}\,|\downarrow\rangle_a\,|\uparrow\rangle_b), \tag{D.3}$$

where $\Delta k \equiv k_{\nu_\uparrow} - k_{\nu_\downarrow}$ and $\Delta x \equiv x_a - x_b$. It is important to note that the entanglement is insensitive to fluctuations in the path length at the scale of the optical

wavelength [116, 54]. The relative phase appearing in the entangled state of Equation D.3 is only sensitive to path length fluctuations compared to the wavelength associated with the frequency difference of the photonic and atomic qubit states $2\pi/\Delta k = c/(\omega_{\nu_\downarrow} - \omega_{\nu_\uparrow}) = 2.4$ cm. Stability over this scale is easily achieved.

While this stability is passively achieved, the path lengths can be changed. The data reported in Chapter IX was taken with a single fixed value for $\Delta k \Delta x$. The experimental results for this choice of $\Delta k \Delta x$ is repeated below in Figure D.1. However, following this data set, the path length of one ion x_a was increased by ~ 0.5mm. A complete set of rotated data was again taken with this setting for $\Delta k \Delta x$ and is shown in Figure D.2. As can be seen from this data set, the phase of the resulting entangled state has changed by ≈ 1.1 radians, consistent with the change of x_a.

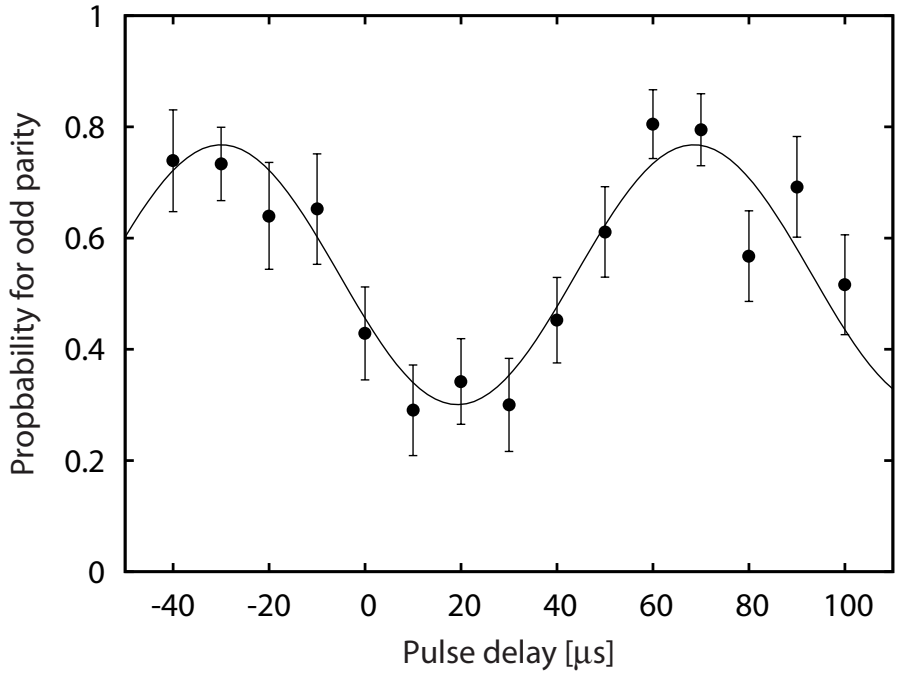

Figure D.1: Measured probabilities in the rotated basis: first choice of $\Delta k \Delta x$ — Results repeated from Figure 9.4. The absolute phase of the interference pattern depends on two factors: the difference in microwave transmission lines to each ion and the photon path length difference from each ion to the beam splitter $\Delta k \Delta x$. The fitted curve has a phase offset of $-30 \pm 1.8\mu$s, contrast of $C = 0.47 \pm 0.05$, and vertical offset of 0.30 ± 0.03.

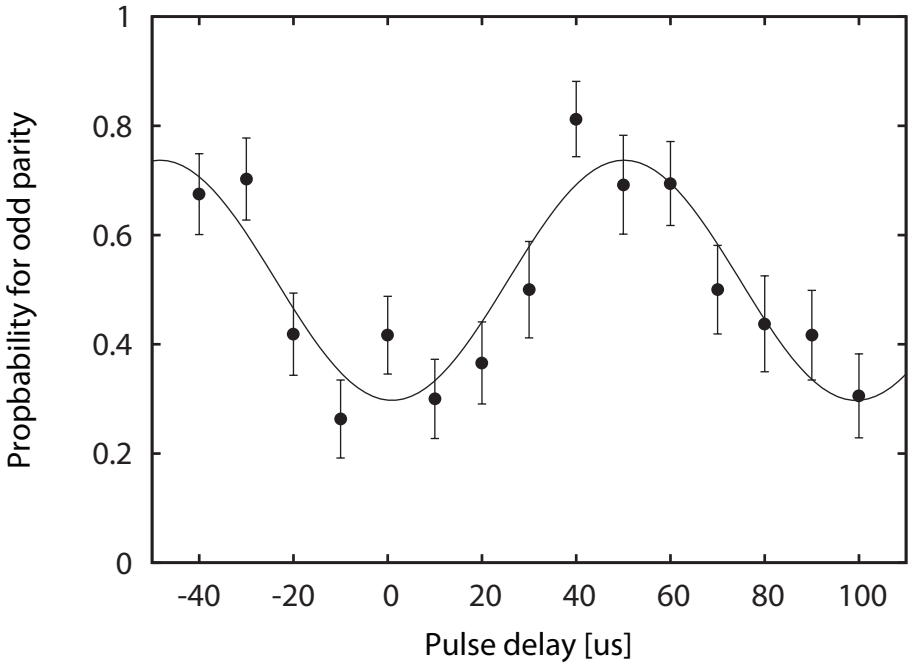

Figure D.2: Measured probabilities in the rotated basis: second choice of $\Delta k \Delta x$. The absolute phase of the interference is shifted with respect to Figure D.1. This is due to a change in $\Delta k \Delta x$ by changing x_a by ~ 0.5mm. This new fitted curve has a phase offset of $-48 \pm 2.3\mu$s, contrast of $C = 0.44 \pm 0.06$, and vertical offset of 0.30 ± 0.03. This phase offset is different from that of Figure D.1 by 18 μs corresponding to ≈ 1.1 radians, consistent with the change of x_a

APPENDIX E

Cd^+ Interactions with Intense Nanosecond Laser Pulses

In one of the first experiments in our trapped cadmium ion system, the possibility of state-dependent forces with fast laser pulses was investigated [170]. In these experiments, a frequency-quadrupled QuantaRay DCR-2 Q-switched Nd:YAG laser provided the fast laser pulses at 266 nm (fundamental wavelength of 1064 nm). This 10 Hz laser provided ≈ 60 mJ of laser power at 266 nm with an estimated pulse length of 6 ns. While this laser is significantly detuned from the atomic $^2S_{1/2} \leftrightarrow {}^2P_{1/2}$ and $^2S_{1/2} \leftrightarrow {}^2P_{3/2}$ transitions in cadmium, the high intensity pulses still allowed for a large a.c. Stark shift on the atomic ground states and through the interaction with the optical potential, could allow for a state-dependent force on the ion (Figure E.1). In the end, we were not able to detect the effects of the a.c. Stark shift because it was found that the bandwidth of the laser pulses was large compared to the 14.5 GHz hyperfine splitting. This large bandwidth allowed for stimulated Raman transitions between the hyperfine levels which washed out any signal we may have been able to detect from the state-dependent force (Figure E.2).

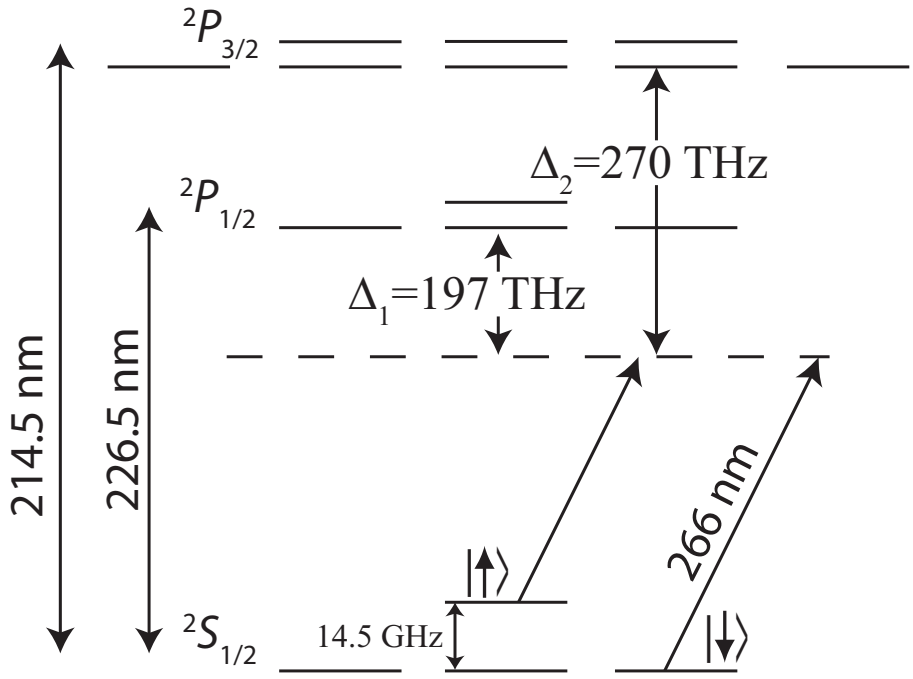

Figure E.1: Relevant energy levels and excitation scheme for the state dependent force experiments using 266 nm laser radiation.

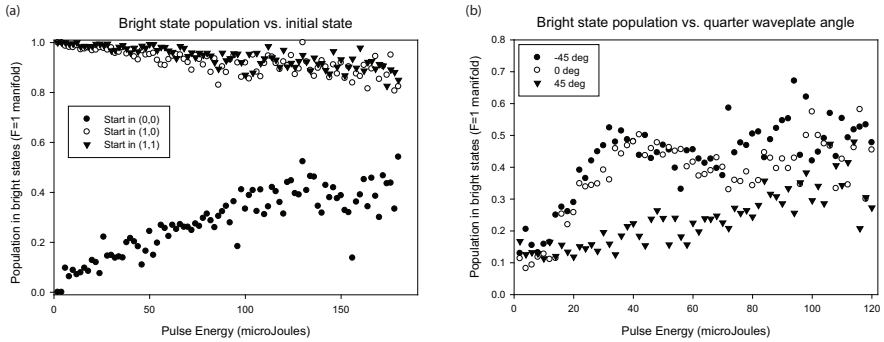

Figure E.2: Nanosecond Raman transitions. (a) Bright state population ($F = 1$ manifold) as a function of nanosecond pulse energy. (b) Bright state population vs. pulse energy for different laser polarizations.

BIBLIOGRAPHY

BIBLIOGRAPHY

[1] A. Einstein, B. Podolsky, and N. Rosen. Can quantum-mechanical description of physical reality be considered complete? *Phys. Rev.*, 47:777–780, 1935.

[2] J. S. Bell. On the Einstein-Podolsky-Rosen paradox. *Physics*, 1:195–200, 1965.

[3] J. S. Bell. On the problem of hidden variables in quantum mechanics. *Rev. of Mod. Phys.*, 38:447–452, 1967.

[4] J. F. Clauser, M. A. Horne, A. Shimony, and R. A. Holt. Proposed experiment to test local hidden-variable theories. *Phys. Rev. Lett.*, 23:880–884, 1969.

[5] S. J. Freedman and J. F. Clauser. Experimental test of local hidden-variable theories. *Phys. Rev. Lett.*, 28:938–941, 1972.

[6] A. Aspect, P. Grangier, and G. Roger. Experimental realization of Einstein-Podolsky-Rosen-Bohm *Gedankenexperiment*: A new violation of Bell's inequalities. *Phys. Rev. Lett.*, 49:91–94, 1982.

[7] A. Aspect, J. Dalibard, and G. Roger. Experimental test of Bell's inequalities using time-varying analyzers. *Phys. Rev. Lett.*, 49:1804–1807, 1982.

[8] Z. Y. Ou and L. Mandel. Violation of Bell's inequality and classical probability in a two-photon correlation experiment. *Phys. Rev. Lett.*, 61:50–53, 1988.

[9] G. Weihs, T. Jennewein, C. Simon, H. Weinfurter, and A. Zeilinger. Violation of Bell's inequality under strict Einstein locality conditions. *Phys. Rev. Lett.*, 81:5039–5043, 1998.

[10] M. Lamehi-Rachti and W. Mittig. Quantum mechanics and hidden variables: A test of Bell's inequality by the measurement of the spin correlation in low-energy proton-proton scattering. *Phys. Rev. D*, 14:2543–2555, 1976.

[11] A. Bramon and M. Nowakowski. Bell inequalities for entangled pairs of neutral kaons. *Phys. Rev. Lett.*, 83:1–5, 1999.

[12] M. A. Rowe, D. Kielpinski, V. Meyer, C. A. Sackett, W. M. Itano, C. Monroe, and D. J. Wineland. Experimental violation of a Bell's inequality with efficient detection. *Nature*, 409:791–794, 2001.

[13] C. F. Roos, G. P. T. Lancaster, M. Riebe, H. Häffner, W. Hänsel, S. Gulde, C. Becher, J. Eschner, F. Schmidt-Kaler, and R. Blatt. Bell states of atoms with ultralong lifetimes and their tomographic state analysis. *Phys. Rev. Lett.*, 92:220402, 2004.

[14] Y. Hasegawa, R. Loidl, G. Badurek, M. Barron, and H. Rauch. Violation of a Bell-like inequality in single-neutron interferometry. *Nature*, 425:45–48, 2003.

[15] D. L. Moehring, M. J. Madsen, B. B. Blinov, and C. Monroe. Experimental bell inequality violation with an atom and a photon. *Phys. Rev. Lett.*, 93:090410, 2004.

[16] D. N. Matsukevich, T. Chanelière, M. Bhattacharya, S.-Y. Lan, S. D. Jenkins, T. A. B. Kennedy, and A. Kuzmich. Entanglement of a photon and a collective atomic excitation. *Phys. Rev. Lett.*, 95:040405, 2005.

[17] D. N. Matsukevich, T. Chaneliere, S. D. Jenkins, S.-Y. Lan, T. A. B. Kennedy, and A. Kuzmich. Entanglement of remote atomic qubits. *Phys. Rev. Lett.*, 96(3):030405, 2006.

[18] J. Volz, M. Weber, D. Schlenk, W. Rosenfeld, J. Vrana, K. Saucke, C. Kurtsiefer, and H. Weinfurter. Observation of entanglement of a single photon with a trapped atom. *Phys. Rev. Lett.*, 96:030404, 2006.

[19] C. Monroe. Quantum information processing with atoms and photons. *Nature*, 416:238–246, 2002.

[20] J.I. Cirac and P. Zoller. New frontiers in quantum information with atoms and ions. *Physics Today*, 57:38–45, 2004.

[21] P. Zoller, Th. Beth, D. Binosi, R. Blatt, H. Briegel, D. Bruss, T. Calarco, J.I. Cirac, D. Deutsch, J. Eisert, A. Ekert, C. Fabre, N. Gisin, P. Grangiere, M. Grass, S. Haroche, A. Imamoglu, A. Karlson, J. Kempe, L. Kouwenhoven, S. Krll, G. Leuchs, M. Lewenstein, D. Loss, N. Ltkenhaus, S. Massar, J.E. Mooij, M.B. Plenio, E. Polzik, S. Popescu, G. Rempe, A. Sergienko, D. Suter, J. Twamley, G. Wendin, R. Werner, A. Winter, J. Wrachtrup, and A. Zeilinger. Quantum information processing and communication. *Eur. Phys. J. D*, 36:203–228, 2005.

[22] J. I. Cirac and P. Zoller. Quantum computation with cold trapped ions. *Phys. Rev. Lett.*, 74:4091–4094, 1995.

[23] C. Monroe, D. M. Meekhof, B. E. King, W. M. Itano, and D. J. Wineland. Demonstration of a fundamental quantum logic gate. *Phys. Rev. Lett.*, 75:4714–4717, 1995.

[24] A. Sørensen and K. Mølmer. Quantum computation with ions in thermal motion. *Phys. Rev. Lett.*, 82:1971–1975, 1999.

[25] D. Jaksch, H.-J. Briegel, J. I. Cirac, C. W. Gardiner, and P. Zoller. Entanglement of atoms via cold controlled collisions. *Phys. Rev. Lett.*, 82:1975–1978, 1999.

[26] D. Jaksch, J. I. Cirac, P. Zoller, S. L. Rolston, R. Côté, and M. D. Lukin. Fast quantum gates for neutral atoms. *Phys. Rev. Lett.*, 85:2208–2211, 2000.

[27] C. A. Sackett, D. Kielpinski, B. E. King, C. Langer, V. Meyer, C. J. Myatt, M. Rowe, Q. A. Turchette, W. M. Itano, D. J. Wineland, and C. Monroe. Experimental entanglement of four particles. *Nature*, 404:256–259, 2000.

[28] G. J. Milburn, S. Schneider, and D. F. V. James. Ion trap quantum computing with warm ions. *Fortschr. Phys.*, 48:801–810, 2000.

[29] A. Sørensen and K. Mølmer. Entanglement and quantum computation with ions in thermal motion. *Phys. Rev. A*, 62:022311, 2000.

[30] D. Jonathan, M. B. Plenio, and P. L. Knight. Fast quantum gates for cold trapped ions. *Phys. Rev. A*, 62:042307, 2000.

[31] J. L. Cirac and P. Zoller. A scalable quantum computer with ions in an array of microtraps. *Nature*, 404:579–581, 2000.

[32] C. J. Hood, T. W. Lynn, A. C. Doherty, A. S. Parkins, and H. J. Kimble. The atom-cavity microscope: Single atoms bound in orbit by single photons. *Science*, 287:1447 – 1453, 2000.

[33] P. W. H. Pinkse, T. Fischer, P. Maunz, and G. Rempe. Trapping an atom with single photons. *Nature*, 404:365–368, 2000.

[34] L.-M. Duan, J. I. Cirac, and P. Zoller. Geometric manipulation of trapped ions for quantum computation. *Science*, 292:1695–1697, 2000.

[35] I. H. Deutsch, G. K. Brennen, and P. S. Jessen. Quantum computing with neutral atoms in an optical lattice. *Fortschr. Phys.*, 48:925–943, 2000.

[36] G. R. Guthöhrlein, M. Keller, K. Hayasaka, W. Lange, and H. Walther. A single ion as a nanoscopic probe of an optical field. *Nature*, 414:49–51, 2001.

[37] D. Leibfried, B. DeMarco, V. Meyer, D. Lucas, M. Barrett, J. Britton, W. M. Itano, B. Jelenkovi, C. Langer, T. Rosenband, and D. J. Wineland. Experimental demonstration of a robust, high-fidelity geometric two ion-qubit phase gate. *Nature*, 422:412–415, 2003.

[38] J. J. García-Ripoll, P. Zoller, and J. I. Cirac. Speed optimized two-qubit gates with laser coherent control techniques for ion trap quantum computing. *Phys. Rev. Lett.*, 91:157901, 2003.

[39] F. Schmidt-Kaler, H. Häffner, M. Riebe, S. Gulde, G. P. T. Lancaster, T. Deuschle, C. Becher, C. F. Roos, J. Eschner, and R. Blatt. Realization of the Cirac-Zoller controlled-NOT quantum gate. *Nature*, 422:408–411, 2003.

[40] J. McKeever, A. Boca, A. D. Boozer, R. Miller, J. R. Buck, A. Kuzmich, and H. J. Kimble. Deterministic generation of single photons from one atom trapped in a cavity. *Science*, 303:1992–1994, 2004.

[41] L.-M. Duan. Scaling ion trap quantum computation through fast quantum gates. *Phys. Rev. Lett.*, 93:100502, 2004.

[42] D. Kielpinski, C. Monroe, and D.J. Wineland. Architecture for a large-scale ion-trap quantum computer. *Nature*, 417:709–711, 2002.

[43] M. A. Rowe, A. Ben-Kish, B. DeMarco, D. Leibfried, V. Meyer, J. Beall, J. Britton, J. Hughes, W. M. Itano, B. Jelenković, C. Langer, T. Rosenband, and D. J. Wineland. Transport of quantum states and separation of ions in a dual rf ion trap. *Quant. Inf. Comp.*, 2:257–271, 2002.

[44] W. K. Hensinger, S. Olmschenk, D. Stick, D. Hucul, M. Yeo, M. Acton, L. Deslauriers, C. Monroe, and J. Rabchuk. T-junction ion trap array for two-dimensional ion shuttling, storage and manipulation. *Appl. Phys. Lett.*, 88:034101, 2006.

[45] D. Stick, W. K. Hensinger, S. Olmschenk, M. J. Madsen, K. Schwab, , and C. Monroe. Ion trap in a semiconductor chip. *Nature Physics*, 2:36–39, 2006.

[46] L. Deslauriers, S. Olmschenk, D. Stick, W. K. Hensinger, J. Sterk, and C. Monroe. Scaling and suppression of anomalous heating in ion traps. *Phys. Rev. Lett.*, 97(10):103007, 2006.

[47] L.-M. Duan and R. Raussendorf. Efficient quantum computation with probabilistic quantum gates. *Phys. Rev. Lett.*, 95:080503, 2005.

[48] Sean D. Barrett and Pieter Kok. Efficient high-fidelity quantum computation using matter qubits and linear optics. *Physical Review A (Atomic, Molecular, and Optical Physics)*, 71(6):060310, 2005.

[49] L.-M. Duan, M. J. Madsen, D. L. Moehring, P. Maunz, Jr. R. N. Kohn, and C. Monroe. Probabilistic quantum gates between remote atoms through interference of optical frequency qubits. *Phys. Rev. A*, 76:062324, 2006.

[50] J. I. Cirac, P. Zoller, H. J. Kimble, and H. Mabuchi. Quantum state transfer and entanglement distribution among distant nodes in a quantum network. *Phys. Rev. Lett.*, 78:3221–3224, 1997.

[51] J. J. Bollinger, D. J. Heinzen, W. M. Itano, S. L. Gilbert, and D. J. Wineland. A 303 MHz frequency standard based on trapped Be^+ ions. *IEEE Trans. Inst. Meas.*, 40:126–128, 1991.

[52] C. Langer, R. Ozeri, J. D. Jost, J. Chiaverini, B. DeMarco, A. Ben-Kish, R. B. Blakestad, J. Britton, D. B. Hume, W. M. Itano, D. Leibfried, R. Reichle, T. Rosenband, T. Schaetz, P. O. Schmidt, and D. J. Wineland. Long-lived qubit memory using atomic ions. *Phys. Rev. Lett.*, 95:060502, 2005.

[53] H. Häffner, F. Schmidt-Kaler, W. Hänsel, C. F. Roos, T. Körber, M. Chwalla, M. Riebe, J. Benhelm, U. D. Rapol, C. Becher, and R. Blatt. Robust entanglement. *Appl. Phys. B*, 81:151–153, 2005.

[54] C. Simon and W. T. M. Irvine. Robust long-distance entanglement and a loophole-free Bell test with ions and photons. *Phys. Rev. Lett.*, 91:110405, 2003.

[55] B. B. Blinov, D. Leibfried, C. Monroe, and D. J. Wineland. Quantum computing with trapped ion hyperfine qubits. *Quantum Inf. Proc.*, 3:45–59, 2004.

[56] P. Badziąg, M. Horodecki, P. Horodecki, and R. Horodecki. Local environment can enhance fidelity of quantum teleportation. *Phys. Rev. A*, 62:012311, 2000.

[57] S.-Y. Lan, S. D. Jenkins, T. Chaneliere, D. N. Matsukevich, C. J. Campbell, R. Zhao, T. A. B. Kennedy, and A. Kuzmich. Dual-species matter qubit entangled with light. *Phys. Rev. Lett.*, 98(12):123602, 2007.

[58] D. Stucki, N. Gisin, O. Guinnard, G. Ribordy, and H. Zbinden. Quantum key distribution over 67 km with a plug & play system. *New J. Phys.*, 4:41, 2002.

[59] D. S. Bethune and W. P. Risk. Autocompensating quantum cryptography. *New J. Phys.*, 4:42, 2002.

[60] R. J. Hughes, J. E. Nordholt, D. Derkacs, and C. G. Peterson. Practical free-space quantum key distribution over 10 km in daylight and at night. *New J. Phys.*, 4:43, 2002.

[61] N. Lütkenhaus and M. Jahma. Quantum key distribution with realistic states: photon-number statistics in the photon-number splitting attack. *New J. Phys.*, 4:44, 2002.

[62] D. G. Enzer, P. G. Hadley, R. J. Hughes, C. G. Peterson, and P. G. Kwiat. Entangled-photon six-state quantum cryptography. *New J. Phys.*, 4:45, 2002.

[63] C. Elliott. Building the quantum network. *New J. Phys.*, 4:46, 2002.

[64] J. H. Shapiro. Architectures for long-distance quantum teleportation. *New J. Phys.*, 4:47, 2002.

[65] M. J. Madsen, D. L. Moehring, P. Maunz, Jr. R. N. Kohn, L.-M. Duan, and C. Monroe. Ultrafast coherent excitation of a trapped ion qubit for fast gates and photon frequency qubits. *Phys. Rev. Lett.*, 97(4):040505, 2006.

[66] A.B. Mundt, A. Kreuter, C. Becher, D. Leibfried, J. Eschner, F. Schmidt-Kaler, and R. Blatt. Coupling a single atomic quantum bit to a high finesse optical cavity. *Phys. Rev. Lett.*, 89:103001, 2002.

[67] A. Kuhn, M. Hennrich, and G. Rempe. Deterministic single-photon source for distributed quantum networking. *Phys. Rev. Lett.*, 89:067901, 2002.

[68] P. G. Kwiat, A. M. Steinberg, R. Y. Chiao, P. Eberhard, and M. Petroff. High efficiency single-photon detectors. *Phys. Rev. A*, 48:R867–R870, 1993.

[69] A. P. VanDevender and P. G. Kwiat. High efficiency single photon detection via frequency up-conversion. *J. of Mod. Opt.*, 51:1433–1445, 2004.

[70] D. Rosenberg, A. E. Lita, A. J. Miller, and S. W. Nam. Noise-free high-efficiency photon-number-resolving detectors. *Phys. Rev. A*, 71:061803, 2005.

[71] D. Leibfried, E. Knill, S. Seidelin, J. Britton, R. B. Blakestad, J. Chiaverini, D. B. Hume, W. M. Itano, J. D. Jost, C. Langer, R. Ozeri, R. Reichle, and D. J. Wineland. Creation of a six-atom "Schrödinger cat" state. *Nature*, 438:639–642, 2005.

[72] H. Häffner, W. Hänsel, C. F. Roos, J. Benhelm, D. Chek al kar, M. Chwalla, T. Körber, U. D. Rapol, M. Riebe, P. O. Schmidt, C. Becher, O. Gühne, W. Dür, and R. Blatt. Scalable multiparticle entanglement of trapped ions. *Nature*, 438:643–646, 2005.

[73] C. Cabrillo, J. I. Cirac, P. Garcia-Fernandez, and P. Zoller. Creation of entangled states of distant atoms by interference. *Phys. Rev. A*, 59:1025–1033, 1999.

[74] L.-M. Duan and J. Kimble. Efficient engineering of multiatom entanglement through single-photon detections. *Phys. Rev. Lett.*, 90:253601, 2003.

[75] U. Eichmann, J. C. Bergquist, J. J. Bollinger, J. M. Gilligan, W. M. Itano, D. J. Wineland, and M. G. Raizen. Young's interference experiment with light scattered from two atoms. *Phys. Rev. Lett.*, 70:2359–2362, 1993.

[76] W. M. Itano, J. C. Bergquist, J. J. Bollinger, D. J. Wineland, U. Eichmann, and M. G. Raizen. Complementarity and Young's interference fringes from two atoms. *Phys. Rev. A*, 57:4176–4187, 1998.

[77] Yuan Liang Lim, Almut Beige, and Leong Chuan Kwek. Repeat-until-success linear optics distributed quantum computing. *Phys. Rev. Lett.*, 95(3):030505, 2005.

[78] Yuan Liang Lim, Sean D. Barrett, Almut Beige, Pieter Kok, and Leong Chuan Kwek. Repeat-until-success quantum computing using stationary and flying qubits. *Phys. Rev. A*, 73(1):012304, 2006.

[79] A. Imamoḡlu. Quantum computation using quantum dot spins and microcavities. *Fortschr. Phys.*, 48:987–997, 2000.

[80] C. Piermarocchi, Pochung Chen, L. J. Sham, and D. G. Steel. Optical RKKY interaction between charged semiconductor quantum dots. *Phys. Rev. Lett.*, 89(16):167402, Sep 2002.

[81] Filippo Troiani, Elisa Molinari, and Ulrich Hohenester. High-finesse optical quantum gates for electron spins in artificial molecules. *Phys. Rev. Lett.*, 90(20):206802, May 2003.

[82] E. Pazy, E. Biolatti, T. Calarco, I. D'Amico, P. Zanardi, F. Rossi, and P. Zoller. Spin-based optical quantum computation via Pauli blocking in semiconductor quantum dots. *Europhys. Lett.*, 62:175–181, 2003.

[83] T. Calarco, A. Datta, P. Fedichev, E. Pazy, and P. Zoller. Spin-based all-optical quantum computation with quantum dots: Understanding and suppressing decoherence. *Phys. Rev. A*, 68(1):012310, Jul 2003.

[84] L. Childress, J. M. Taylor, A. S. Sorensen, and M. D. Lukin. Fault-tolerant quantum communication based on solid-state photon emitters. *Phys. Rev. Lett.*, 96(7):070504, 2006.

[85] M. V. Gurudev Dutt, L. Childress, L. Jiang, E. Togan, J. Maze, F. Jelezko, A. S. Zibrov, P. R. Hemmer, and M. D. Lukin. Quantum Register Based on Individual Electronic and Nuclear Spin Qubits in Diamond. *Science*, 316(5829):1312–1316, 2007.

[86] C. K. Hong, Z. Y. Ou, and L. Mandel. Measurement of subpicosecond time intervals between two photons by interference. *Phys. Rev. Lett.*, 59:2044–2046, 1987.

[87] B. Yurke, S. L. McCall, and J. R. Klauder. SU(2) and SU(1,1) interferometers. *Phys. Rev. A*, 33:4033–4054, 1986.

[88] A. R. Edmunds. *Angular Momentum in Quantum Mechanics*. Princeton, 1960.

[89] L.-M. Duan, B. B. Blinov, D. L. Moehring, and C. Monroe. Scaling trapped ions for quantum computation with probabilistic ion-photon mapping. *Quant. Inf. Comp.*, 4:165–173, 2004.

[90] R. Blatt, H. Häffner, C. F. Roos, C. Becher, and F. Schmidt-Kaler. Ion trap quantum computing with Ca^+ ions. *Quantum Inf. Proc.*, 3:61–73, 2004.

[91] P. T. H. Fisk. Trapped-ion and trapped-atom microwave frequency standards. *Reports on Progress in Physics*, 60:761–817, 1997.

[92] P. Gill, editor. *Proceedings of the 6th Symposium on Frequency Standards and Metrology,*. World Scientific, Singapore, 2002.

[93] L. Deslauriers, M. Acton, B. B. Blinov, K.-A. Brickman, P. C. Haljan, W. K. Hensinger, D. Hucul, S. Katnik, Jr. R. N. Kohn, P. J. Lee, M. J. Madsen, P. Maunz, S. Olmschenk, D. L. Moehring, D. Stick, J. Sterk, M. Yeo, K. C. Younge, and C. Monroe. Efficient photoionization loading of trapped ions with ultrafast pulses. *Phys. Rev. A*, 74(6):063421, 2006.

[94] B. B. Blinov, Jr. R. N. Kohn, M. J. Madsen, P. Maunz, D. L. Moehring, and C. Monroe. Broadband laser cooling of trapped atoms with ultrafast laser pulses. *J. Opt. Soc. Am. B*, 23:1170–1173, 2006.

[95] D. L. Moehring, B. B. Blinov, D. W. Gidley, Jr. R. N. Kohn, M. J. Madsen, T. B. Sanderson, R. S. Vallery, and C. Monroe. Precision lifetime measurement of a single trapped ion with ultrafast laser pulses. *Phys. Rev. A*, 73:023413, 2006.

[96] L. Deslauriers, P. C. Haljan, P. J. Lee, K-A. Brickman, B. B. Blinov, M. J. Madsen, and C. Monroe. Zero-point cooling and low heating of trapped $^{111}Cd^+$ ions. *Phys. Rev. A*, 70(4):043408, 2004.

[97] A. S. Bell, P. Gill, H. A. Klein, A. P. Levick, Chr. Tamm, and D. Schnier. Laser cooling of trapped ytterbium ions using a four-level optical-excitation scheme. *Phys. Rev. A*, 44(1):R20–R23, Jul 1991.

[98] Ann-Marie Mårtensson-Pendrill, David S. Gough, and Peter Hannaford. Isotope shifts and hyperfine structure in the 369.4-nm 6s-$6p_{1/2}$ resonance line of singly ionized ytterbium. *Phys. Rev. A*, 49(5):3351–3365, May 1994.

[99] P. Taylor, M. Roberts, S. V. Gateva-Kostova, R. B. M. Clarke, G. P. Barwood, W. R. C. Rowley, and P. Gill. Investigation of the $^2S_{1/2} - {}^2D_{5/2}$ clock transition in a single ytterbium ion. *Phys. Rev. A*, 56(4):2699–2704, Oct 1997.

[100] M. Roberts, P. Taylor, G. P. Barwood, P. Gill, H. A. Klein, and W. R. C. Rowley. Observation of an electric octupole transition in a single ion. *Phys. Rev. Lett.*, 78(10):1876–1879, Mar 1997.

[101] M. Roberts, P. Taylor, S. V. Gateva-Kostova, R. B. M. Clarke, W. R. C. Rowley, and P. . Measurement of the $^2S_{1/2} - {}^2D_{5/2}$ clock transition in a single $^{171}Yb^+$ ion. *Phys. Rev. A*, 60(4):2867–2872, Oct 1999.

[102] P. J. Blythe, S. A. Webster, H. S. Margolis, S. N. Lea, G. Huang, S.-K. Choi, W. R. C. Rowley, P. Gill, and R. S. Windeler. Subkilohertz absolute-frequency measurement of the 467-nm electric octupole transition in $^{171}Yb^+$. *Phys. Rev. A*, 67(2):020501, Feb 2003.

[103] P. Gill, G. P. Barwood, H. A. Klein, G. Huang, S. A. Webster, P. J.Blythe, K. Hosaka, S. N. Lea, and H. S. Margolis. Trapped ion optical frequency standards. *Meas. Sci. Technol.*, 14:1174–1186, 2003.

[104] N. Yu and L. Maleki. Lifetime measurements of the $4f^{14}5d$ metastable states in single ytterbium ions. *Phys. Rev. A*, 61(2):022507, Jan 2000.

[105] Chr. Balzer, A. Braun, T. Hannemann, Chr. Paape, M. Ettler, W. Neuhauser, and Chr. Wunderlich. Electrodynamically trapped Yb^+ ions for quantum information processing. *Phys. Rev. A*, 73(4):041407, 2006.

[106] D. Kielpinski, M. Cetina, J. A. Cox, and F. X. Kärtner. Laser cooling of trapped ytterbium ions with an ultraviolet diode laser. *Opt. Lett.*, 31:757–759, 2006.

[107] D. Engelke and Chr. Tamm. Dark times in the resonance fluorescence of trapped ^{171}Yb ions caused by spontaneous quantum jumps to the $^2D_{3/2}$ (F=2) state. *Europhysics Letters (EPL)*, 33(5):347–352, 1996.

[108] Chr. Tamm, D. Engelke, and V. Bühner. Spectroscopy of the electric-quadrupole transition $^2S_{1/2}(F=0) - {}^2D_{3/2}(F=2)$ in trapped $^{171}Yb^+$. *Phys. Rev. A*, 61(5):053405, Apr 2000.

[109] R. W. P. Drever, J. L. Hall, F. V. Kowalski, J. Hough, G. M. Ford, A. J. Munley, and H. Ward. Laser phase and frequency stabilization using an optical resonator. *Appl. Phys. B: Lasers and Optics*, 31:97–105, 1983.

[110] Eric D. Black. An introduction to Pound–Drever–Hall laser frequency stabilization. *American Journal of Physics*, 69(1):79–87, 2001.

[111] S. Gerstenkorn and P. Luc. *Atlas du spectre d'absorption de la molecule d'iode, 14800-20000 cm^{-1}*. Editions du Centre National de la Recherche Scientifique (CNRS), Paris, France, 1978.

[112] S. Gerstenkorn, J. Verges, and J. Chevillard. *Atlas du spectre d'absorption de la molecule d'iode, 11000-14000 cm^{-1}*. Laboratoire Aime - Cotton CNRS II, Orsay, France, 1982.

[113] M. Acton, K.-A. Brickman, P. C. Haljan, P. J. Lee, L. Deslauriers, and C. Monroe. Near-perfect simultaneous measurement of a qubit register. *Quant. Inf. Comp.*, 6:465–482, 2006.

[114] Martin J. Madsen. *Advanced Ion Trap Development and Ultrafast Laser-Ion Interactions*. PhD thesis, Department of Physics, University of Michigan, 2006.

[115] S. R. Jefferts, C. Monroe, E. W. Bell, and D. J. Wineland. Coaxial-resonator-driven rf (Paul) trap for strong confinement. *Phys. Rev. A*, 51:3112, 1995.

[116] B. B. Blinov, D. L. Moehring, L.-M. Duan, and C. Monroe. Observation of entanglement between a single trapped atom and a single photon. *Nature*, 428:153–157, 2004.

[117] S. Haroche, J. M. Raimond, and M. Brune. *Experimental Quantum Computation and Information*, pages 3–36. IOS Press, Amsterdam, 2002.

[118] A. Kuhn and G. Rempe. *Experimental Quantum Computation and Information*, pages 37–66. IOS Press, Amsterdam, 2002.

[119] J. McKeever, J. R. Buck, A. D. Boozer, A. Kuzmich, H.-C. Nägerl, D. M. Stamper-Kurn, and H. J. Kimble. State-insensitive cooling and trapping of single atoms in an optical cavity. *Phys. Rev. Lett.*, 90:133602, 2003.

[120] R. G. DeVoe and R. G. Brewer. Observation of superradiant and subradiant spontaneous emission of two trapped ions. *Phys. Rev. Lett.*, 76:2049–2052, 1996.

[121] A. Kuzmich, L. Mandel, and N. P. Bigelow. Generation of spin squeezing via continuous quantum nondemolition measurement. *Phys. Rev. Lett.*, 85:1594–1597, 2000.

[122] B. Julsgaard, A. Kozhekin, and E. S. Polzik. Experimental long-lived entanglement of two macroscopic objects. *Nature*, 413:400–403, 2001.

[123] A. Kuzmich, W. P. Bowen, A. D. Boozer, A. Boca, C. W. Chou, L.-M. Duan, and H. J. Kimble. Generation of nonclassical photon pairs for scalable quantum communication with atomic ensembles. *Nature*, 423:731–734, 2003.

[124] C. H. van der Wal, M. D. Eisaman, A. Andr, R. L. Walsworth, D. F. Phillips, A. S. Zibrov, and M. D. Lukin. Atomic memory for correlated photon states. *Science*, 301:196–200, 2003.

[125] D. N. Matsukevich and A. Kuzmich. Quantum state transfer between matter and light. *Science*, 306:663–666, 2004.

[126] C. W. Chou, H. de Riedmatten, D. Felinto, S. V. Polyakov, S. J. van Enk, and H. J. Kimble. Measurement-induced entanglement for excitation stored in remote atomic ensembles. *Nature*, 438:828–832, 2005.

[127] D. Bouwmeester, A. Ekert, and A. Zeilinger, editors. *Quantum Cryptography, Quantum Teleportation, Quantum Computation*. Springer, 2000.

[128] D. J. Wineland, C. Monroe, W. M. Itano, D. Leibfried, B. E. King, and D. M. Meekhof. Experimental issues in coherent quantum-state manipulation of trapped atomic ions. *Journal of Research of the National Institute of Standards and Technology*, 103:259–328, 1998.

[129] L.-M. Duan, M. D. Lukin, J. I. Cirac, and P. Zoller. Long-distance quantum communication with atomic ensembles and linear optics. *Nature*, 414:413–418, 2001.

[130] R. Blatt and P. Zoller. Quantum jumps in atomic systems. *Eur. J. Phys.*, 9:250–256, 1988.

[131] Philip M. Pearle. Hidden-variable example based upon data rejection. *Phys. Rev. D*, 2(8):1418–1425, Oct 1970.

[132] P. G. Kwiat, P. H. Eberhard, A. M. Steinberg, and R. Y. Chiao. Proposal for a loophole-free Bell inequality experiment. *Phys. Rev. A*, 49:3209–3220, 1994.

[133] S. F. Huelga, M. Ferrero, and E. Santos. Loophole-free test of the Bell inequalities. *Phys. Rev. A*, 51:5008–5011, 1995.

[134] E. S. Fry, T. Walther, and S. Li. Proposal for a loophole-free test of the Bell inequalities. *Phys. Rev. A*, 52:4381–4395, 1995.

[135] P. Maunz, D. L. Moehring, M. J. Madsen, Jr. R. N. Kohn, K. C. Younge, and C. Monroe. Quantum interference of photon pairs from two trapped atomic ions. *arXiv:quant-ph/0608047v1*, 2006.

[136] B. Darquié, M. P. A. Jones, J. Dingjan, J. Beugnon, S. Bergamini, Y. Sortais, G. Messin, A. Browaeys, and P. Grangier. Controlled Single-Photon Emission from a Single Trapped Two-Level Atom. *Science*, 309(5733):454–456, 2005.

[137] P. J. Lee, K.-A. Brickman, L. Deslauriers, P. C. Haljan, L.-M. Duan, and C. Monroe. Phase control of trapped ion quantum gates. *Journal of Optics B*, 7:S371–S383, 2005.

[138] J. Beugnon, M. P. A. Jones, J. Dingjan, B. Darquié, G. Messin, A. Browaeys, and P. Grangier. Quantum interference between two single photons emitted by independently trapped atoms. *Nature*, 440:779–782, 2006.

[139] F. Diedrich and H. Walther. Nonclassical radiation of a single stored ion. *Phys. Rev. Lett.*, 58:203–206, 1987.

[140] W. M. Itano, J. C. Bergquist, and D. J. Wineland. Photon antibunching and sub-Poissonian statistics from quantum jumps in one and two atoms. *Phys. Rev. A*, 38:559–562, 1988.

[141] L. Mandel. Quantum effects in one-photon and two-photon interference. *Rev. Mod. Phys.*, 71:S274–S282, 1999.

[142] Patricia Lee. *Quantum Information Processing with Two Trapped Cadmium Ions*. PhD thesis, Department of Physics, University of Michigan, 2005.

[143] Rainer Kaltenbaek, Bibiane Blauensteiner, Marek Zukowski, Markus Aspelmeyer, and Anton Zeilinger. Experimental interference of independent photons. *Phys. Rev. Lett.*, 96(24):240502, 2006.

[144] C. Santori, D. Fattal, J. Vučković, G.S. Solomon, and Y. Yamamoto. Indistinguishable photons from a single-photon device. *Nature*, 419:594–597, 2002.

[145] Thomas Legero, Tatjana Wilk, Markus Hennrich, Gerhard Rempe, and Axel Kuhn. Quantum beat of two single photons. *Phys. Rev. Lett.*, 93:070503, 2004.

[146] T. Legero, T. Wilk, A. Kuhn, and G. Rempe. Characterization of single photons using two-photon interference. *Adv. At. Mol. Opt. Phys.*, 53:253–289, 2006.

[147] J.K. Thompson, J. Simon, H. Loh, and V. Vuletic. A high-brightness source of narrowband, identical-photon pairs. *Science*, 313:74–77, 2006.

[148] D. Felinto, C.W. Chou, J. Laurat, E.W. Schomburg, H. de Riedmatten, and H.J. Kimble. Conditional control of the quantum states of remote atomic memories for quantum networking. *Nature Physics*, 2:844–848, 2006.

[149] T. Chaneliere, D. N. Matsukevich, S. D. Jenkins, S.-Y. Lan, R. Zhao, T. A. B. Kennedy, and A. Kuzmich. Quantum interference of electromagnetic fields from remote quantum memories. *Physical Review Letters*, 98(11):113602, 2007.

[150] E. H. Pinnington, G. Rieger, and J. A. Kernahan. Beam-laser measurements of the lifetimes of the 6p levels in Yb II. *Phys. Rev. A*, 56:2421–2423, 1997.

[151] P. Maunz, D. L. Moehring, S. Olmschenk, K. C. Younge, D. N. Matsukevich, and C. Monroe. Quantum interference of photon pairs from two remote trapped atomic ions. *Nature Physics*, doi:10.1038/nphys644, 2007.

[152] H.G. Dehmelt. Radiofrequency spectroscopy of stored ions I: Storage. *Adv. At. Mol. Phys.*, 3:53, 1967.

[153] J. Kim, C. J. Nuzman, B. Kumar, D. F. Lieuwen, J. S. Kraus, A. Weiss, C. P. Lichtenwalner, A. R. Papazian, R. E. Frahm, N. R. Basavanhally, D. A. Ramsey, V. A. Aksyuk, F. Pardo, M. E. Simon, V. Lifton, H. B. Chan, M. Haueis, A. Gasparyan, H. R. Shea, S. Arney, C. A. Bolle, P. R. Kolodner, R. Ryf, D. T. Neilson, and J. V Gates. 1100×1100 port MEMS-based optical crossconnect with 4-dB maximum loss. *IEEE Phot. Tech. Lett.*, 15:1537–1539, 2003.

[154] J. Sherson, B. Julsgaard, and E. S. Polzik. Deterministic atom-light quantum interface. *Adv. At. Mol. Opt. Phys.*, 54, 2006.

[155] S. D. Jenkins, D. N. Matsukevich, T. Chanelire, S.-Y. Lan, T. A. B. Kennedy, and A. Kuzmich. Quantum telecommunication with atomic ensembles. *J. Opt. Soc. Am. B*, 24:316–323, 2007.

[156] B.B. Blinov, L. Deslauriers, P. Lee, M.J. Madsen, R. Miller, and C. Monroe. Sympathetic cooling of trapped Cd^+ isotopes. *Phys. Rev. A*, 65:040304(R), 2002.

[157] M. Barrett, B. L. DeMarco, T. Schaetz, V. Meyer, D. Leibfried, J. Britton, J. Chiaverini, W. M. Itano, B. M. Jelenkovic, J. D. Jost, C. Langer, T. Rosenband, and D. J. Wineland. Sympathetic cooling of $^9Be^+$ and $^{24}Mg^+$ for quantum logic. *Phys. Rev. A*, 68:042302, 2003.

[158] P. O. Schmidt, T. Rosenband, C. Langer, W. M. Itano, J. C. Bergquist, and D. J. Wineland. Spectroscopy using quantum logic. *Science*, 309:749–752, 2005.

[159] R. Raussendorf and H. J. Briegel. A one-way quantum computer. *Phys. Rev. Lett.*, 86:5188–5191, 2001.

[160] Adan Cabello and Jan-Ake Larsson. Minimum Detection Efficiency for a Loophole-Free Atom-Photon Bell Experiment. *Phys. Rev. Lett.*, 98(22):220402, 2007.

[161] Nicolas Brunner, Nicolas Gisin, Valerio Scarani, and Christoph Simon. Detection Loophole in Asymmetric Bell Experiments. *Phys. Rev. Lett.*, 98(22):220403, 2007.

[162] S. L. Braunstein and A. Mann. Measurement of the Bell operator and quantum teleportation. *Phys. Rev. A*, 51:R1727, 1995.

[163] K. Mattle, H. Weinfurter, P. G. Kwiat, and A. Zeilinger. Dense coding in experimental quantum communication. *Phys. Rev. Lett.*, 76:4656–4659, 1996.

[164] D. F. V. James and P. G. Kwiat. Atomic-vapor-based high efficiency optical detectors with photon number resolution. *Phys. Rev. Lett.*, 89:183601, 2002.

[165] H.-J. Briegel, W. Dür, J. I. Cirac, and P. Zoller. Quantum repeaters: The role of imperfect local operations in quantum communication. *Phys. Rev. Lett.*, 81:5932–5935, 1998.

[166] W. Dür, H.-J. Briegel, J. I. Cirac, and P. Zoller. Quantum repeaters based on entanglement purification. *Phys. Rev. A*, 59:169–181, 1999.

[167] D. L. Moehring, M. J. Madsen, K. C. Younge, Jr. R. N. Kohn, P. Maunz, L.-M. Duan, C. Monroe, and B. B. Blinov. Quantum networking with photons and trapped atoms. *J. Opt. Soc. Am. B*, 24:300–315, 2007.

[168] Charles H. Bennett, David P. DiVincenzo, John A. Smolin, and William K. Wootters. Mixed-state entanglement and quantum error correction. *Phys. Rev. A*, 54(5):3824–3851, Nov 1996.

[169] Scott Hill and William K. Wootters. Entanglement of a pair of quantum bits. *Phys. Rev. Lett.*, 78(26):5022–5025, 1997.

[170] Russell L. Miller. *Work Towards the Observation of Trapped Cd^+ Ion Interactions with Intense Laser Pulses*, B.S. Thesis, Department of Physics, University of Michigan, 2004.